

Seismological and Seismotectonic Analysis of the Northwestern Argentine Central Andean Foreland

Martin Zeckra, M.Sc.

Univ.-Diss.

**zur Erlangung des akademischen Grades
"doctor rerum naturalium"
(Dr. rer. nat.)
in der Wissenschaftsdisziplin "Seismologie"**

**eingereicht an der
Mathematisch-Naturwissenschaftlichen Fakultät
Institut für Geowissenschaften
der Universität Potsdam**

Ort und Tag der Disputation: Potsdam, den 19.05.2020

This work is licensed under a Creative Commons License:
Attribution – Non Commercial – Share Alike 4.0 International.
This does not apply to quoted content from other authors.
To view a copy of this license visit
<https://creativecommons.org/licenses/by-nc-sa/4.0/>

Hauptbetreuer*in: apl. Prof. Dr. Frank Krüger
Betreuer*innen: Prof. Dr. Torsten Dahm
Gutachter*innen: apl. Prof. Ed Sobel, PhD
Prof. Frederik Tilmann, PhD
PD Dr. Sascha Brune
Prof. Dr. Fernando Hongn (schriftl.)

Published online in the
Institutional Repository of the University of Potsdam:
<https://doi.org/10.25932/publishup-47324>
<https://nbn-resolving.org/urn:nbn:de:kobv:517-opus4-473240>

Abstract

After a severe M_W 5.7 earthquake on October 17, 2015 in El Galpón in the province of Salta NW Argentina, I installed a local seismological network around the estimated epicenter. The network covered an area characterized by inherited Cretaceous normal faults and neotectonic faults with unknown recurrence intervals, some of which may have been reactivated normal faults. The 13 three-component seismic stations recorded data continuously for 15 months.

The 2015 earthquake took place in the Santa Bárbara System of the Andean foreland, at about 17km depth. This region is the easternmost morphostructural region of the central Andes. As a part of the broken foreland, it is bounded to the north by the Subandes fold-and-thrust belt and the Sierras Pampeanas to the south; to the east lies the Chaco-Paraná basin.

A multi-stage morphotectonic evolution with thick-skinned basement uplift and coeval thin-skinned deformation in the intermontane basins is suggested for the study area. The release of stresses associated with the foreland deformation can result in strong earthquakes, as the study area is known for recurrent and historical, destructive earthquakes. The available continuous record reaches back in time, when the strongest event in 1692 (magnitude 7 or intensity IX) destroyed the city of Esteco. Destructive earthquakes and surface deformation are thus a hallmark of this part of the Andean foreland.

With state-of-the-art Python packages (e.g. pyrocko, ObsPy), a semi-automatic approach is followed to analyze the collected continuous data of the seismological network. The resulting 1435 hypocenter locations consist of three different groups: 1.) local crustal earthquakes (nearly half of the events belong to this group), 2.) interplate activity, of regional distance in the slab of the Nazca-plate, and 3.) very deep earthquakes at about 600km depth. My major interest focused on the first event class. Those crustal events are partly aftershock events of the El Galpón earthquake and a second earthquake, in the south of the same fault. Further events can be considered as background seismicity of other faults within the study area. Strikingly, the seismogenic zone encompass the whole crust and propagates brittle deformation down, close to the Moho.

From the collected seismological data, a local seismic velocity model is estimated, using VELEST. After the execution of various stability tests, the robust minimum 1D-velocity model implies guiding values for the composition of the local, subsurface structure of the crust. Afterwards, performing a hypocenter relocation enables the assignment of individual earthquakes to aftershock clusters or extended seismotectonic structures. This allows the mapping of previously unknown seismogenic faults.

Finally, focal mechanisms are modeled for events with accurately located hypocenters, using the newly derived local velocity model. A compressive regime is attested by the majority of focal mechanisms, while the strike direction of the individual seismogenic structures is in agreement with the overall north – south orientation of the Central Andes, its mountain front, and individual mountain ranges in the southern Santa-Bárbara-System.

Zusammenfassung

Nach einem schweren Erdbeben der Magnitude M_W 5.7 am 17. Oktober 2015 in El Galpón, in der Provinz Salta im Nordwesten Argentiniens, habe ich ein lokales seismologisches Netzwerk, um das vermutete Epizentrum herum, aufgebaut. Dabei haben 13 Stationen kontinuierlich für 15 Monate gemessen. Das Netzwerk wurde in einem Gebiet installiert, welches durch tektonische Störungen charakterisiert ist, die entweder in der Kreidezeit zunächst als Abschiebungen initiiert und später als Aufschiebungen reaktiviert wurden oder in der geologischen jüngeren Vergangenheit erst entstanden sind. Die Intervallzeiten zwischen zwei Erdbeben sind dabei häufig unbekannt.

Das Erdbeben von 2015 trat im Santa-Barbara-System im Argentinischen Vorland, 17km unter der Erdoberfläche auf. Diese Region ist die östlichste strukturgeologische Provinz der Zentralanden und dem broken-foreland-Typus zuzuordnen. Im Norden schließt sich der Bolivianische Faltengürtel (Sierras Subandinas) und im Süden die Sierras Pampeanas an; im Osten liegt das Chaco-Paraná Becken.

Eine mehrstufige morphotektonische Entwicklung wird hier vermutet, bei der das Grundgebirge durch als thick-skinned bezeichnete Deformation herausgehoben wurde und die dazwischen liegenden Intermontanbecken gleichzeitig Deformation des Typs thin-skinned erfahren haben. Die plötzliche Spannungsfreisetzung, die mit dieser Vorlanddeformation einhergeht, kann zu starken Erdbeben führen. Das Untersuchungsgebiet ist für wiederkehrende und historische, zerstörerische Erdbeben bekannt. Der zur Verfügung stehenden Aufzeichnungen reichen bis in das Jahr 1692 zurück, als ein Erdbeben der Magnitude M7 (oder Intensität IX) die Stadt Esteco zerstörte. Daher sind zerstörerische Erdbeben ein besonderes Kennzeichen in diesem Teil des Andenvorlands.

Für die Analyse der im seismologischen Netzwerk aufgezeichneten kontinuierlichen Daten wurde ein semiautomatischer Ansatz verfolgt, der mittels hochmoderner Python-Bibliotheken informationstechnisch umgesetzt wurde. Die resultierenden 1435 Erdbeben bestehen aus drei verschiedenen Gruppen: 1.) lokale Erdbeben in der Erdkruste (die etwa die Hälfte aller Events ausmachen), 2.) weiter entfernte Interplattenaktivität, die durch die Subduktion der Nazca-Platte unter den Südamerikanischen Kontinent hervorgerufen wird und 3.) sehr tiefen Erdbeben in etwa 600 km Tiefe. Mein Hauptaugenmerk lag dabei auf der ersten Gruppe. Diese krustalen Ereignisse sind teilweise Nachbeben des El Galpón Erdbebens und eines weiteren Bebens, welches sich weiter im Süden an der gleichen Störung ereignete. Die restlichen Beben können der allgemeinen Hintergrundaktivität entlang weiterer Störungen im Untersuchungsgebiet zugeschrieben werden. Beachtenswert ist dabei der Umstand, dass die Erdbebenaktivität in der gesamten Kruste beobachtet werden kann und sich dadurch die Deformation bis a fast an den Erdmantel ausbreitet.

Mit den gesammelten Daten kann, unter der Verwendung der VELEST Software, ein lokales seismisches Geschwindigkeitsmodell bestimmt werden. Nach der Durchführung verschiedener Stabilitätstests, können aus dem robusten eindimensionalen Modell Richtwerte für die Zusammensetzung und den Aufbau der Erdkruste gewonnen werden. Die

anschließende Relokalisierung von Erdbebenherden erlaubt die Zuordnung einzelner Erdbeben zu Erdbebenclustern oder ausgedehnten seismotektonischen Strukturen. Dadurch können sogar zuvor unbekannte seismogene Störungen kartiert werden.

Schlussendlich, werden Herdflächenlösungen für Beben mit präzise lokalisierten Erdbebenherden und unter der Einbeziehung des neu bestimmten lokalen Geschwindigkeitsmodells modelliert. Der Großteil der resultierenden Lösungen bestätigt das vorherrschende kompressive Regime. Das Streichen der einzelnen seismogenen Strukturen stimmt größtenteils mit der allgemeinen Nord – Süd Ausrichtung der Zentralanden, ihrer Gebirgsfront und den einzelnen Höhenzügen im Santa-Barbará-System überein.

Contents

1	Introduction	1
1.1	Geological Settings	2
1.2	Historical Seismicity	6
1.3	The 2015 El Galpón Event	9
1.3.1	Macroseismic Event Description	9
1.3.2	Teleseismic Source Information	11
1.3.3	Hypocentral Depth Reestimation	12
2	Topic I: Seismological Field Instrumentation	15
2.1	Damage Identification	15
2.2	STRATEGY - Temporal Seismic Network	16
2.2.1	Network installation	16
2.2.2	Data Quality	19
2.2.3	Data Loss	21
2.2.4	Data Publishing	24
2.3	Instrument Validation - Huddle Test	24
2.3.1	Method	24
2.3.2	Results	26
3	Topic II: Event Identification	28
3.1	Event Detection - LASSIE	30
3.2	Phase Picking	32
3.3	Results	34
3.3.1	Pick Uncertainty	36
3.3.2	Wadati-Diagram	37
3.3.3	Network Based Time Correction for Single Station Static Clock Offset	38
4	Topic III: Event Catalog	42
4.1	Event Location	42
4.2	Magnitude Estimation	43
4.3	Results	44
4.3.1	Seismicity	46
4.3.2	Spatial Hypocenter Distribution	46
4.3.3	Magnitude Analysis	50

5	Topic IV: Minimum 1D – Velocity Model	53
5.1	Mantle Velocity Estimation	53
5.2	Data Selection	56
5.3	Approaching Stable Solutions	57
5.3.1	Model Layering	57
5.3.2	Initial Hypocenters	60
5.3.3	Jackknife Resampling	62
5.3.4	Geographical Subsets	63
5.4	Final Velocity Model	65
6	Topic V: Event Relocation	70
6.1	Method	70
6.2	Data Preparation	71
6.3	Relocation Catalog	73
7	Topic VI: Focal Mechanisms Inversion	75
7.1	Method	76
7.2	Data Selection and Preparation	77
7.3	Results	78
7.3.1	El Galpón Aftershock Cluster	79
7.3.2	Rosario Aftershock Cluster	80
7.3.3	Sierra de la Candelaria	80
7.3.4	Cerro Colorado	80
7.3.5	Decollement	81
8	Topic VII: Seismotectonic Interpretation of the Study Area	82
8.1	Petrological and Geophysical Parameters	82
8.2	Seismotectonic Interpretation	83
8.3	Seismic Hazard Estimation	85
9	Conclusions	86
	Acknowledgments	87
	List of Figures	89
	Bibliography	91
A	Appendix	106
A.1	Wadati-Diagram	106
A.1.1	Derivation for source time independent v_P/v_S ratio estimation . . .	106
A.1.2	Derivation for time offset calculation from Wadati-Diagram . . .	107
A.2	Shake reports during recording period of STRATEGy network	107
A.3	Moment Tensor solutions for 2015 El Galpón EQ	108
A.4	Focal Mechanisms of Supervised Events	109

A.5	Velocity Models	112
A.6	Uncertainty plots	118

1 Introduction

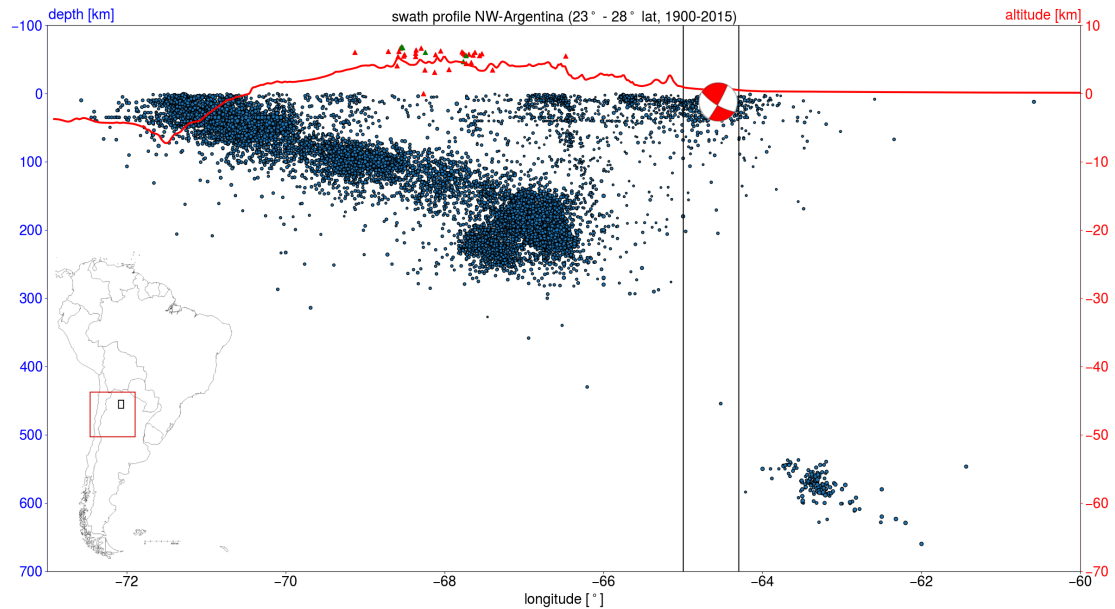


Figure 1.1: All earthquakes from the ISC-bulletin [1] from 1900 until 2015 between -23° and -28° lat are plotted as blue dots by depth on a profile from -73° to -60° lon. This corresponds to the dimension of the red rectangle in the overview map. The topography at -25° lat is plotted on top as a red line, exaggerated by a factor of ten compared to the hypocentral depths. Volcanoes in the same region plotted as triangles (red: inactive, green: active). Focal mechanism of an $M_W 5.7$ earthquake (see Section 1.3. Black vertical lines indicate the east – west extension of a temporarily installed seismic network (see Section 2.2).

The Andean orogeny offers an unique natural observatory for all kind of geoscientific processes, offering manifold possibilities to tackle various research questions. From a seismologists point of view, the Andes display a first-order homogeneous, trench-perpendicular stress field over its 7,000 km extent, forced by a subduction process. The seismic activity at the plate interface is responsible for the majority of the strain release and produced megathrust earthquakes with the largest, instrumentally recorded magnitudes ($M_W 9.5$) [2] [3]. Strike-perpendicularly tracing the seismicity reveals along-strike variation of subduction angles [4] and internal orogenic deformation [5] [6].

Focusing on the Central Andes, seismic activity in the normal-dipping slab interface is continuously traceable downdip up to 250 km (see Figure 1.1) [7] beneath the Altiplano-Puna plateau, the second largest high plateau on the Earth. The aseismic extension of the Benioff-zone deeper into the mantle, is supported by various tomographic studies [8] [9] [10] [11], and attaches a structural link to the deep-foci earthquake clusters [12].

Crustal seismicity of the back-arc region of the Central Andes is localized in the foreland, a region of limited topography but evident Quaternary deformation, i.e., a M_W 5.7 earthquake in NW Argentina in 2015 (see Section 1.3 and focal mechanism in Figure 1.1). High precipitation gradients caused by steep orographic barriers [13], induce dense vegetation, preventing accessibility for field-based geological studies. Hence, geophysical studies using active [14] and passive sources [15] [16] offer reasonable alternative methods for in-depth analyses of the Central Andean Foreland System.

In this thesis I aim to fill the gap of fundamental knowledge of recent seismological deformation. Besides the work of Cahill [15] and Whitman [17] located in the Eastern Cordillera as the most proximal, comparable investigation, no other seismological study focused on the eastern Andean thrust front of the Central Andes [18]. Hence, the temporal installation of a seismological network, alongside with field observations, is described first. The implementation of a semi-automatic data processing workflow (Chapter 3 and Chapter 4) leads to an earthquake catalog with 1435 primary hypocenters (Chapter 4). Afterwards, well-constraint events are chosen to estimate a local 1D-velocity model (Chapter 5) and to perform a highly accurate hypocenter relocation (6). Based on focal mechanisms estimated for distinct events in the study area (Chapter 7), an in-depth image of the ongoing, recent seismotectonic deformation is drawn and discussed, with respect to previous ideas about the foreland deformation of the Central Andes and necessary future investigations (Chapter 8).

1.1 Geological Settings

The geological settings of the studied area is mainly taken from (with minor adaptions) from the paper "Neotectonic activity in the low-strain broken foreland (Santa Bárbara System) of the north-western Argentinean Andes, (26° S)" [14], which is in the review process at Lithosphere and for which I am co-author.

The seismically active broken foreland of the north-western Argentinean Andes between 23°S and 33°S constitutes an environment with discontinuous and reactivated pre-existing structures; often active on time scales of 10^3 to 10^4 years and with long recurrence intervals [5] [20] [19]. In such environments, the accumulation of shortening during repeated earthquakes is suggested by variably deformed Quaternary deposits, tectonic landforms, and reverse fault-bounded mountain ranges [21] [22] [23]. In some cases, these mountain ranges are not bounded by faults, however, whose motion would explain their relief, but rather constitute extensive basement-cored antiforms associated with sedimentary drape folds that are underlain by blind faults (e.g., [22], [23], [24]). In combination, these different structural and tectono-geomorphic phenomena reflect the complex long-term effects of protracted Cenozoic shortening superimposed on

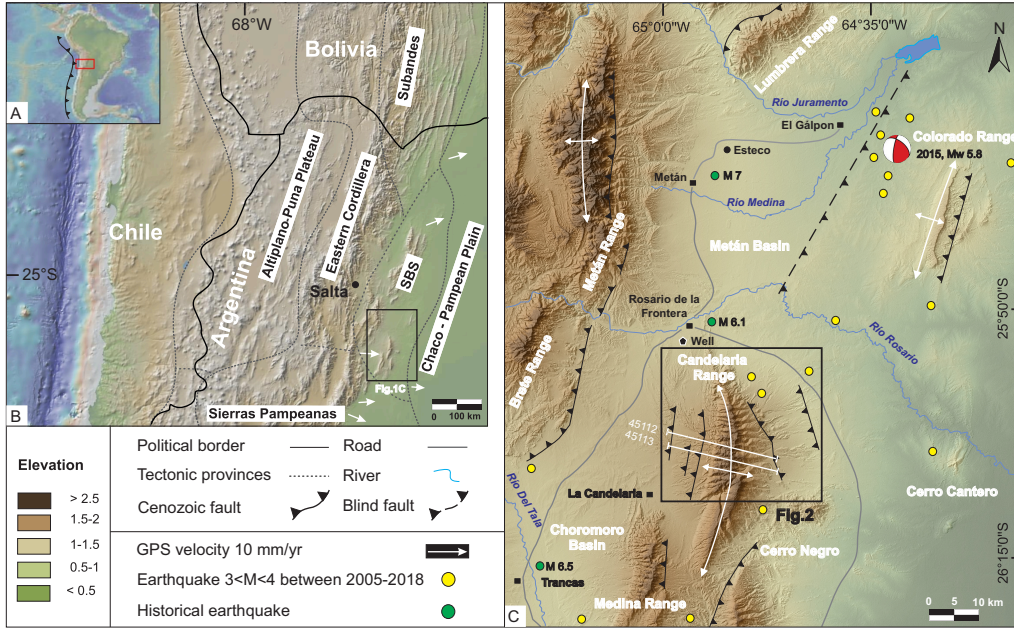


Figure 1.2: Regional morphotectonic setting of the northern broken foreland of the Argentinean Andes with adjacent geological provinces. Inset (A) shows location of study area in the Andean context, red box outlines area covered by Figure B. (B) DEM of the north-western Argentinean Andes with principal morphotectonic provinces [5] and GPS-velocity vectors [19]. Black rectangle outlines area covered by Figure C. (C) DEM with 12.5 m spatial resolution of the Santa Barbara System (SBS) of the broken foreland and its transition with the Eastern Cordillera (west) and the Subandean fold-and-thrust belt (north). Locations of destructive historical earthquakes (see Section 1.2) and focal mechanism of the 2015 Mw 5.8 El Galpón earthquake are also shown.

crustal anisotropies in the broken Andean foreland. As such, this region is akin to the Cretaceous-Eocene basement uplifts of the North American Laramide province [25] [5] [26] and the seismically active Tian Shan of Central Asia [27] [28].

The broken foreland of the Argentinean Andes comprises the reverse-fault bounded Sierras Pampeanas basement blocks [29] and the basement-cored uplifts of the Santa Bárbara System (SBS) in the northern part of the foreland [30] (Figure 1.2). The Santa Bárbara System has been interpreted to record the contractional inversion of a Cretaceous extensional province, the former Salta Rift [31] [32] [30] [33]. At about 23°S, this morphotectonic province transitions into the thin-skinned Sub-Andean foreland fold-and-thrust belt of north-western Argentina and Bolivia (Figure 1.2).

Regarding the morpho-structural and stratigraphic appearance, the SBS is separated into a northern and a southern section, separated by the Metán depression. This inter-

nal boundary falls together with the regional El Toro lineament [23]. In the northern sector, the oldest exposed strata is Ordovician, exhumed through consistently west-vergent thrust faults [34]. To the south, ongoing, spatially and temporally disparate tectonic activity within the SBS has created a compressional basin-and-range topography with asymmetrically uplifted mountain ranges, intervening sedimentary basins, and tectonically forced drainage patterns and landforms, with evidence for different stages of tectonic inversion [35] [36] [37] [22] [38] [23] [39].

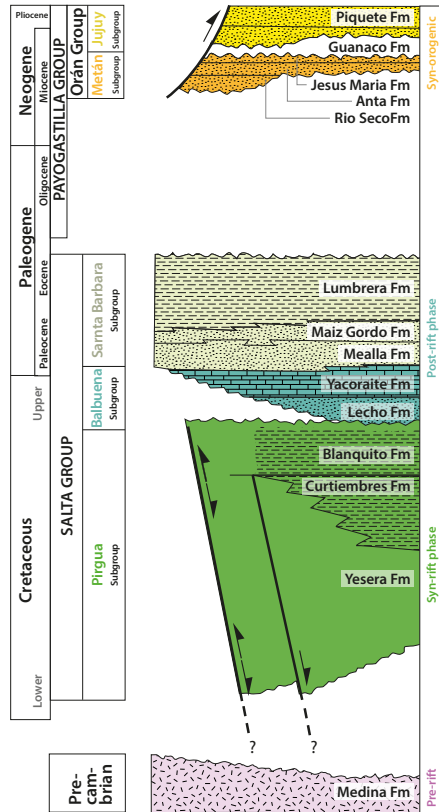


Figure 1.3: Stratigraphic column of the units exposed in the greater La Candelaria Range region, modified after [40] and [41].

The CR of the SBS belongs to a series of spatially separated, reverse fault-bounded or fault-cored basement ranges in the formerly contiguous foreland (Figure 1.2) [42] [39]. The uplift history of the SBS ranges is directly linked with the spatially and temporally disparate eastward migration of Andean deformation in this sector of the foreland [43]

[6] [44] [45] [46]. This is in stark contrast with the tectonically active deformation front of the Sub-Andean fold-and-thrust belt toward the north (e.g., [47]).

The N–S-trending, basement-cored asymmetric antiform of the CR is located between 25.5°S and 26.5°S and 65.5°W and 64.5°W (Figure 1.2, Figure 1.3). The range interior exposes pervasively deformed Upper Precambrian to Lower Cambrian metasediments [48] [49], whereas folded sedimentary cover rocks are preserved around the flanks of the range and dip outward [50] [51] [24]. These units are terrigenous and marine Cretaceous strata of the Salta Group, followed by Tertiary units of the Mio-Pliocene Orán Group [43] (Figure 1.3).

The oldest units of the Salta Group comprise fault-bounded red conglomerates and sandstones interbedded with thin layers of limestones [43] [40] of the Pirgua subgroup; these syn-rift deposits are followed by post-rift sandstones and calcareous strata [52] [53], as well as lacustrine mudstones [54] of the Balbuena and Santa Barbara subgroups, respectively. These rift related units are unconformably overlain by the strata of the syn-orogenic Metán and Jujuy subgroups (Orán Group). The majority of these Tertiary units are sandstones, conglomerates, and fluvio-lacustrine deposits [55] [56].

In turn, these units are unconformably overlain by Plio-Pleistocene alluvial-fan conglomerates [56]. All piedmont sectors of the CR are covered by these coarse deposits, which form an integral part of gently inclined geomorphic surfaces that occur at successively lower elevations. Except for the lowest, active alluvial fan, all of these surfaces are isolated remnants of formerly contiguous, coalesced alluvial fans that have been incised since they were abandoned as active depositional environments.

East of the CR, the *Cerro Negro* preserves spherical deformation of Cretaceous and Cenozoic sedimentary units. The dome-shaped anticline is caused by the intrusion of the Pliocene Antilla magmatic complex [57]. The mafic dikes were emplaced (age: 4.7 Ma) contemporaneously to the development of relief in the CR and adjacent basement-cored ranges [58]. Inferred from geochemical analyses, the evolution of the Antilla complex implies lithospheric foundering in the region with consequent asthenospheric upflow.

Instead of a sharp boundary between the northern and the southern section of the SBS, the *Cerro Colorado* mountain range presents a transitional characteristic, comprising features of both sectors. The cuesta exposes the complete stratigraphic column from syn-rift to post-rift phase sediments. Nevertheless, no basement rock is exposed [45]. The uplift of the topographic relief was generated through a west-dipping inverted normal fault [38] adjacent to a partly buried anticline [59]. To the south, the existence of three right-lateral strike-slip faults are proposed, parallel to major lineaments originating from Cretaceous normal faults, and limiting the extension of the Salta rift depocenters [60] [45].

The Metán basin is one of the most prominent Salta rift depocenters [30]. Syn-rift deposits accumulated more than 3 km of sediments, together with up to 2.5 km of post-rift units [42]. Maximum aggregation in depth is observed in the hanging-wall of Cretaceous normal faults. With respect to the seismogenic hazard potential, these structures bear a major risk as inverted reactivated faults. The most intriguing example, the Metán Basin Central Thrust Fault, cuts the whole Metán basin west of the *Cerro Colorado*, with a disputed dip-direction (see Section 4.3.2 and [38]).

1.2 Historical Seismicity

The structural settings presented in the previous Section 1.1 suggest active seismotectonic processes. This statement is promoted by a long history of reported damaging earthquakes in the study area. The first written sources attest seismic activity in the 17th century (e.g. 1632, 1636, 1692), including the *Esteco* earthquake on September 13 1692.

This event was the very first reported fatal earthquake in Argentina. The name is derived from the town of Esteco (complete original name: *Nuestra Señora de Talavera del Esteco*), which was "pulverized" during the shaking, as reported by the governor [61]. From historical sources the intensity is estimated up to IX [62]. Thus, a M7.3 is implied based on the observed and reported shaking, causing damage to distant cities as Salta 85 km away from Esteco. Back in time, the city was a major trade hub for silver from the Higher Andes to the Atlantic harbors at the estuary of the Rio de la Plata. The earthquake invoke the instant downfall of that city and influenced the future development of the region as a whole. Afterwards, the settlement was abandoned completely and the archaeological remnants are still under investigation.

The epicenter location of earthquakes earlier than the 20th century can only be estimated from damage reports and witness protocols. Location uncertainties are therefore very high and, retracing geolocations from those reports is error-prone. In addition, settlement distribution and population density vary through time. As discussed in Section 8.3, seismotectonic structures responsible for a M7.3 have a great spatial extent and could even cross the whole Metán basin [63] [64]. Therefore, there is a need to discuss physical parameters, which cannot be determined from the existing data. The ruins of the city of Esteco, for example, provide evidence of the closest distance to the earthquakes epicenter.

An examination of pre-instrumental earthquake recordings was carried out in the doctoral thesis of Zossi in 1979 [61]. She collected different historical sources of macroseismic reports, primarily from newspaper articles. Together with a list of instrumental earthquakes from different Argentinean seismological observatories, this work presents the most complete earthquake catalog of the study area before the implementation of digital broadband sensors. Although the catalog focus lies on events in the province of Tucumán, it includes events from neighboring municipalities, which were strong enough to be felt or be damaging to parts of the province. Therefore, the list of events is not limited to the southern half of the study area however, it miss some weaker events located in the northern part. The estimated epicenters are shown in Figure 1.4. In this work, locations derived from macroseismicity are taken from the list presented by Zossi or reestimated by the provided source citations. The same observations, reported in [61], are then used to estimate location errors for all events. The location of the strongest damage is mapped here in detail. A direction of the strongest shaking or the direction of the source is rarely suggested. The corresponding location errors are estimated from the distance to the closest settlement with reported shaking. Further, Zossi provides a list of instrumentally recorded earthquakes within and near the province of Tucumán. The first event occurred on August 3, 1920; the catalog reaches until 1977. The epi-

center locations are highly erroneous, particularly before the 1960s, before the set-up of the World-Wide Standardized Seismographs Network (WWSSN). Sparse global sensor coverage and limited computational power lead to low location accuracy. Hence, the location errors for instrumental records shown in Figure 1.4 were set manually to $\pm 0.5^\circ$ for all events before 1961. The same values were applied on events with seemingly manually fixed locations (i.e., both, latitude and longitude values ending on .0 or .5). Later events were assigned with $\pm 0.1^\circ$ errors, as location accuracy increased through time.

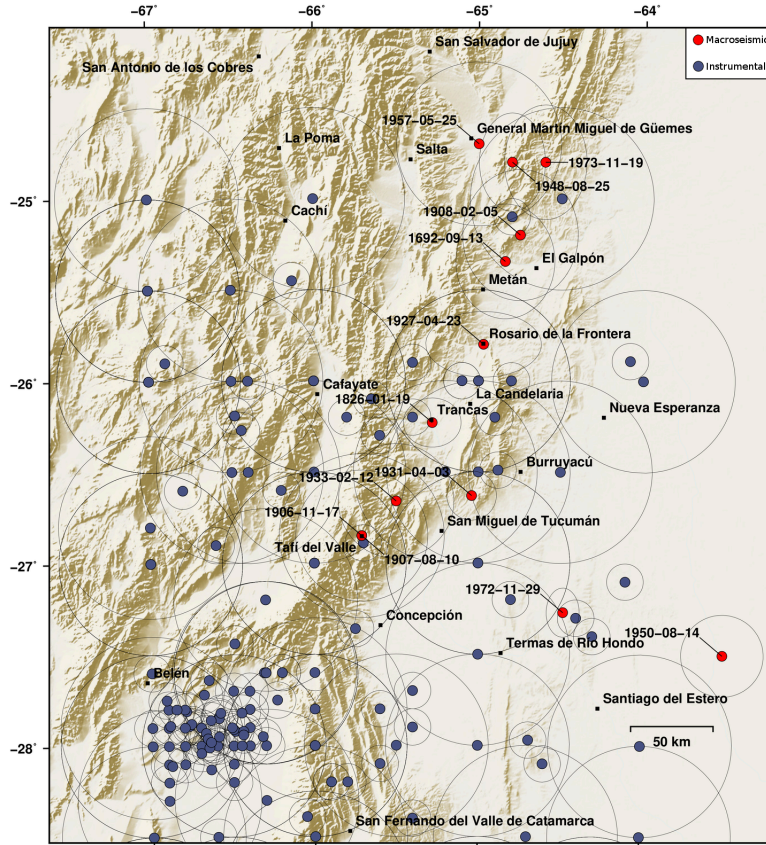


Figure 1.4: Map of historical (red points) and instrumental (blue points) earthquake locations after Zossi 1979 [61]. The historical epicenter locations are solely estimated from macroseismic information and range from September 13, 1692, until November 19, 1973. The first instrumental recorded epicenter is from August 3, 1920. Error estimations are shown as ellipses around each epicenter.

Unsurprisingly, the extensive spatial errors of the earthquakes shown in Figure 1.4 prevent their attribution to distinct structural features. Especially in east – west extension, the errors exceed the width of the frontal mountain ranges. Thus, various events can be associated to particular structures. Conversely, individual strong earthquakes cannot be

assigned unambiguously to a mapped fault. For example, exploring and uniquely identifying the source structure responsible for the 1692 Esteco earthquake is improbable. Further noteworthy earthquakes in the study area are:

- **Trancas** January 19, 1826: Macroseismic reports of damages from villages all over the Choromoro basin (e.g., El Tala, La Candelaria, Zárate). The maximum macroseismic intensity of IX reported for the settlement of Trancas. Thus, Zossi [61] estimated an $M_{6.5}$ for this event.
- **El Rey I** February 5, 1908: An intensity map indicates an epicenter close to the Esteco epicenter. Affected cities located all around the Metán basin (e.g., Metán, Rio Pedras, Juramento, Güemes, Rosario de la Frontera, San Antonio), while it was also felt in distant provinces such as Jujuy and Santa Fé (> 400 km). Estimated intensities at VIII and magnitude $M_{6.5}$.
- **Rosario de la Frontera** April 23, 1927: The reported maximum intensities VII leads to an $M_{6.1}$ estimation. Epicenter estimations are missing, thus for Figure 1.4 the present-day center of the city of Rosario de la Frontera is used. Multiple aftershocks sometimes with strong shaking are described in historical sources.
- **Salta** August 25, 1948: The epicenter estimation is close to the location of the El Rey I event, north of the Metán basin; derived from detailed newspaper shake reports, this results in smaller location uncertainty than from instrumental records. However, the instrumental magnitude estimation of $M_{6.2}$ given by Zossi [61] differs from an M_7 estimation from macroseismic analysis with a maximum intensity of VIII, while global observatories list $MS_{7.1}[1]$ for this event.
- **El Rey II** November 19, 1973: Similar epicenter as for the 1908 and 1948 events is estimated, at the northern end of the study area. Macroseismic reports for this event are limited, but present a maximum intensity IX on the Mercalli-scale. Magnitude estimations from regional and teleseismic analyses suggest a magnitude ranges from $M_{5.9}$ to $M_{6.1}$, with an $M_{5.4}$ aftershock five hours after the main shock.
- **El Galpón** October 17, 2015: The most recent $M_W 5.7$ event is described in the following Section 1.3.

All of these events reveal recurrences of severe and destructive earthquakes on a decadal to centennial time scale. The strongest of these events (from macroseismic information) somehow align with each other roughly from NNE to SSW through the study area (see Figure 1.4) and confine at the mountain front. Taking into account the large errors, several of the presented instrumentally recorded events can be clustered around the same area.

This overview displays the importance of a precise seismological study to understand the framework of geophysical parameters; characterizing the tectonic forces and their spatial and general boundary conditions leads towards a substantially improve understanding of the actual seismic hazard potential in the Argentine Central Andean Foreland.

1.3 The 2015 El Galpón Event

The need for a better understanding of the neotectonic settings of the Central Andean Foreland region for hazard and risk mitigation efforts became evident on October 17, 2015, when an M_W 5.7¹ earthquake occurred in close vicinity to the village El Galpón in the Salta province.

1.3.1 Macroseismic Event Description

During the shaking people fled onto the streets, while several buildings were destroyed to the degree, that rendered them uninhabitable. Fortunately, the event occurred on a Saturday morning, so public buildings were empty. This may explain the low number of fatalities, despite the fact that several buildings partly collapsed, e.g., the school building (see Figure 1.5). A typical destruction pattern all through the village was the collapse of western walls towards the west and onto the street. In archaeoseismological studies ([65], [66], [67]) seismogenic destruction patterns of ancient ruins have been analyzed and modeled to estimate ground motion parameters. Following Schweppe et al.[68], either (1) the wall collapses in the direction of horizontal ground motion during the stopping phase of the cycloidal pulse or (2) the wall falls due to the high inertial forces in the opposite direction of the ground motion. Thus, the most intense shaking in El Galpón must have occurred in an east – west direction. In detail, a maximum negative acceleration towards the west or a maximum positive acceleration towards the east can produce such a pattern.

The described pattern of damage was only found in the center of El Galpón. On average, buildings in the city center are older and were constructed without modern building codes using reinforced concrete frames[69]. As shown in Figure 1.5, the east – West ground motion not only introduced collapse and tilting of walls. In addition, perpendicular oriented internal walls experienced extensional forces, when neighbouring walls collapsed. These walls showed tensile cracks and were slightly separated from the remaining structures.

Besides structural damages on buildings, geologically noteworthy co-seismic effects were also reported. The national road No. 16 passes by the earthquake epicenter and displayed settling cracks along the embankment. At one site (Figure 1.6), the asphalt was ruptured perpendicularly and with the same strike as the fault orientation suggested by moment tensor inversion (see Table A.2). Similar structures could be found 2 km to the south at several aligning spots. This part of the Metán basin incorporates hot springs at the same location, where these surface offsets were observed. Unfortunately, due to dense vegetation cover, it was only possible to follow those structures further along-strike for several meters. Here, a vertical offset of a few centimeters appeared, where the eastern side was dislocated above the western part. The strike of these cracks was consistently close to N-S. During the period shortly after the earthquake, the composition of the water of the hot springs changed. Locals reported that after the event, the hyperthermal water

¹<https://geofon.gfz-potsdam.de/eqinfo/event.php?id=gfz2015uixg>



Figure 1.5: Images of destruction patterns in El Galpón I took five months after the earthquake. Image A: Facing north. The west-facing wall collapsed to the left, while the perpendicular wall shows crack patterns related to the extensional forcing. Image B: Facing south. The western wall tilts towards the west and is supported by wooden planks against further damage. Image C: Facing southeast. It shows the former school building where the western wall and the roof collapsed.

contained muddy sediments. Usually, the water is clear and has temperatures ranging between 46 and 63 degrees Celsius [70].

In the first week after the mainshock, more than 70 aftershocks were reported by locals. The lower magnitude threshold of earthquakes with sensitive shaking can be derived from the correlation of reported shaking in El Galpón with catalog data from our temporal seismological network installation (see Section 2.2). The aftershocks appeared



Figure 1.6: Superficial cracks in the epicenter region. *Top*: Crack at the national road rupturing the asphalt perpendicularly. Facing south. Dislocation crack was already remodeled. *Lower*: Surface crack close to a hot spring; facing north. Along several tens of meters, a vertical offset in cm-range could be traced.

consistently around the mainshock origin and thus present homogeneous epicentral distances with persistent damping of the emitted wave field. The smallest event magnitudes with reported shaking are ML 3.2. In comparison, the public event catalog of the Argentine national seismological service INPRES (*Instituto Nacional de Prevención Sísmica*) missed one of those felt events (see: Table A.1).

1.3.2 Teleseismic Source Information

Due to the strength of the mainshock, several seismological observatories list this event in their global catalogs [1]. Epicenter locations vary up to 20 km. Depth solutions range between 10 km and 33 km, while the majority give values of approximately 21 km. In comparison to similar tectonic regions such as Central Asia [71], the focal depth lies at the

deeper end of crustal seismicity in a mountain belt foreland. The lack of seismic stations in close proximity to the epicenter hinders an accurate determination of the hypocentral depth. The closest 3-component stations are at a distance of 128 km (station code: SLA) and 171 km (station code: AHML), respectively.

The moment tensor solutions for the 2015 El Galpón earthquake provided by different seismological observatories are consistent (see Figure A.2). They suggest as a first solution, a thrust event with a slightly oblique component on a nearly N-S-striking fault. For a thrust event, the dip angle is surprisingly steep (dip angle from 61° to 70°). When comparing Iaffa et al. [38] with the epicentral locations, the fault plane of the 2015 event coincides with the "Metán Basin Central Thrust Fault", which is a reactivated normal fault from the Cretaceous (it is inverted and shows the activity of a reverse fault). However, the dip direction of the fault mapped by Iaffa et al. opposes the moment tensor solution for the El Galpón earthquake. In addition, Iaffa et al. only analyzed seismic sections, their deeper detection limit of stratigraphy is given at 8280m, which does not cover the focal depth of the earthquake hypocenter. Hence, applying this method, no reliable information can be derived concerning the subsurface structure for the earthquake hypocenter.

Nevertheless, it cannot be excluded, that the mapped fault is the active structure responsible for the 2015 event. This would imply a strong hazard potential as the fault cuts through the whole Metán basin over a distance of 80 km. It could also be the subsurface structure that is responsible for the 1692 Esteco M7.3 earthquake showing the upper magnitude limit of observed, historical earthquakes. Therefore, a complete seismological study of the region as presented in this work is necessary, to fully understand those active structures and processes, which lead to potentially devastating earthquakes.

1.3.3 Hypocentral Depth Reestimation

The lack of local seismic stations and their sparse distribution in the epicentral region introduces a very high uncertainty regarding the hypocentral depth estimation. Teleseismic observations of depth phases enable a more robust estimation of focal depths [72] [73]. Depth phases pP and sP are upgoing P- or S-phases, which are reflected at the free surface. Differential travel times between direct and depth phases are nearly independent of the raypath between source and receiver, due to the near-vertical incidence angles at the surface. Instead, the local, crustal velocity structure and hypocentral depth of the event are the dominant factors controlling different arrival times.

Favorably using more distant receivers helps to reduce variations of the depth phase geometries, thereby minimizing depth phase incidence angles. Especially, for intermediate earthquakes such as the El Galpón earthquake, the signal-to-noise ratio may be close to one over large distances. Using data from seismological arrays (e.g. Yellowknife, Texas, Nevada, Pinedale or GERES) and stacking their waveforms using a "beamforming" approach [72] increases the signal-to-noise ratio compared to a single station by a factor of \sqrt{M} , where M represents the number of used stations in the array. [74] [75]

Before performing the beamforming for each array, synthetic back-azimuth and slowness values have to be calculated for each source - array combination [76]. Then, the

identified delay times can be used to align the waveform data along the desired phase onsets and stack them. By comparing the travel time differences of the array beam with a set of synthetic seismograms depicting various source depths, it is possible to identify the hypocentral depth precisely.

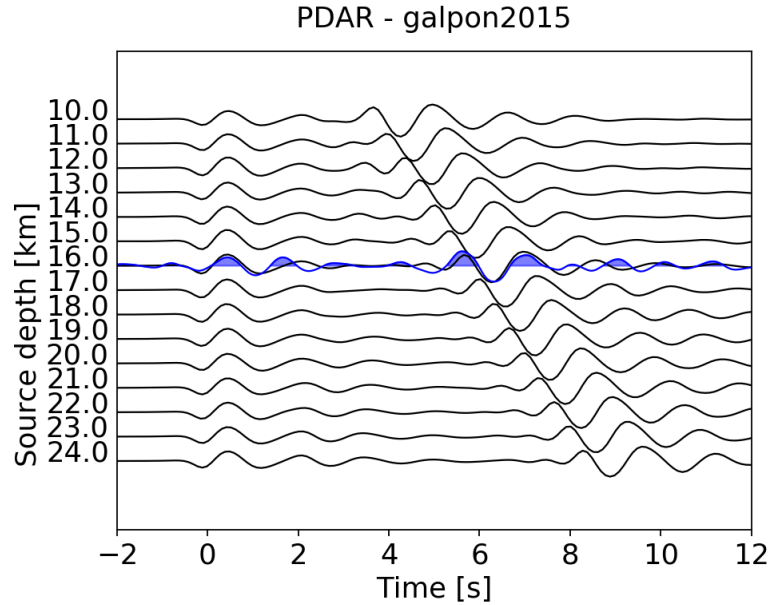


Figure 1.7: Result of the hypocentral depths estimation using teleseismic depth phases and the *ArrayBeamDepthTool*. Example calculated from data using the Pinedale-array. Blue: array beam data, aligned to a theoretical depth of 16 km. Black: synthetic seismograms with varying source depth, between 10 and 25 km.

The *ArrayBeamDepthTool*² presents an efficient tool to perform the depth estimation as described above. This python-based software package provides a completely automatic tool, starting with data queries of array meta-data and waveforms from IRIS [77], Geofon[78] and BGR data centers [79]. The calculation of synthetic back-azimuth and slowness values is performed using the pyrocko cake module[76], which calculates travel-time tables for 1-D layered media. The waveform data is restituted before stacking, to match the units of the synthetic waveforms. The Green’s functions database, necessary for the calculation of synthetic seismograms, is generated with the pyrocko fomosto module; fomosto uses the fortran based QSEIS[80] code as its backend. Input velocity models are the local velocity model derived in Chapter 5 underlain with the AK135 [81] global velocity model on the source side and a combination of the CRUST2.0 [82] [83] and the AK135 model for the receiver part of the Green’s function. From visual alignment of the array beam with a set of synthetic waveforms, the source depth can be estimated.

²<https://github.com/HerrMuellerluedenscheid/ArrayBeamDepthTool>

The resulting depth estimations are consistent between different arrays measuring from approximately 16 (e.g., Pinedale array) to 16.4 km (e.g., Texas array). This is also true using different velocity models, however the absolute depth values differ. As the depth estimation from teleseismic depth phases only depends on the local velocity structure above the hypocenter [73], the use of a global velocity model would lead to higher velocities in the crust (see chapter 5) and thus lead to a deeper source. Hence, the use of a Crust2.0 model for the seismic velocities around the source results in hypocentral depths of between 17 and 17.5 km. Nevertheless, the estimated values are robust and add reliable information for the analysis of the 2015 El Galpón earthquake.

2 Topic I: Seismological Field Instrumentation

The seismological investigation in its entirety necessitates several methodological approaches to cover the multiplicity of geoscientific processes. A key method in the presented seismotectonic work is the installation of a temporary seismological network, combined with the processing and interpretation of its recorded data. A combination of thorough planning as well as an in-depth analysis of the 2015 El Galpón earthquake is crucial for a successful comprehensive study. As described in the introduction (see Section 1.1 and 1.3.2), the lack of data prior to this study limits the investigation of the source processes of the 2015 El Galpón earthquake (see Section 1.3). To overcome the scarcity of seismotectonic data, several field campaigns were carried out. This not only makes it possible to generate a more complete data-set in general but also helps to perform the study with high confidence.

2.1 Damage Identification

Five months after the El Galpón earthquake the first field campaign was realized. To get a first impression of the shaking and the impact of the seismic event, the village of El Galpón in short epicentral distance was visited. At first, the structural damage of the buildings throughout the town was examined. These observations are discussed in the Section 1.3. Interviews with inhabitants who experienced the earthquake gave further insight into the maximum shaking and distribution of aftershocks in intensity and over time (see Table A.1). Locals also shared their pictures taken directly after the earthquake. Rural residents gave access to areas of geologically interesting destruction patterns, e.g., possible fault scarps, hot springs and settlement damage. This geological insight helps to identify markers clarifying the contrast between the moment tensor solutions and the geometries of faults mapped in seismic lines. Previous geological studies in the area led to various fault geometries and different tectonic interpretations of identified structures.

Connecting with local decision-makers and politicians was crucial to receive information about interesting scientific sites associated with the earthquake. Furthermore, they supported the following seismological survey to install a temporal seismic network and assisted in the choice of sites for the deployment of stations. Thus – depending on the availability of installation sites – further planning and decisions included information provided by locals.

2.2 STRATEGY - Temporal Seismic Network

The overall task of this work is the seismological and seismotectonic analysis of the NW Argentine Central Andean Foreland. The monitoring of active seismotectonic processes is crucial to investigate both the driving forces and the subsurface architecture, which lead to potential seismic hazard. Thus, 13 temporary seismic stations intended to monitor the microseismicity in the foreland were installed. After the occurrence of the 2015 El Galpón earthquake, the initially planned survey was adapted.

2.2.1 Network installation

Based on information derived from previous geological [6] [34], geophysical [38], [24] and seismological studies [15] [17], in combination with new information gathered during the field campaigns, potentially seismotectonically active regions and structures were identified. The orographic features *Cerro Colorado* and *Sierra de la Candelaria* ranges (see map in Figure 2.1) were selected as areas of particular interest in the study area. Their lithological composition reflects the different evolution of both ranges and represents the previously intended north to south transition of the neotectonic deformation regimes [86] within short distances. In order to lower the detection threshold of the seismic network and improve the hypocenter determination, the interstation distance was reduced to an average of 20 km. Thus, it was possible to detect the low-magnitude aftershock events, the appearance of which is expected to decay over time [87]. In addition, from the spatio-temporal distribution of the aftershocks it may be possible to gather additional source parameters of the mainshock.

The final decision for a specific location to be used as a site for a seismic station was based on the following considerations:

1. **geological site conditions:** It is favorable to minimize the vertical distance to the bedrock. This increases the coupling of the station and results in a wider recorded signal spectrum. A thick sedimentary layer reduces the local wave velocities and introduces a systematic error in arrival times. In addition, the wave field scatters, introducing a strong wave coda and more emergent, difficult to pick phase onsets.
2. **remoteness:** The signal-to-noise ratio of the seismological data mainly depends on the distances to ambient noise sources. The choice of remote locations in the study area favors far distances from human settlements and infrastructures (e.g., roads, electric lines, cropping fields). In general, the region is characterized by a very low population density and a lack of major industry. Maintaining homogeneous interstation distances for a good network coverage, could not always be achieved. Some stations (e.g., 01A, 07A, 10A) had to be reinstalled in new locations, in order to reduce the impact of anthropogenic ambient noise sources.
3. **security:** In most locations it was preferred to install the seismic stations in sight distance to nearby houses so that, locals could detect problems with the stations and the stations would appear protected. Even though, one station (02A) was lost

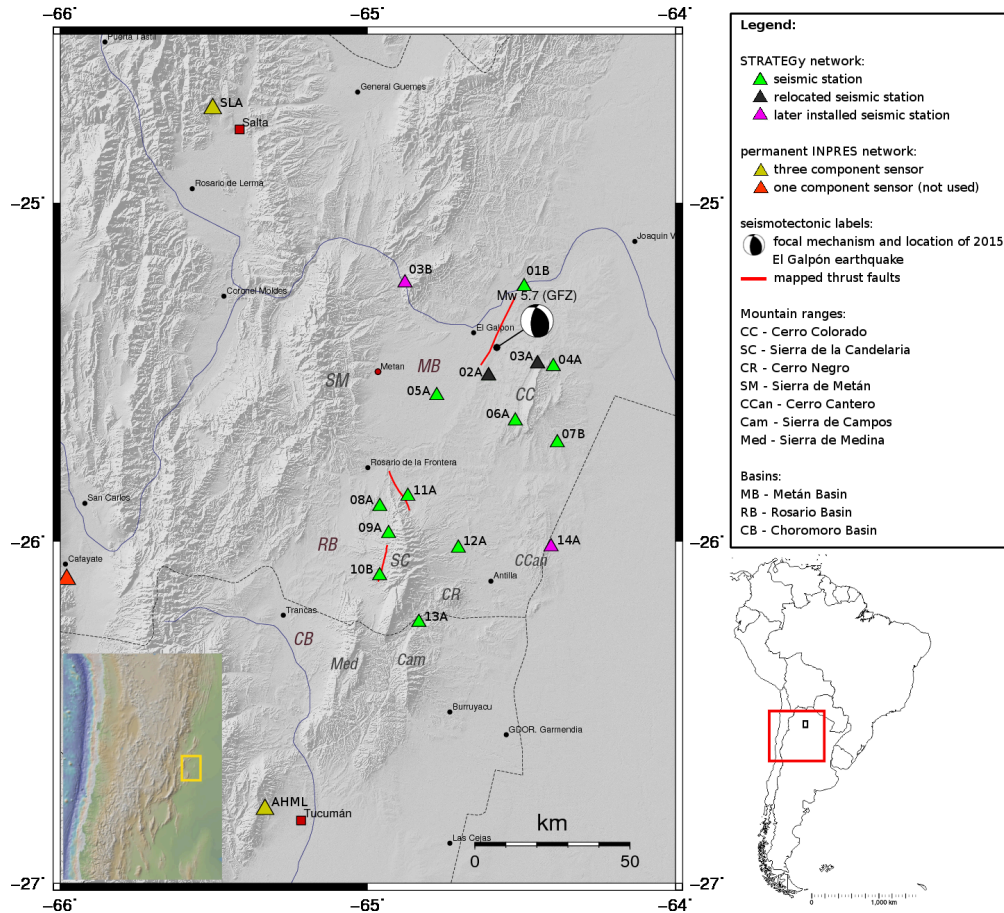


Figure 2.1: A map of the study area with all available temporal [16] and permanent [84] seismic stations during the survey. The location of the 2015 El Galpón earthquake is shown with the corresponding focal mechanism. Red lines indicate the location of previously mapped faults [85]. Discussed major topographic features are labeled with abbreviations. Inset maps show political borders (lower right) with the location of the other maps and DEM of the Central Andes (lower left).

due to a robbery and one station (13A) was temporarily damaged due to animal chewing on the power cables (see Section 2.2.3).

Each station consisted out of a Lennartz 3D 5s¹ intermediate broadband seismometer, except for the later installed station 14A, which was instrumented with a Mark L-4C-3D² short-period sensor. The analog 100 Hz data output was digitized (with 23 bit) and

¹<http://www.lennartz-electronic.de/index.php/seismometers-en/le-3d-5s>

²<https://www.passcal.nmt.edu/content/instrumentation/sensors/short-period-sensors/l-4c>

stored on DATA-CUBE³ type 2³. Those instruments use an external GPS-antenna to receive timestamps for correcting the internal clock drift. The power supply was provided by batteries, which were recharged by solar panels during the day. The equipment was provided by the University of Potsdam.

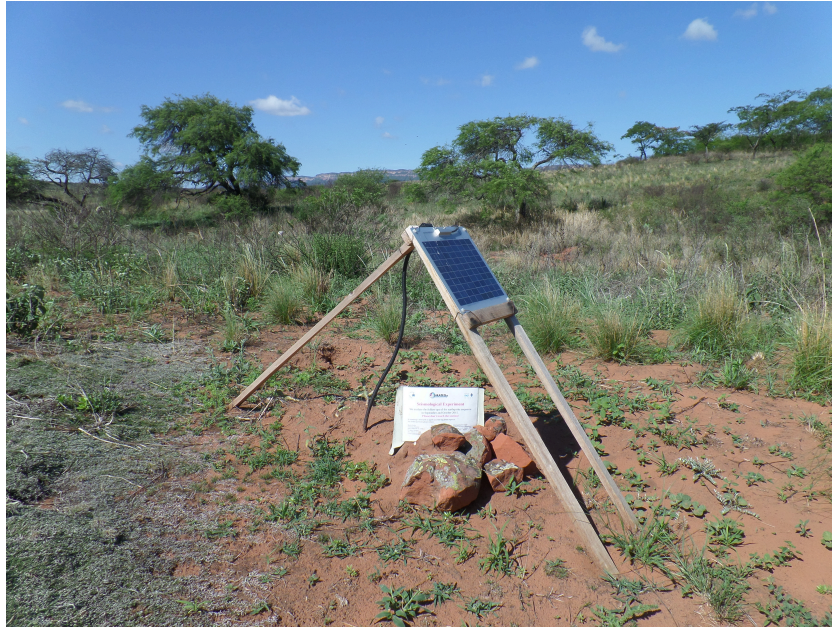


Figure 2.2: Image of station 04A in the field. The solar panel (oriented to the north) and GPS-antenna were placed at the surface. The sensor and all electrical equipment were dug into the ground and placed under the solar panel; here covered and secured by rocks.

During the installation the horizontal components of the seismometers were arranged to magnetic north. The magnetic declination in the study area ranges between -7.5° and -8.5° , for which the recorded data were not corrected. The sensors were placed in holes at a depth of approximately 60 cm, except for station 03B, for which a 2 m deep concrete basement existed. Solar panels and GPS – antennas were placed on a wooden frame facing north at a height of 1 m, to prevent shadowing from the surrounding vegetation during the austral summer. The remaining electrical parts of the stations were placed below a pile of soil. This prevented heating from insolation and reduced the impact of the seasonal rainfall events. With this set-up the seismic stations run autarkically and the recorded data was read out manually every five months on average.

The total recording period was 15 months, starting in June 2016 and ending in August 2017. The network set-up was adjusted twice during the recording period. First, the station 03A was moved to the new position 03B to reduce redundancy with station 04A as their interstation distance was only 5 km. In cooperation with INPRES, established

³<https://digos.eu/seismology-and-cubes/>

during the project, it was possible to install the station 03B in the location of a former permanent station, which was abandoned due to data transmission issues. Also, the data of two stations (AHML and SLA) from the national permanent network [84] close to the temporal network could be incorporated into the analysis. Unfortunately, the data was not recorded continuously due to heavy monsoonal precipitation flooding several stations (see Section 2.2.3) and the loss of one station due to robbery. Later, the station 14A could be added and the network extended to the southeast. This location was chosen in order to improve the azimuthal coverage of earthquakes in the center of the network, which had been identified and located during the first data analysis period. In addition, several events were identified between the *Sierra de la Candelaria* and the Cerro Cantero. Station 14A increased the robustness and lowered the detection threshold for those events.

2.2.2 Data Quality

The use of a stochastic based analysis method facilitates the comparability between stations and whole networks. Probabilistic Power Spectral Densities (PPSDs) are standard methods to calculate ambient seismic background noise (for method description see [88]). This method helps to decipher stations with probable higher noise levels, leading to higher detection thresholds of seismic events. Further, temporal variations and bandwidth limitations due to ambient or anthropogenic noise sources can be identified. The analysis of the full, continuous waveforms allows the evaluation of station performance in the full spectral range of the instruments.

In Figure 2.3, the PPSD of station 06A for the first three months of data recording is given as an example. Here, the calculation of PPSDs is based on the implementation in the ObsPy-package [90]. All long period signals above 10 seconds are negligible as those frequencies do not lie within the recording bandwidth of the Lennartz 5 s instruments and represent the instrument self-noise. The periods between 1 s and 10 s are dominated by ocean microseism [91] [92]. Its influence becomes evident in the New Higher Noise Model (NHNM) and New Lower Noise Model (NLNM), which represents the expected ambient noise range for seismic stations, estimated on a global scale range [89]. For the seismotectonic study performed here, the frequency range between 2 s to 15 Hz is of highest interest. Dominant frequencies of seismic waves recorded from earthquakes in local distances are expected to fall into that range. All higher frequencies can be assigned to cultural noise, with possible diurnal variations.

The most energetic periods are from oceanic microseismic sources, but the measured amplitudes lie just 10 dB above the NLNM. This indicates a low noise level compared to global averages. In the seismotectonically interesting bandwidth, the amplitudes present a flat plateau 20 dB above the NLNM. These are good results for a temporal installation, highlighting the importance of station remoteness.

To make the noise level comparable throughout all stations in the STRATEGy-network, the mode of each PPSD is used as the main discriminative parameter. Due to the probabilistic character of the PPSD, the mode describes the most probable amplitude value for each frequency band throughout the continuously recorded wavefield. Figure

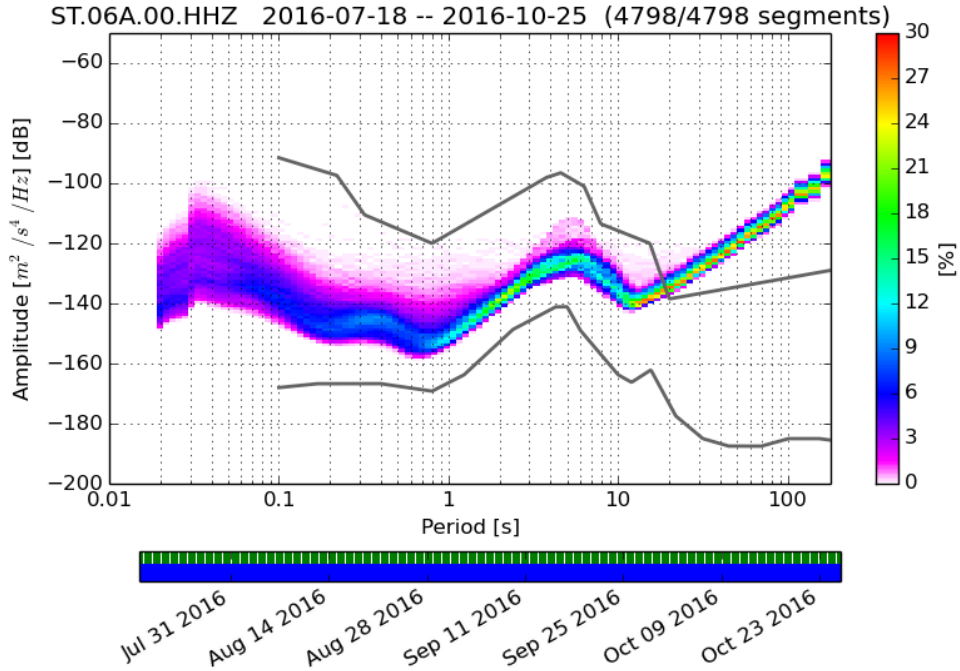


Figure 2.3: PPSD plot of station 06A (see map 2.1) with three months of continuous data (lower bar). The color-coded plot shows the most probable occurrence of seismic velocity amplitudes for each period. In grey the New Lower Noise Model and New Higher Noise Model (see Peterson 1993 [89]) are given as expected possible lower and upper limits, respectively.

2.4 visualizes the frequency depending noise deviation in the STRATEGy-network, using the mode PPSD for each station. Due to the instrumental detection limit, signals below 5 s were canceled out. Similarly, the noise analysis was limited to 15 Hz, which reflects the upper limit of expected seismotectonically interesting signal frequencies.

The most probable amplitudes for the second-order oceanic microseism frequency range are very consistent. Only station 05A shows slightly higher amplitudes in the full microseism range, due to site effects of the thick sediment lithology within the Metán basin, amplifying the signal [93]. A clear correlation of decreasing oceanic noise with increasing distance from the Pacific coast is not visible in the dataset. Except for station 05A, the signal amplitude ranges vary less than 8 dB between one another. In contrast, cultural noise levels vary intensively up to 40 dB within the network. Some stations show an increase noise level towards higher frequencies, while others remain stable or show a noise amplitude peak at lower frequencies.

Discriminating the sources of the varying noise levels throughout the network is tackled by a spatial approach in Figure 2.5. From the previously discussed mode of the PPSD

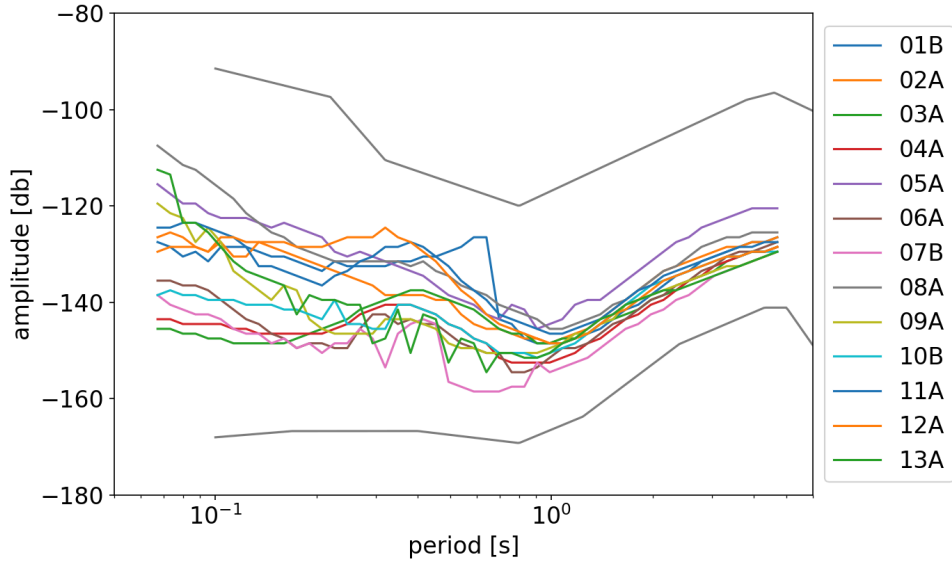


Figure 2.4: Mode PPSDs for all stations within the seismotectonically frequency bandwidth. Color-coding with respect to each station. Grey lines indicate NLNM and NHNM [89]. Above 1 s, the noise is dominated by second-order oceanic microseism and below by cultural noise.

of each station, the difference to the NLNM is calculated for each period bin between 5 s and 15 Hz. Then, averaging the mode difference returns a single value discriminator to label the noise station for all stations.

Two centers of reduced noise levels are visible around the two mountain ranges *Cerro Colorado* in the northeast and the *Sierra de la Candelaria* in the southwest of the study area. This result confirms the efficiency of a remote selection of sites, as described in section 2.2.1. Additionally, those sites characterize small vertical distances to the bedrock. In contrast, stations close to highways in the north of the *Sierra de la Candelaria* (e.g., 08A, 11A, 12A) and in the northwest of the study area (e.g., 03B, 01B, 02A) show an elevated noise level (compare "rule of thumb" in Bormann & Wielandt [93]). Both effects, lithological subsurface conditions and station remoteness, superimpose each other and it is difficult to argue each contributions. Station 05A shows the highest noise levels; besides the thick soil and sedimentary layers in the subsurface, it is surrounded by high-intensity cropland [94]. Hence, less remote stations show an elevated noise level but are still useful for further analysis.

2.2.3 Data Loss

During the 15 months temporary installation of the STRATEGY-network, several stations did not work continuously due to different issues. The station 02A was stolen in

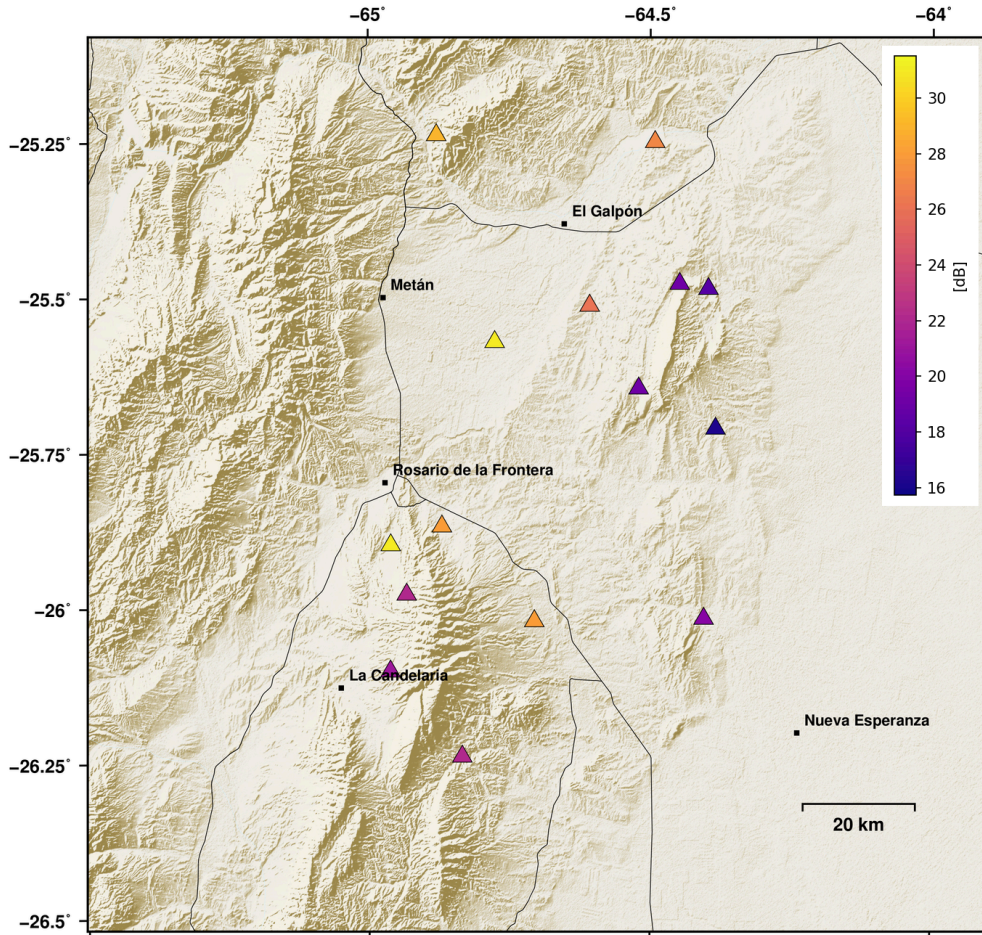


Figure 2.5: Topographic map of the STRATEGY network, with its stations as triangles color-coded by the average noise amplitude difference to the NLNM[89]. Black lines indicate major roads in the study area.

January 2017, but the last data collection was in November 2016. Thus, this station only recorded five months (158 days) in total. Externally forced interruptions occurred at station 13A March 29, 2017, when local farm animals interrupted the power supply by chewing the solar panel cables. This problem was solved, and the interruption lasted no longer than 32 days. Power shortage due to technical failure occurred at station 06A January 21, 2017, and remained unnoticed until May 18, 2017.

Major recording shortage occurred during the austral summer months. Budget limitations for the temporary installation did not allow us to install a fully protected station, comparable to standards in permanent installations (i.e., station 03B, in a hut with concrete basement). The climate in the study area is characterized by high summer-monsoon precipitation, transported through the South American low-level jet along the

eastern flanks of the Andes [13]. At least 70% of the DJF rainfall in the region is contributed by extreme rainfall events [95]. Thus, measured peak precipitation can reach up to 60 mm in 30 minutes in localized, single rainfall events [96]. Such extreme rainfall events led to complete technical failure of multiple stations in the network. In most of the cases, water drained into the supply bags and led to corrosion of the power supply parts (e.g. battery or solar charger).

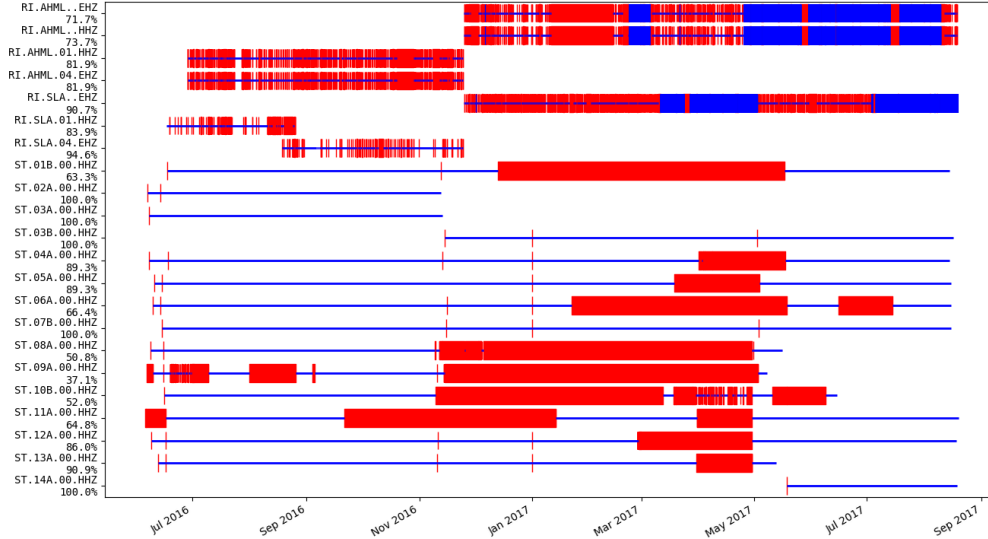


Figure 2.6: Plot of available data of all stations during the temporal installation of the STRATEGy network, also including the INPRES stations (network code RI). Blue horizontal lines indicate continuously available waveform data. Red vertical lines indicate data gaps.

Figure 2.6 presents an overview of time spans during the installation with a reduced number of working stations. The first stations stopped working in November 2016, with the onset of the monsoon season. Other stations malfunctioned in March or April 2017. The large number of damaged stations has an impact on the later interpretation of the seismological data-set. For several weeks, only two stations were working. Hence, the unambiguous localization of earthquakes is not possible during that time, only their detection. In addition, the incremental reduction of available stations raises the detection threshold of events and introduces an unstable magnitude of completeness for the earthquake catalog. A temporal interpretation of earthquake occurrences should be avoided or strongly consider the number and location of available stations in the network.

Although the inclusion of two stations from the national seismological permanent network improves the azimuthal and epicentral coverage of the network, those stations also suffered from data-loss due to data transmission issues. Both stations cover the full recording time of the STRATEGy network, but show very short period data gaps. In addition, the station San Lorenzo (SLA) has only intermediate band data (e.g., HHZ)

for the first three months. Later only short period data (e.g., EHZ) is available. For the purpose of picking arrival times of local earthquakes, this bandwidth is sufficient.

2.2.4 Data Publishing

The seismological data is published with the FDSN network code 2S(2016-2017) (see Zeckra et al. [16]). The data access is restricted for the first five years and will be released on January 1, 2022. The network is named "seismic network/array in Northwestern Argentina", with the acronym STRATEGy. The primary purpose of the instrumentation was intended to function as a local seismic network, recording local seismicity. But, due to its set-up with average interstation distances of around 20 km, it can also be used as a seismic array for events at regional (i.e., intermediate-depth earthquakes at the subduction plate interface at around 200 km depth underneath the Puna plateau) or teleseismic distances (i.e., an M_W 7.4 earthquake in South Georgia Island Region⁴ was recorded, with aftershock detection limits of unstacked traces down to a magnitude of m_b 4.5). In addition, the network geometry allows a separation of the array into a northern and a southern array with six to seven stations each.

2.3 Instrument Validation - Huddle Test

Before and after the installation of the network, a lab-based instrument validation test was performed with all seismic sensors. This test is based on Havskov and Alguacil 2004 [97] and is called the *huddle-test*. This experiment aims to control all sensors and determine their instrument response. This is needed for further processing steps (see Section 4.2), i.e., to reconstitute the recorded waveforms to ground displacement. In addition, this test helps to identify malfunctioning sensors, as they were used in previous surveys and their hardware components can be altered. After the installation in northwest Argentina, the experiment was executed once more, in order to assure consistency throughout the survey.

2.3.1 Method

In Figure 2.7 the instrument set-up is shown. All sensors were installed in close proximity to each other. As a result, the lateral variance of the recorded signals is minimized as the interstation distance is negligible in comparison to the raypath distance to the sources, and therefore the recorded signal is highly correlated. This experiment is favorably performed in a location with a high noise level, so the instrument self-noise is well below the mean signal amplitude. The total recording time spans several days, so sufficient correlated signals could be recorded. Several earthquakes were recorded during the huddle-test (before and after the temporal installation) in Potsdam-Golm, Germany. The events used for further analysis occurred:

⁴<https://geofon.gfz-potsdam.de/eqinfo/event.php?id=gfz2016qqd>



Figure 2.7: All seismometers were aligned during the lab-based huddle test, before the deployment in the field. Data-Cube digitizers and sensors were powered by batteries.

1. APRIL 10, 2016⁵: Afghanistan-Tajikistan Border Region, source time: 10:28:58.6 UTC, M_W 6.6, source depth: 210 km. The records for this events were used to determine the instrument responses before the temporal installation.
2. JANUARY 5, 2019⁶: Western Brazil, source time: 19:25:38.4 UTC, M_W 6.7, source depth: 573 km. This event was used for the experiment after the field installation.

With the presented experiment set-up, it is assumed that all sensors experience the same ground motion. Even during the recording of the arriving wave field, it is not applicable, that the recorded signal is noise-free. The mathematical approach uses the cross-spectrum to calculate the transfer functions, to cancel out the noise. If the transfer function (T_1) for one instrument is known, the unknown transfer function (T_2) of a second instrument can be calculated with the formula 2.1. $P_{11}(\omega)$ is the power spectrum of the output of the known sensor, and $P_{21}(\omega)$ is the cross-spectrum between the outputs of the known and the unknown sensor.

$$T_2(\omega) = T_1(\omega) \frac{P_{21}(\omega)}{P_{11}(\omega)} \quad (2.1)$$

Under the assumption that the poles and zeros given by the manufacturer are correct for one sensor, the relative transfer function of a second sensor can be calculated using formula 2.1. Afterwards, the instrument parameters poles, zeros and gain have to be determined by an optimization process, while minimizing the complex L2-Norm of a simulated transfer function with the calculated transfer function T_2 in formula 2.1. This has to be performed for all sensor – sensor permutations.

⁵<https://geofon.gfz-potsdam.de/eqinfo/event.php?id=gfz2016hbnc>

⁶<https://geofon.gfz-potsdam.de/eqinfo/event.php?id=gfz2019aiuk>

The software to perform and reproduce the huddle-test presented here is available in a public software repository ⁷. It is written in Python using the widely used ObsPy package [90] [98]. The inversion step is realized using the external dinver plugin, which comes with the Geopsy software-package ⁸.

2.3.2 Results

Poles	Zeros	Gain
$-0.888 + 0.888i$	$0 + 0i$	400
$-0.888 - 0.888i$	$0 + 0i$	
$-0.29 + 0i$	$0 + 0i$	

Table 2.1: Poles and Zeros for Lennartz instruments as given by the manufacturer. These values were used as input for the known transfer function T_1 in equation 2.1.

The inversion aims to optimize for six free parameters, three parameters for the real part of the poles, the imaginary part of the first two poles, and the gain factor. The zeros are not considered as they are true complex zeros. In addition, the imaginary part of the third pole is set to zero as a priori information given by the manufacturer.

The resulting estimated poles of all instrument combinations can be inspected visually in Figure 2.8. The calculated poles of the transfer functions of all instrument combinations are displayed in the complex plane. Most of the calculated parameters fall into a close range around the expected theoretical values. Six values differ stronger from the theoretical values. Those values show abnormally high misfit values after the last inversion step (in Figure 2.8 orange dots with misfit values greater than 20) and can be interpreted as local minima from improper exploration of the solution space. These outliers neither relate to a specific station nor occur in the reversed sensor – sensor combination. The gain values follow a normal distribution with a mean value of 400 and a standard deviation of 18.6. To sum up, the non-analytical approximations of the transfer functions fall into a reliable solution range.

This experiment was performed before and after the survey to assure the consistency of the recorded data. In Figure 2.8, the experiment results, post-installation, are presented. The poles and zeros estimations before the installation show very similar results with comparable variance. Hence, the instrument response is constant throughout the whole survey, and no significant harm occurred to the instruments themselves.

⁷<https://github.com/marzeck/seismo-huddle.git>

⁸<http://www.geopsy.org/index.html>

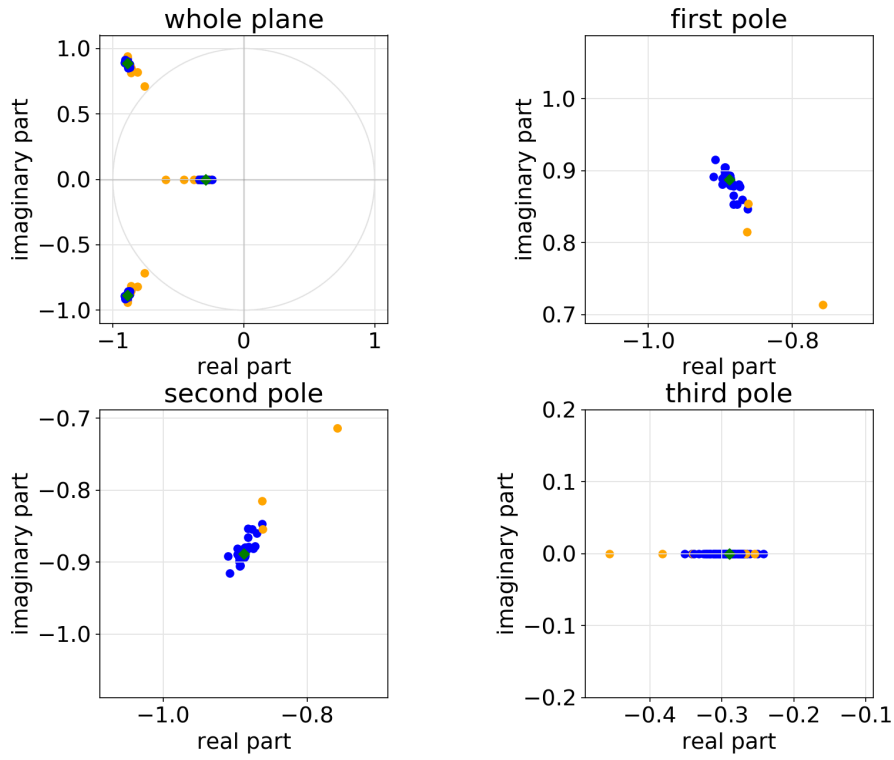


Figure 2.8: Visualization of the resulting poles with all sensor – sensor combinations. In the upper left plot, the whole complex plane with all poles is shown. The other Figures give a close-up view of the three instrument poles. Green diamonds represent theoretical poles as presented in Table 2.1. Blue dots show the inversion results of the calculated transfer function for all instrument combinations. Orange dots show poles with misfits greater than 20.

3 Topic II: Event Identification

In Seismology a vast range of processing software has been developed over decades, mostly to assist in finding solutions for specific research tasks, for example, permanent data acquisition and real-time data processing at observatories (e.g. earthworm [99], SEISAN [100], seiscomp3 [101] [102]), relocation of existing earthquake catalogs [103] or source modeling with moment tensor inversion [104] [105]. With increasing computational power, the solution of higher degree numerical problems has become more applicable over time, i.e., using big data sets [106], incorporating remote sensing deformation data into source modeling [107] [108] [109], implementing deep learning approaches [110] [111] [112] or Bayesian sampling algorithms [113].

To fulfill the specific task of a tectonically focused analysis of the seismological dataset, the implementation of a Python based workflow was favored over the use of fully implemented rigid software packages. This allows high adaptability to the scientific task and full control of the methods used in each processing step. In detail, the presented workflow composes of previously existing FORTRAN based software (e.g. Hyposat [114]) in combination with Python packages, developed for seismological tasks [90] [76]. While the latter was favored due to higher computational efficiency (increase of computation speed up to a factor of 10).

The data handling uses two distinct categories of formats. First, the continuous waveform data is stored in the MiniSEED data format ¹ (further as mseed). This binary file format was developed from the SEED (Standard for the Exchange of Earthquake Data) format to serve the special needs of seismological data processing and minimizes storage space thanks to the applied data compression. Its development was driven by members of the Federation of Digital Seismographic Networks (FDSN). The second category comprises XML-based (eXtensible Markup Language) file formats. These formats are plain-text based, therefore human and machine-readable, platform-independent, and reduce computational efforts to load the data. The hierarchical structure of XML-type formats helps to sort the information for the user and reduce redundancy.

In detail, the network and station related meta-information is stored in the StationXML data format ². This schema definition represents MiniSEED metadata provided by the FDSN [115] as a modern seismological data standard. The hierarchical structure consists of three layers: network, station, and channel, each with vast numbers of optional parameters with flexible field width. Event-based information (i.e., event catalog with location and magnitudes) are stored in the QuakeML data format [116]. This XML-based scheme is community-approved by a public *Request for Comments* before the last development step to its current Version 1.2. The extensive hierarchical structure

¹<https://ds.iris.edu/ds/nodes/dmc/data/formats/miniseed/>

²<https://www.fdsn.org/xml/station/>

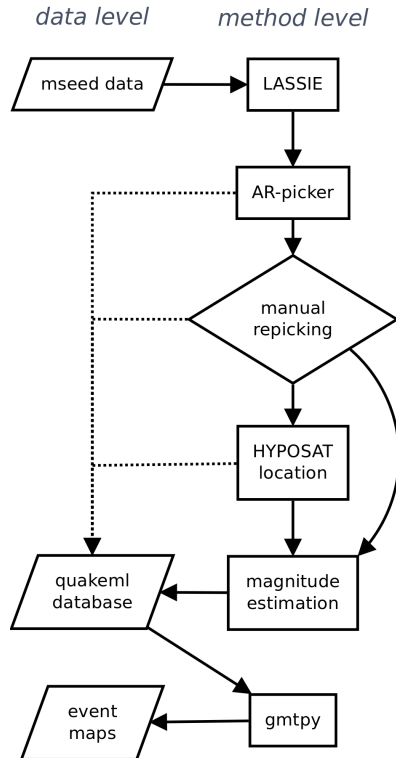


Figure 3.1: Workflow set-up for processing the seismological recorded data. On the left, the in- and output data handling is sketched, which is performed in most of the processing steps through the QuakeML file format. On the right, the nearly linear, semi-automatic processing chain from event identification to the full seismological catalog is sketched.

[117] allows the storage of intermediate processing results (e.g., picks, arrivals, station magnitudes) and several unambiguous solutions next to final, preferred solutions, i.e. testing different velocity models or location software. Explicit identification of results in the catalog is accomplished with *Uniform Resource Identifiers (URIs)* in all layers of the XML-scheme. This increases reproducibility and traceability of the final catalogs for other users who are not involved in the processing.

This chapter will provide insight into the processing of the seismological data, including event detection, and the identification of seismic phases. The semi-automatic workflow (see Figure 3.1) is implemented in Python and consists of event detection and automatic phase picking with manual verification. The following Chapter 4 describes the automatic processing of event location and magnitude estimation in order to set up a complete seismological event catalog. The semi-automatic approach was favored as high-grade automation minimizes processing time, while manual interaction guarantees robustness.

3.1 Event Detection - LASSIE

Scanning the continuous waveform data of a seismological data-set for earthquake induced signals manually is extremely time-consuming. Therefore, various approaches were developed, analyzing energy deviations in the data stream (e.g., STA/LTA triggers), using a priori information from known events (e.g., cross-correlation [118], template-matching [119]) or stochastic methods (e.g. Hidden-Markov-Models [120] [121]). The Hidden-Markov-Models have high computational effort and aim for simultaneously detection and classification of different source classes, which is not expected for the study area in NW Argentina. For the study area solely seismotectonic sources are expected in the recorded data, due to the absence of nearby mining (e.g., quarry blasts, mining explosions) and steep, erosive mountainous areas (e.g., landslides [122], debris-flows [123] or monsoon related elevated seismic noise [124]).

Furthermore, the limit of preceding seismological information prohibits the use of supervised learning methods. After the manual identification of useful STA/LTA trigger thresholds, the number of false alarms and missed events was unsatisfying, although the implementation is rather simple. The usage of network coincidence information increases robustness, but still not to the degree that manual inspection of the results could be avoided and, thus, lead to time-consuming post-processing.

Here, the unsupervised delay-and-stack method is used for earthquake detection. This method works on the full continuous waveforms and includes coincidence information of the whole network, as it exploits coherency of the waveforms. Hence, the event detection is independent of the identification of seismic phases (see Section 3.2). Nowadays, this approach is widely used and applied for different seismic source types, e.g., volcano-tectonic [125] [126], landslides [127], induced seismicity [128] [129]. A complete description of the delay-and-stack method is given in Cesca & Grigoli [130]. Further, a brief explanation is given here.

For an arbitrary source location (yellow star in Figure 3.2 a1) with an arbitrary source time, theoretical arrival times of the P- and S-phases are calculated for all stations in the known network geometry. Along these station-dependent arrival time windows, the recorded waveforms of all stations are translated into characteristic functions and stacked. Various stacking functions have been proposed and used so far as coherence measures:

- energy traces ([131], [132])
- envelope traces ([133], [134], [135])
- kurtosis traces ([126])
- STA/LTA traces ([125], [128], [136])

Repetitive stacking for all source locations within a predefined gridded volume results in single coherence values for each grid point. Theoretically, maximum coherence is expected for the true source location. In fact, the scanned source grid shows increased

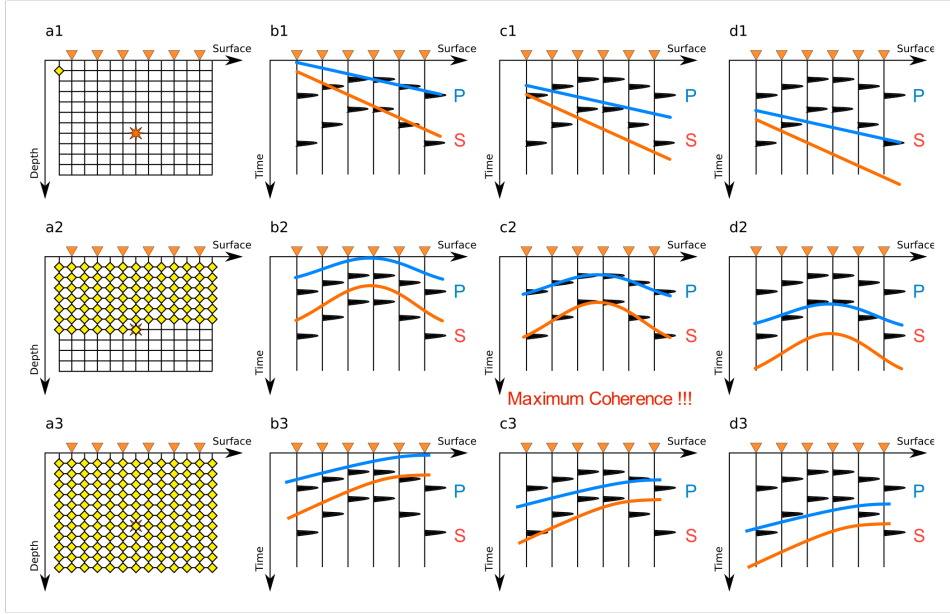


Figure 3.2: Sketch shows the process of stacking characteristic functions for different source locations in a predefined 2-D grid, with a line of seismometers on top of a homogeneous half-space. Theoretical arrival times for the P (blue) and S (orange) phases for different source locations are presented. Maximum coherence of the waveform stack (along the delay time, determined from theoretical arrival times) can be achieved in the true source location. Figure taken from [130]

coherence around the true source, so the 3D coherence matrix is scrutinized for the global maximum as the most probable source location.

The described method is implemented in the Lassie detector [129] [137]³. This Python-based software toolbox is published under the GNU General Public License, operates mainly with the pyrocko Python-package [76]. Pyrocko comes with a ray-tracer tool called cake. It can be used to solve classical seismic ray theory problems for layered-earth models on a spherical Earth. Here, cake is used to calculate the theoretical arrival times of direct P- and S-phases. The 1-D velocity model used is the Swiss model [138], which was calculated for a similar purpose and in a comparable region, including mountainous and foreland regions. Also a local velocity model of the study area was not available at this early stage of processing. Arbitrary source locations are taken from a gridded volume, with 2.5 km spatial resolution. The source volume covers the expected seismotectonically active and interesting region of the NW Argentine Andes and extends from the center of the STRATEGy network (-25.75° lat , -64.7° lon) 200 km to the west, 150 km to

³<https://gitext.gfz-potsdam.de/heimann/lassie.git>

the north, and 70 km to the east and south, respectively. Stacking functions along the theoretical arrival times differ for the expected seismic phase. For computation-efficiency and more stable detections, characteristic functions were calculated for the seismic waveforms before stacking. However, the outstanding performance of *Lassie* is achieved on the cost of larger location uncertainties [129]. The characteristic function for P-wave arrival times is based on STA/LTA, which makes the detector more sensitive to sharp onsets in the signal. S-waves are imaged through moving average functions, which performs better with the emergent S-phases. Prior to mapping into characteristic functions, the waveforms were bandpass-filtered and weighted afterwards. The S-waves carry more energy in their wavefield and the different characteristic functions compensate for that. Finally, the stacked characteristic functions are thresholded, and above a critical (dimensionless) value the detection is triggered. Thus, an expected source time with an uncertain location is returned.

3.2 Phase Picking

The list of detected events gives a robust estimation of time windows with seismic signals in the continuous data stream. Further analyses (e.g. event location, magnitude estimation) highly depends on the accurate identification of seismic phases and their time onsets (phase picks). To achieve this in the previously presented data set, an automatic picking algorithm analyses those time windows. Afterwards, the manual repicking verifies the automatically derived results.

Over time, various numerical approaches have been invented with different orders of complexity. Mainly, the reduction of processing time of extensive data-sets is driving the changeover from manual to automated picking procedures. In addition, the manual identification of seismic phases is highly subjective; even the subjective interpretation performed by the same analyst is incoherent over time. Hence, an automatic picking algorithm can provide objective tools generating reproducible and consistent results.

The earliest attempts of automated picking algorithms transferred seismic waveforms into characteristic functions based on the short-term-average to long-term-average ratios (STA/LTA) [139] [140]. This method effectively identifies sharp onsets in seismic traces. To increase the efficiency for lower signal-to-noise ratios and more emergent onsets (e.g., S phases), other characteristic functions (e.g., z-detector, recursive STA/LTA, delayed STA/LTA), higher-order statistics (e.g., skewness, kurtosis) [141] [142] or additional processing steps (e.g., dynamic signal threshold [143]) were introduced. Model-oriented algorithms, such as autoregressive techniques based on the Akaike Information Criterion (AIC) [144] are widely used.

In this category of picking algorithms, autoregression methods present the most sophisticated results [145], but the lengthy implementation of those higher-order approaches (i.e., spectral and statistical differences of P-phases, S-phases, and noise) needs supervision of a seismologist, to identify useful parameters for the picking algorithm. Even high-performance classical picking algorithms cannot outperform the work of an experienced analyst [110]. Most recent developments with neural networks seek fully unsupervised

approaches. But these approaches need enormous training data-sets (i.e., 273,882 earthquakes with each 1.5 million prepicked P- and S- phases [112]), which is not available for this study. Hence, a more classical approach is used in this work.

The output of the previous detector described in Section 3.1 is used here to scrutinize effective time windows with expected seismic phases. For each detected event a time window is limited to 60 seconds before and 120 seconds after the expected event source time. This study is mainly interested in seismic events of local distance, thus desired arrivals are expected not later than 1 minute after the source time. In addition, 60s of waveform data is padded before and after: (1) to prevent artefacts during the application of the taper and the bandpass filter, and (2) the STA/LTA trigger requires a lead time of noise to identify the wave onset. The concept of phase picking on distinct time windows reduces the number of false alarms and increases computation efficiency. To further reduce computation time, a coincidence trigger implemented as a classical STA/LTA trigger with a comparable low trigger threshold is applied on all available seismic traces in the network. This step identifies those stations with phase onsets in the waveforms and before applying the computationally expensive autoregression picker. Besides the robustness of the autoregression picker using the Akaike Information Criterion, significant advantages of this method are the simultaneous analysis of all seismic traces of the three-component data and the contemporaneous picking of P- and S- wave arrivals. A complete mathematical description of the implementation of this approach is given in [145].

It is important to mention, that the autoregression picker, as it is implemented in the ObsPy-package [90], is applied forward and backwards on the seismic traces. Therefore, when triggered falsely, S-picks occur before the P-pick. Physically this is not possible due to the slower wave velocities of S-waves compared to P-waves. Thus, S-picks occurring before the P-pick are neglected in this workflow.

In general, automatically identified picks tend to be delayed (see Section 3.2). Besides sharp noise signals preceding the actual arrivals, the clear identification of refracted head waves (Pn phase) and direct P phases strongly depends on the signal-to-noise ratio at each station. Therefore, throughout the network some stations have such a low noise level, that the low amplitude of the Pn-phase is sufficient to trigger the picking algorithm, while the other stations identify the Pg-phase as the first P-onset. This can lead to discrepancies in S – P travel times of several seconds and thus to erroneous source locations. Unfortunately, none of the previously described picking algorithms is able to distinguish between direct phases and refracted phases. Thus, the correct phase identification then rely strongly on the analyst.

Emergent onsets are major issues, also making it difficult for a trained analyst to identify the true arrival time. Similarly, uncertainties of the S-pick accuracy is greater than for P-picks due to their emergent appearance out of the P-wave coda. One possibility to improve the picking would be to perform the autoregression picker on distinct frequency bands (e.g., half-octave bands) in parallel (compare [146]). This could enhance the picking for events with narrower dominant frequencies, as their signal-to-noise ratio would increase. In addition, this could help to apply the picker for a wider range of epicentral distances, as higher frequencies are damped stronger and dominant frequencies decrease.

But this option is less performant because the repeated application of the costly autoregression algorithm on the same waveform prolongs the overall processing time. So far, this option has not been implemented in the presented workflow.

To ensure high location accuracy of the final seismological catalog, a manual repicking of the results of the automatic picker is crucial. The pyrocko environment [76] provides a highly performant waveform visualization tool called snuffler, which also allows the visualization and creation of new pick markers. Additional optional tools called snufflings can be loaded and facilitate the manual repicking. For example, global seismicity catalogs can be scanned for pre-located events in the analysis period. Then, the cake module (see Section 3.1) can be used to derive theoretical arrival times for those events, to help identify suspicious phases.

In the presented workflow, it is essential to assign a specific category to each pick. Snuffler does not allow extensive parameter lists as presented and used in the QuakeML format (see the introduction to this Chapter). Thus, each pick is assigned to one color-coded integer group:

- automatically generated and preliminary
- manually generated and confirmed
- automatically generated and confirmed
- automatically generated and rejected

This step allows the reconstruction of the processing later on, because this information is stored in the QuakeML container. During the repicking, the polarity of the first arrival can be stored as well. This allows the inversion of focal mechanisms for those events (see chapter 7). All information described in this chapter is stored in the QuakeML catalog and can be accessed directly or after the processing is finished, for further stochastic analyses or traceability of the processing itself.

3.3 Results

The fully automatized event detection (see Section 3.1) resulted in 1919 detected events for the complete recording period of 15 months (447 days). On average, this results in 4.3 events per day. As described in Section 2.2.3, the number of recording stations varied throughout the survey, due to heavy rainfall during the austral summer. The detectability strongly depends on the available number of recording stations, because (1) a high number of stations with small interstation distances lowers the minimal detectable magnitude, (2) a consistent spatiotemporal coverage guarantees higher chances to detect events over a wider area and (3) the delay-and-stack approach of the Lassie-detector needs several stations to operate. This dependency is visualized in Figure 3.3; with decreasing station availability, the detection performance reduces significantly.

During the first five months, 12 to 13 stations were recording continuously, resulting in 10 ± 5 detections per day, slightly decreasing over time. The decreasing detection rate,

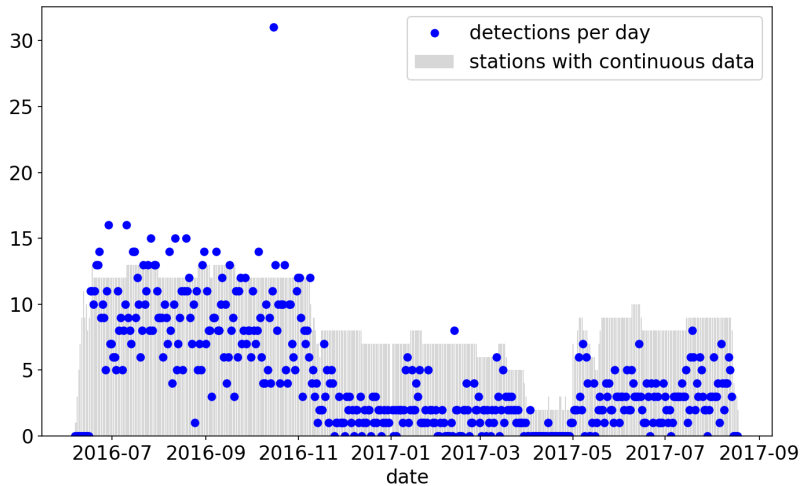


Figure 3.3: Time series of automatic event detections. Blue dots represent daily event detections over time. Grey bars show the number of stations with complete, continuous data recording for that day.

while the network set-up remains unchanged, indicates that the recording period still covered the tail of the aftershock sequence of the El Galpón event, following an Omori-law event rate decay [87]. After three to four stations stopped working in November 2016, the detection rate went down to two events per day on average. When the number of available stations went down to two, only one detection was triggered for 28 days. After restoring most of the stations in May 2017, the average detection rate increased to three detections per day and remained stable until the end of the survey. An exponential decrease (Omori-law) of daily detections is not recognizable for the later period.

It is to be pointed out here that the series of events on October 16, 2016, led to an outstanding daily detection rate. This short term increase of the detection rate is related to the occurrence of an M_W 4.8 earthquake approximately 130 km to the north of the network in the Argentinean province of Jujuy. In the first hours after this event, a high number of aftershocks occurred close in space and time to the mainshock, triggering the automatized detector.

Based on the 1919 detected events more than 27,000 arrival time onsets (13,731 P-picks, 13,724 S-picks) are identified in the automatic picking procedure. For 23 events, no picks – neither automatically nor manually repicked – can be identified. The number of picks listed in table 3.1 shows twice as many S-picks, because of the redundancy on the horizontal components. Averaged over all events, the catalog comprises 7 picks (P and S, thus s-p-times are available) per event. This presents a good basis for locating most of the seismic events.

		P-picks	S-picks
automatic	preliminary	11,122	24,964
	rejected	40	1,980
	confirmed	2,569	503
manual		12,958	24,928
used		15,527	25,431

Table 3.1: List of all picks after the manual reprocessing of 1919 automatically detected and picked events. Preliminary (automatic) pick number consists of unsupervised results, while rejected and confirmed picks are determined automatically, supervised during the repicking. Manual picks are picked by the observer. For further processing, only confirmed and manually derived picks are used.

The manual repicking reveals different pick quality for P and S phases. Five times more automatic P-picks are confirmed than S-picks. Rejected picks are categorized subjectively and thus cannot be discussed statistically.

3.3.1 Pick Uncertainty

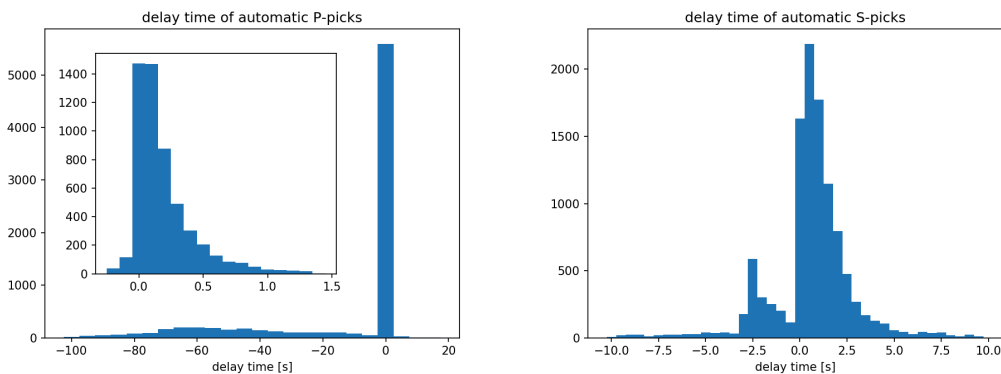


Figure 3.4: Histograms of time residuals between automatic and manually identified picks. Confirmed and rejected classified picks are neglected. Left: P-pick residuals, with 5 s binning in the main plot and 0.1 s binning in the inset. Right: S-pick residuals with 0.5 s binning.

Here, the accuracy of the automatic picking process is examined with respect to the repicked pick catalog. This is under the assumption, that a well-trained analyst works perfectly, and the output is more accurate than results from the presented automatic approach. To quantify the outcome of both steps, the time residuals between the automatically and the manually picked times are calculated and shown in Figure 3.4.

On a broad time scale, most of the automatic picks (5,500 out of 8,000, approximately) fall into a range of ± 2.5 s around the true (manual) pick. The others accumulate around -60 s ± 20 s. This coincides with the onset of the padded noise period before the event. Possibly, the taper applied to both ends of the picking window does not prevent artefacts as intended, so the STA/LTA is triggered when the energy level of this part is stronger than the incoming waves. Having a closer look 2 s around the true pick reveals, that most of the automatically determined P-picks are delayed. The occurrence of delayed picks decreases exponentially until 1.5 s after the manually picked time.

S-pick time residuals fall into a narrower overall range of ± 10 s. Similar to the P-picks, automatic S-picks occur delayed, but with a mode value between 0.5 and 1 s. For later time residuals, the amount of picks also decreases exponentially until 5 s after the manual picked time. A second log-normal distribution appears for earlier automatic onsets with a peak between 3 and 2.5 seconds before the true S-wave onset. This could indicate a systematic misparametrization of the S-wave picker, unable to adequately detect the true onset.

The automatically identified P-picks can be labeled with reasonable uncertainty of 0.5 s, while S-picks reveal 2.5 s of uncertainty. Uncertainty from the manual repicking is set to 0.1 s for P- and 0.5 s S-picks. The overall delay of seismic phase pickers is also resembled in this data set and emphasizes the need for a manual interaction of an analyst to reassure interim results in the processing workflow.

3.3.2 Wadati-Diagram

Originally introduced in 1933 [147], the Wadati diagram presents a straightforward method to determine the origin time of seismic events, based only on the picked arrival times of direct P- and S- waves at several stations [148]. This solely empirical method works under the assumption of a constant v_P/v_S ratio. Thus, it is not limited to homogeneous half-space models and does not require further knowledge of the subsurface elastic parameters. Following the derivation in the appendix A.1.1, when observing P and S arrival times at two stations (a and b, respectively), emitted by the same earthquake, the v_P/v_S ratio can be estimated as A.3:

$$\frac{v_P}{v_S} = \frac{t_S^a - t_S^b}{t_P^a - t_P^b} \quad (3.1)$$

With this empirical approach, it is possible to check the observed arrival times independently and to test whether or not the assumption of a constant v_P/v_S ratio and its absolute value is reasonable for the studied area. For better implementation, the iteration runs over the permutation of all stations, neglecting the backazimuth and epicentral distances. Therefore, the adjusted Wadati diagram is point symmetric to the origin.

As a rule of thumb, the v_P/v_S ratio for crustal raypaths of direct waves can be given as $\sqrt{3}$. Further in this analysis, only confirmed picks (either manually set or confirmed by an analyst) are used. The mode of the symmetrical v_P/v_S distribution shown in Figure 3.5 encompasses this value. The standard deviation of this normal distribution reflects the expected error of ± 0.4 after the repick procedure.

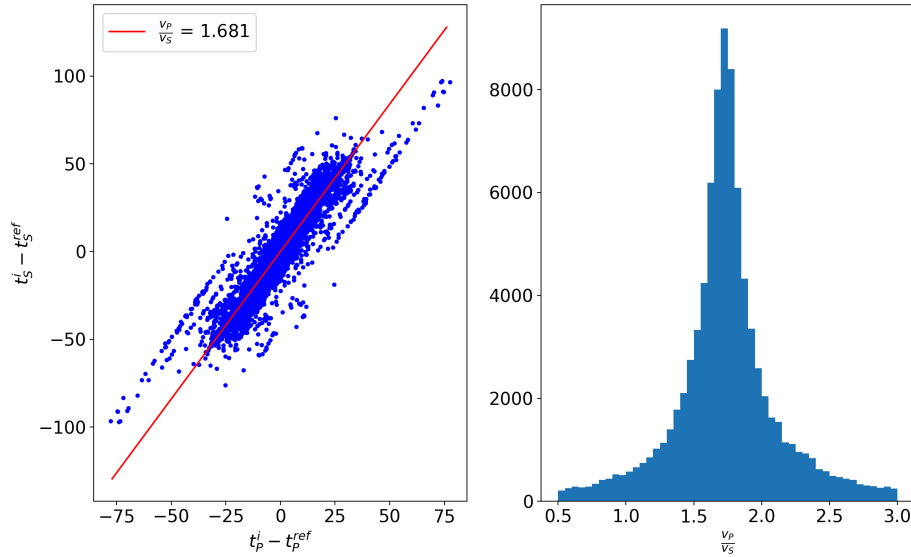


Figure 3.5: Wadati diagram results following equation A.3. Left: adjusted Wadati diagram, estimating the v_P/v_S ratio by regression through all empirical data points. Right: histogram of v_P/v_S ratios calculated for each event and station combination independently, with 0.5 bins.

To focus on the pick accuracy of local seismicity, a subset of the most robust locations (location error < 100 km, hypocentral depth $\neq 0.0$ km as this indicates a fixed depth) is sampled from the final catalog (see Chapter 4). When plotting the arrival time differences of the S-phases over P-arrival differences of all possible station combinations in the network, the slope of the regression line represents an average v_P/v_S ratio over all available raypaths. Unfortunately, linear regression is influenced by outliers. The outliers visible in Figure 3.5 appear due to clock offsets at two permanent stations and are discussed and corrected in the following Section 3.3.3. Thus, the v_P/v_S ratio of 1.68 is smaller than expected and is determined correctly in the next step.

3.3.3 Network Based Time Correction for Single Station Static Clock Offset

The outliers in the Wadati-diagram of Figure 3.5 align well to a straight line, with a similar slope, but no intersection in the origin. This offset in the data is introduced by a temporary, constant clock offset of the INPRES stations SLA and AHML (see Section 2.2.1), which was already recognized during the repicking procedure (see Section 3.2). Here, an innovative approach is presented in order to determine the clock offset of a single station using information from the whole network.

Starting from equation 3.1 and under the assumption all other stations have correct clocks, it is possible to show (full derivation see Appendix A.1.2), that the time offset of one station can be determined by:

$$t_{offset} = \frac{n}{1 - m_{diff}} \quad (3.2)$$

m_{diff} and n are the linear regression components of the adjusted Wadati diagram, where one station shows a constant time shift.

At first, the time periods of constant time shifts have to be identified. When iterating over each station permutation and each event of the event catalog, the adjusted Wadati plot of the picks with time offset does not align with the other pick differences. For every single event – stations combination, the approximated time offset can be determined using linear regression, here, using the Python-based NumPy package [149]. This step only works if sufficient pick combinations are available and the absolute pick differences stretches over a wide range of values, i.e., picks of waves arriving nearly simultaneously, impede the linear regression and lead to high errors. Hence, only events with at least four pick combinations are used. Event – stations combinations with absolute time offsets greater than 15 s are labeled as candidate events.

Afterwards, for each station, consecutive candidate events are grouped, when estimated time offset average around a similar value (± 10 s; remind that uncertainties are still high). The use of a two-step recursion allows single outliers in the list of candidate events. In the end, for each station (if it exists) one or multiple lists of consecutive events with a similar time offset are generated, implicating periods of clock offset at that station.

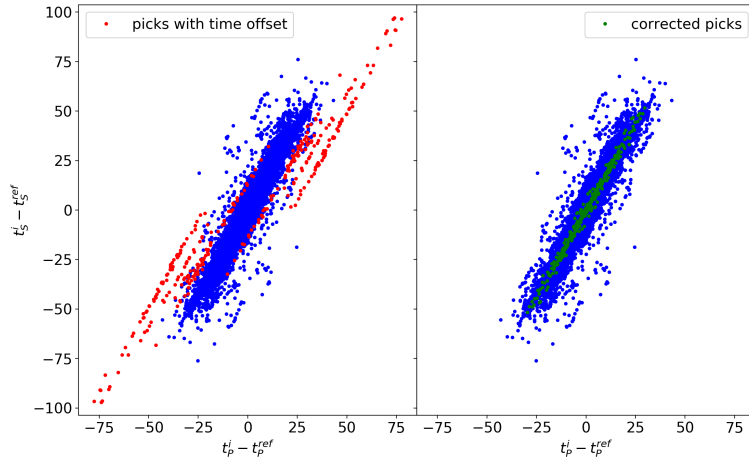


Figure 3.6: Wadati diagrams following equation 3.1 (blue dots). Left: uncorrected picks with clock offset highlighted as red dots from automatic identification. Right: Automatically identified picks with subtracted time offset in green dots.

For each group of candidate events with similar time offsets, the linear regression is executed once more. This second regression benefits from the increased number of used events, as more pick combinations are involved, which also stretches over a wider range of pick differences. Only candidate event groups with standard deviations greater than $\sqrt{0.1}$ are retained further.

To include event picks which were not identified in the first regression step (i.e. because of too few pick differences per event), all event – reference station combinations are rechecked, whether or not their pick-differences align with the identified regression line, under the assumption the time offset applies for that reference station. This step assures thorough identification of the length of clock offset periods and robust regression results.

Station	event	time offset +/- σ
AHML	2017-02-18 12:10:53.496	34.7472 s +/- 0.1449 s
	2017-02-24 16:22:25.372	
	2017-02-25 08:45:37.751	
	2017-03-03 04:42:17.771	
	2017-03-04 07:38:37.456	
AHML	2017-03-08 20:16:54.819	50.3174 s +/- 0.0361 s
	2017-03-08 20:41:14.676	
	2017-03-11 08:16:46.855	
	2017-03-12 04:51:01.048	
	2017-03-12 15:51:29.697	
	2017-03-13 03:30:08.358	
	2017-03-18 05:17:01.160	
	2017-03-19 02:53:34.765	
	2017-03-20 08:17:54.206	
	2017-03-22 00:52:17.631	
	2017-03-23 21:05:59.141	
	2017-03-26 18:42:44.428	
	SLA	
2017-07-17 08:23:30.155		
2017-07-18 08:24:49.026		
2017-07-20 15:39:32.498		
2017-07-30 19:23:27.182		
2017-08-05 03:01:21.149		
2017-08-07 07:34:24.235		

Table 3.2: Groups of the station and event combinations with temporary, constant clock offset.

For the presented event catalog, three periods of constant clock offset at two different stations (AHML and SLA) are identified, spanning from eight days up to one month. Identified events are listed in Table 3.2. Each period match with one line of picks in

the adjusted Wadati diagram in Figure 3.6. After subtracting the time offset from the corresponding picks, they accurately align to each other and intersect the origin.

The presented list in Table 3.2 might not be complete, as the observer rejected some picks during the manual repicking procedure. However, the uncertainties (σ) taken from the regression covariance matrix are below 0.04s, which is a factor of 10 smaller than the pick uncertainties after the manual repick.

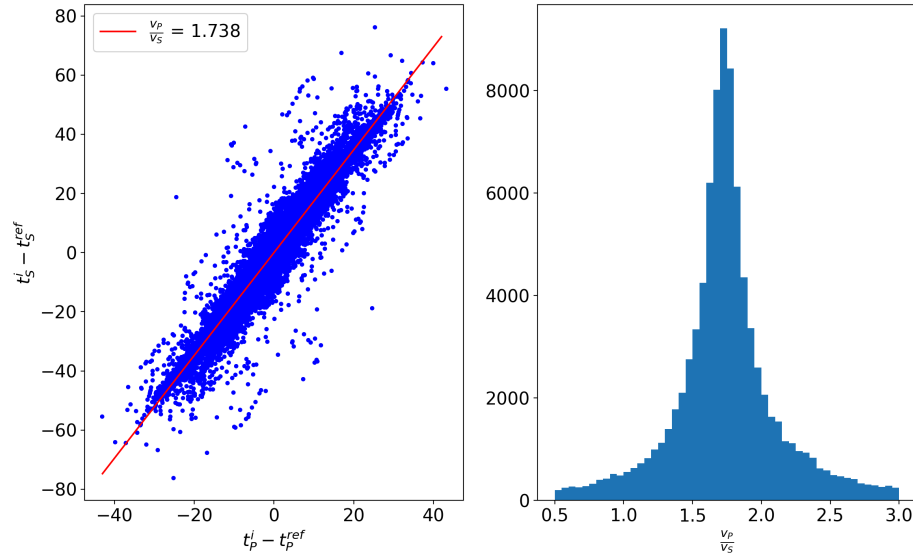


Figure 3.7: Wadati diagram and v_P/v_S distribution after the correction of time offsets. For more explanations see Figure 3.5

When comparing the estimated v_P/v_S ratios before (1.68) and after the time correction, the latter value of 1.73 is in agreement with the anticipated value of $\sqrt{3}$. To conclude, the presented static time correction serves as a robust tool to correct with high precision the clock offset of a station using a seismological network. In further processing steps of the next topics, only those corrected values are used.

4 Topic III: Event Catalog

The aim of seismological study is a deeper understanding of the origin of an earthquake and its associated processes. Two crucial parameters are the location and the magnitude of an earthquake. The former gains importance, the more source locations are available, in order to map seismogenic structures and to understand the processes leading to their occurrence. The processes contribute to the understanding of the extension of seismological processes and are of high public interest for seismic hazard mitigation efforts.

Both parameters can be estimated fully automatically with the data presented and introduced in the previous chapters. Automation does not only reduce computation time. Moreover, it allows a complete objective analysis of the observed data. In addition, it facilitates reproducibility and parameter optimization.

4.1 Event Location

Numerous software packages have been developed over the last decades tackling the task of locating earthquake hypocenters. The wide variety of computer platforms, programming languages and methods have also increased as well as computational power itself. In observatory practice widely used software includes: Earthworm [99], SEISAN [100], and SeisComp3 [101] [102]. For higher flexibility and better integration of the presented workflow, a stand-alone tool is favored over those complex integrative software solutions. Here, the FORTRAN based program HYPOSAT [114] in its newest version 6.0c was used to locate the earthquakes identified in the previous steps.

HYPOSAT can be applied to a wide range of epicentral distances, from local events to teleseismic records. It incorporates the use of arrival times and travel-time differences of direct, reflected and critically refracted phases (e.g., PnP). In general, all seismic phases, following the name convention, as recommended by IASPEI, can be included in the inversion process. Using the tau-spline interpolation, various global spherical Earth models can be incorporated. Primarily the AK135 model [81] is used. For the primary hypocenter estimation, the CRUST 1.0 model [150] (see Figure A.2) was used additionally as a local velocity model for the source region (1.5 degrees around the epicenter), as this model accommodates the local deviation from the global velocity models. Later, in Chapter 5, a new local velocity model is estimated, which is then used to update the primary hypocenters.

Regarding the aim of a maximized level of automation, HYPOSAT integrates well into the presented workflow. I/O python scripts prepare and transfer the input data from the QuakeML database into the free FORTRAN data format automatically, as well as the location output back into the XML-format. The QuakeML data format allows a

wide range of parameter classes, thus the full HYPOSAT output can be stored for later quality assessment (e.g., location uncertainties, used arrivals, arrival residuals, etc.).

The only a priori information included here is a deeper starting depth for the inversion at 25 km, which appears to give more robust locations because hypocentral depth estimations in the study area distribute deeper than global averages [71] (see Section 4.3.2). It is also tested to use the locations given by the Lassie detector as starting locations for the inversion. However, this step leads to higher uncertainties and unstable locations. As described in Section 3.1, for costs of location accuracy, Lassie favored computational efficiency. Thus, those theoretical locations as starting values push the inversion into some local minimum, leading to high residuals and prevent the inspection of the best solution.

4.2 Magnitude Estimation

The original intention of Charles F. Richter to introduce a magnitude scale was to provide an objective measurement of the original energy of an earthquake, regardless of the point of observation [151]. In the following years, Gutenberg & Richter [152] [153] standardized the processing of seismometric recordings and magnitude determination, using the Californian seismic network of Wood-Anderson instruments and invented the local magnitude scale M_L . The magnitude concept was further extended to be applied in medium- and long-period records of either body waves (m_B) or surface waves (M_S). Thereby, the magnitude concept also became applicable for events of regional and teleseismic epicentral distances. In the scope of modern, digital seismometer recordings, various types of earthquake magnitudes were developed and are still in use. The Working Group on Magnitudes of the IASPEI Commission on Seismological Observation and Interpretation recommended standard procedures for calculating the most used magnitude scales (e.g. M_L , M_s , m_b , m_B , and m_b_Lg) [154]. Here, the updated IASPEI local magnitude scale M_L is used and briefly presented.

$$M_L = \log_{10}(A) + 1.11 \cdot \log_{10}(R) + 0.00189 \cdot R - 2.09 \quad (4.1)$$

A – maximum trace amplitude in nm

R – hypocentral distance in km

The local magnitude is determined by two observable and three empirical parameters. Originally, the equation 4.1 is intended to be used only for crustal earthquakes in regions, which have similar seismic wave attenuation as Southern California [155]. So far, a regional calibration function for magnitude estimations does not exist for the central Andean Foreland system [154]. In addition, the use of the same calibration function as INPRES [156] (for their magnitude estimation the Californian calibration function is used) allows a direct comparison of the national earthquake catalog with the final catalog of this work.

The processing step of magnitude estimation is completely automatized in the presented workflow (see Figure 3.1). At first, the waveform picks are utilized to identify stations and traces with sufficient signal-to-noise ratios. As described in Section 2.2.2, the noise level is station-dependent and varies throughout the network. Thus, the catalog contains events with measured amplitudes at one station below the average noise level of another station; these events would have wrong magnitudes assigned, if traces with signals to noise ratios smaller than one were not excluded. Second, picked arrival time differences are used to define time windows where the maximum trace amplitude is expected. As the arrival onset is picked, and the S-wave arrival is expected to contain the most energy, three times the S – P arrival time difference, starting at the P-pick, is set as the time window. If only the P-pick was available for a station, the window length was fixed at 3 minutes after the P-pick. Additional padding was performed for each iteration through the traces by padding 2s of data at both ends of the data window.

When iterating over each station, the vertical components are neglected because the local magnitude, as presented in equation 4.1, is defined for the horizontal components only. Before determining the maximum amplitudes, the seismological traces have to be restituted and transferred to displacement so that they replicate a Wood-Anderson standard seismograph with a static magnification of 1. The instrument responses of the sensors used in the survey are confirmed in Section 2.3 and automatically derived from the StationXML file. To prevent artefacts, a bandpass filter is applied with corner frequencies at 0.05, 0.1, 30.0 and 50.0 Hz. The maximum trace amplitudes are determined for both horizontal components independently of each other, but only the maximum value of both traces is stored in the quakeML-database. In addition, the standard deviation of the trace within the predefined time window is calculated and used as the noise level to specify the signal-to-noise ratio.

The second observable parameter in equation 4.1, the hypocentral distance R is directly calculated from the source location taken from the primary hypocenter estimation in the previous processing step. However, the local magnitude scale is only defined for events with hypocentral distances smaller than 1,000 km. Thus earthquakes at larger distances do not have a magnitude value assigned to them.

The final magnitude value is evaluated as the mean of the magnitudes determined for each station for that event (called station magnitude in the quakeML environment), without additional weights. The quakeML file format allows extensive storage of all determined parameters during the magnitude estimation, i.e., the full list station magnitudes with URI, weights, and residuals. This facilitates event-wise quality assessment, after the data processing is completed.

4.3 Results

The final catalog consists of 1,435 earthquakes with a primary hypocenter estimation and a local magnitude value. 1,199 of those events are without a fixed depth estimation of 0 km. Roughly half of those events are crustal earthquakes within the network extension

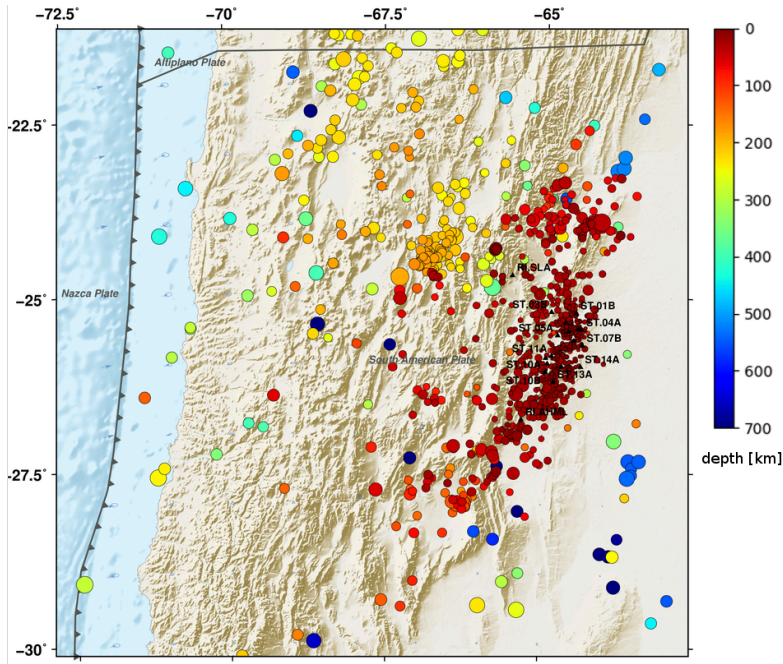


Figure 4.1: Topographic map of the central Andes showing the earthquake primary epicenters as circles, color-coded by depth. Circle size corresponds to magnitude. Seismological stations are visualized as black triangles.

or located in close proximity, as shown in Figure 4.2. The other half of the catalog comprises three classes, which are visualized in Figure 4.1:

1. Shallow, crustal earthquakes, comparable to events within the network, but of a larger magnitude range. Those events stretch across a narrow band along the Andean mountain front.
2. Intermediate, interplate earthquakes northwest of the study area. Hypocentral depths of these events lie at approximately 200 km and are situated in the Wadati-Benioff zone of the subducting Nazca-plate [15] [157].
3. Deep earthquakes with hypocentral depths of approximately 600 km [12]. During the recording period, deep-foci earthquakes occurred Northeast (Bolivian-Argentine border) and Southeast of the network (Argentinean province Santiago del Estero). Further this category contains the strongest, non-teleseismic event recorded with the installed instruments on February 21, 2017 ($ML_{STRATEGY}7.3$, $M_W6.5$ [1]).

Further, the hypocentral depth distribution with uncertainties is discussed in detail in Section 4.3.2.

4.3.1 Seismicity

During the 15 months of the networks operation time, the occurrence rate of earthquakes is similar, but less than the detection rate of the Lassie detector (see fig. 3.3). Due to weather conditions during the monsoon season, recordings at several stations are interrupted temporarily. For the recording time after October 2016, events with origins of teleseismic and regional epicentral distances are neglected in the repicking procedure (see Section 3.2) to save time during the manual data processing and focus solely on events of elevated interest for the local seismotectonic analysis. The main indicators to identify the events used by the observer are S-P travel times and dominant frequencies. Therefore the final catalog only contains $3/4$ of the initially detected events.

Hence, only the period until November 1, 2016, provides robust results useful for a seismicity rate analysis. As at least 12 stations were recording continuously, the data-set itself can be assumed to be consistent through the first 150 days. On average, 3.08 events per day are identified and fully processed. The events occurred in a rectangular manually chosen region close to the network (corner coordinates: -65.5° lon, -64° lon, -26.8° lat, -24.4° lat). This seismicity rate for local crustal earthquakes is notably higher than presented in previous studies North of this study area [15]. In other seismically active regions worldwide studies have been undertaken with similar network set-ups. Surprisingly, the seismicity rate observed here is more comparable to active plate boundaries as the Southern Alpine Fault zone [158] or the Himalayas [159], than continental intraplate environments as western Anatolia [160]. Nevertheless, it has to be taken into account that the presented seismicity rate does not reflect the actual background seismicity. Less than one year after the 2015 El Galpón earthquake, it is very likely that the catalog contains events from the decaying aftershock sequence [161] [87]. This would lead to biases of the stochastic parameters of earthquake catalogs, which assumes independent earthquakes occurrence follows the distribution of a stationary Poisson process [162].

4.3.2 Spatial Hypocenter Distribution

Instead of a fully descriptive analysis of the complete event catalog, this study aims to improve the perception of seismotectonic processes in the studied region. The spatial distribution of earthquake hypocenters is key for linking the seismological observation with underlying geological processes in the Earths crust.

Unsurprisingly, numerous earthquakes were located in the vicinity of the 2015 El Galpón epicenter, indicating the survey still captured aftershocks of the main event. Nevertheless, events comparable in magnitude and depth occur within the extension of the seismological network, which outline distinct elongated zones of increased seismicity, striking northeast – southwest. The seismogenic zone is quite extensive vertically, spanning from the surface down to at least 30 km within the network, for which low hypocentral location uncertainties can be assumed (quantitatively discussed later). North of the network, earthquakes shallower than 25 km appear to be absent during the recording time, except for a handful of events in the Lerma Valley to the northwest. The same is observed for the Eastern Cordillera to the west of the installed network. To the south

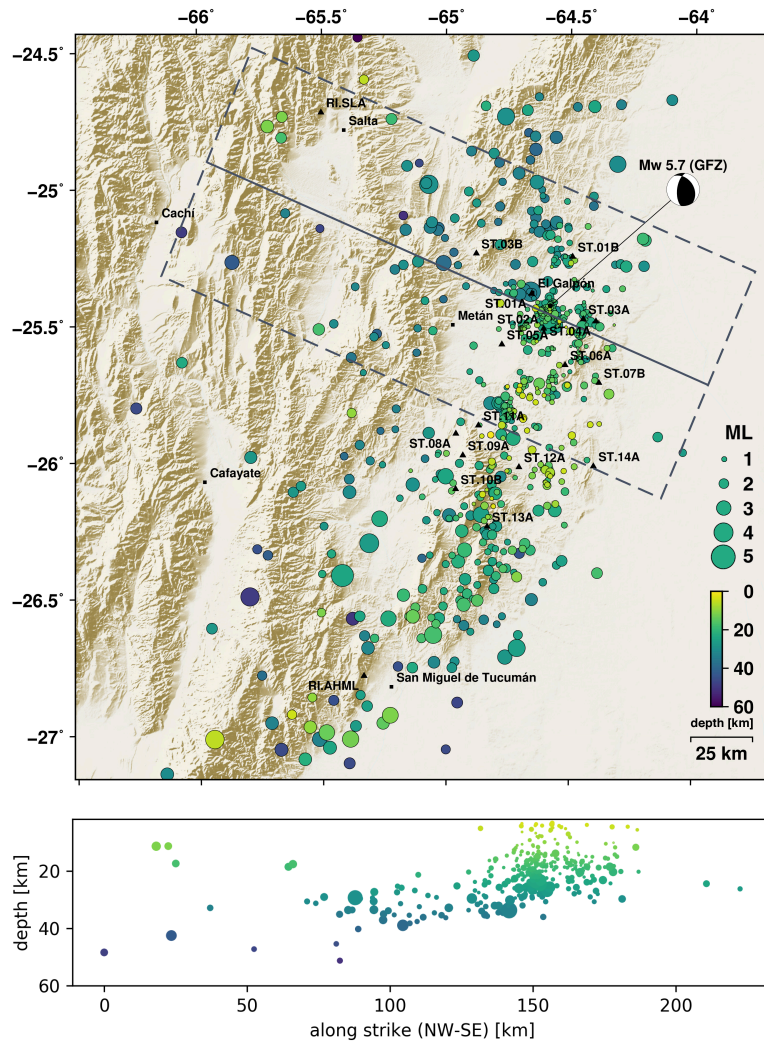


Figure 4.2: *Upper panel:* Topographic map of the study area, showing primary epicenters of local, crustal earthquakes as circles and color-coded by depth. Circle size corresponds to magnitude. Seismological stations visualized as black triangles. The location and focal mechanism of the 2015 El Galpón event given by GEOFON¹ plotted on top. The depth scale is different from Figure 4.1 and limited to crustal levels. *Lower panel:* Profile through the study area, indicated by a grey line in the map. Only events 50 km to both sides of the profile are projected on the plane.

of the network, depth and magnitude distributions are comparable to events within the networks. However, very shallow events are missing, which could be attributed to an increased depth error due to missing seismic stations above the events. Without surprise,

east of the network, no events could be identified (apart from two exceptions), as no strain is expected to be accumulated in that part of the Andean Foreland.

To better visualize the hypocenter distribution in-depth, a profile is created, as shown in the lower panel of Figure 4.2. Here, only events 50 km to both sides of the profile are taken into account to be projected on the profile plane. The orientation of the profile is chosen to be perpendicular to the Metán basin central thrust fault (MBCTF), as inferred by Iaffa et al.[38]. This structure is of major interest for several reasons:

- The fault, as mapped from seismic reflexion profiles [38], lies in the interior of the network and enables a microseismicity analysis with high accuracy.
- The strike of the fault aligns well with the strike of one of the nodal planes and the location of the 2015 El Galpón earthquake, identified from teleseismic moment tensor inversion. Thus, the MBCTF is a candidate structure for this event. It is important to mention the opposing dip of the mapped fault and the nodal plane.
- The length of the MBCTF has a high hazard significance, as it is the only mapped and apparently active structure of that size, to be a candidate for the M7.3 Esteco earthquake.

The uppermost deformation (< 20 km) in this profile is concentrated around the 2015 El Galpón epicenter and to some degree aligns horizontally along the MBCTF. Under the assumption that most of the hypocenters at 150 km along-strike of the profile are aftershocks, these events support the outline of a west-dipping structure as the focal mechanism indicates. This does not support the idea of an east-dipping MBCTF, as suggested by Iaffa et al. [38]. Northeast of station ST.11A and south of the assumed aftershock cluster, a different cluster of events align in a very similar fashion. This observation strengthens the spatial extension of the MBCTF to the south, although the interior part appears aseismic.

East of the previously described NNE – SSW striking structure, multiple earthquake hypocenters align strike-parallel underneath the *Cerro Colorado* range. This event cluster outlines a second seismically active, west-dipping structure. The *Cerro Colorado* fault was already hypothesized by Mon et al [59] [45] from geological mapping.

In the profile shown in Figure 4.2, the upper part (< 25 km) of the crust underneath the Eastern Cordillera (70 – 130 km along strike) appears to be completely aseismic. Further discussions are needed to identify explanations for the limitations of deformation into the lower parts of the crust. These deep seated hypocenters align subhorizontally between 30 km and the Moho, exceptionally deeper than observed before [15] and estimated through balanced cross sections (see discussion in Section 8.2).

To exclude systematic modeling bias as an explanation and assure the depth estimate of the deeper crustal events is true, a strong local event from November 11, 2017 (teleseismic magnitudes ranges: mb 4.3 – 4.9) is used to verify the depths independently. Using regional and teleseismic arrival time picks from global and local catalogs (published by the ISC [1]), alongside recordings of the station ST.03B which was still operating during that event, the event could be relocated using the presented location process scheme (see

Section 4.1). The station of the STRATEGy network is of high importance regarding the hypocentral depth estimation. The epicentral distance is only 9 km (located in the NW end of the Metán basin), while the source depth is estimated to be 31 km including the ST.03B station into the location procedure. This value falls into the average depth range observed here, but represents the lowermost expected values for Foreland deformation on a global scale [71].

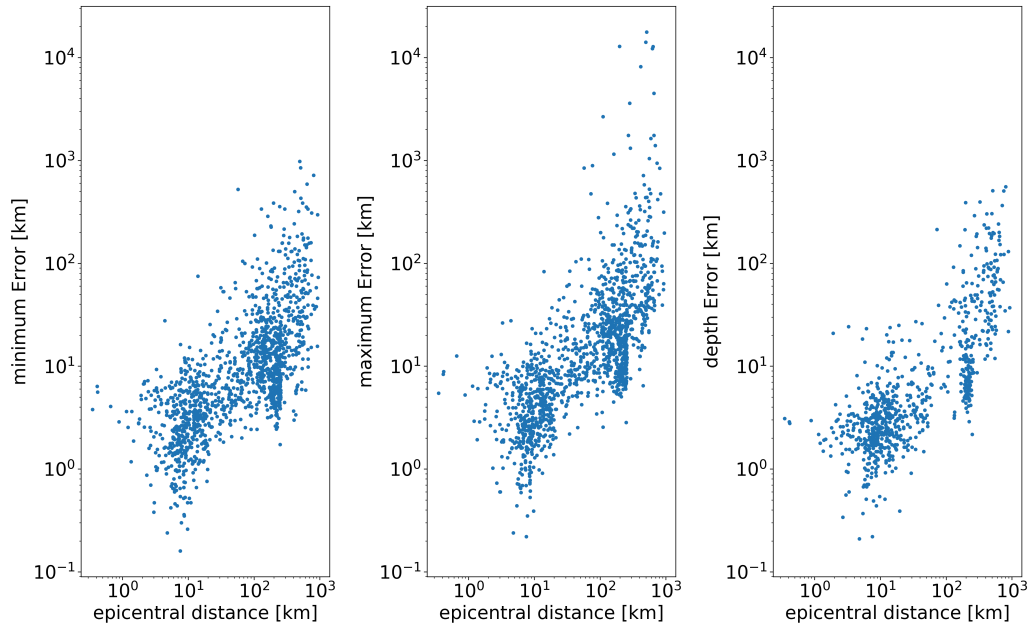


Figure 4.3: Location uncertainty parameters over the epicentral distance for each event. *Left*: minimum horizontal uncertainty taken from the minor axis of the location error ellipse. *Middle*: maximum horizontal uncertainty taken from the major axis of the location error ellipse. *Right*: absolute depth uncertainty given by the HYPOSAT output (see Section 4.1)

Uncertainty estimates (RMS-errors) derived from the inversion of the source locations given by HYPOSAT (see Section 4.1) follow a lognormal distribution. The median is estimated to be 0.64, while the mean of the skewed distribution is 0.92 (see Figure A.9 in the appendix).

In absolute terms, the origin uncertainty for the events is highly dependent on the hypocentral location of the earthquake. In Figure 4.3, the horizontal location uncertainties, as given by the major and minor axis of the error ellipses, and the depth uncertainty are shown as a function of the distance to the closest station of the seismological network. Local earthquakes within a short distance (~ 30 km) have epicenter accuracy less than 10 km, down to 400 m. With greater epicentral distances, the location accuracy decreases regardless of the uncertainty parameter. Similarly the uncertainty increases, the

deeper the source is located. Although in many cases, the hypocentral distance increases substantially, this effect is evident for local, crustal earthquakes (compare Figures A.10 and A.11 in the appendix). To summarize, the primary hypocenter locations presented in the catalog have uncertainties less than 10 km for local events, but in many cases, only a few kilometers. Deeper and more distant events show increased uncertainties up to 200 km, while the best locations in this category can be determined precisely with 4 km uncertainty. A strong azimuthal dependence of location errors or eccentricity values cannot be recognized.

4.3.3 Magnitude Analysis

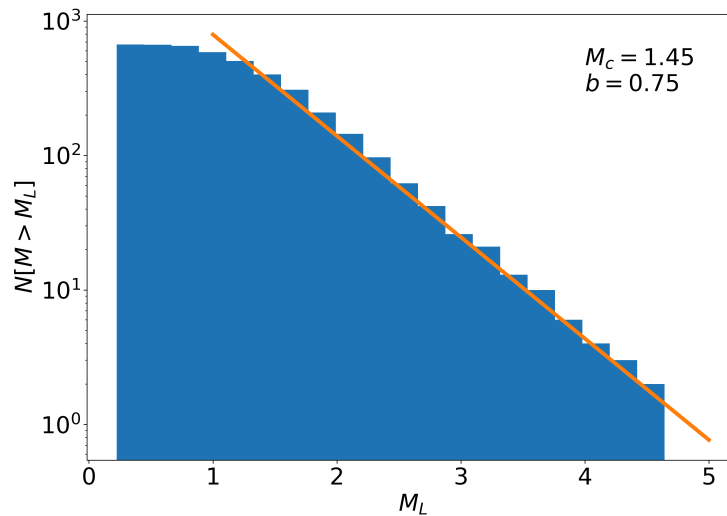


Figure 4.4: Magnitude-frequency distribution of local earthquakes with blue bars for cumulative histogram representation; analyzed region boundaries similar to Figure 4.2. Orange line represents the least square fit (to equation 4.2) for local magnitudes above magnitude of completeness ($M_C = 1.45$).

In order to present a consistent magnitude analysis, only crustal and local events are further considered here. Various seismic sources presented previously (e.g. intermediate-depth interplate events, very deep earthquakes) are generated by different physical processes, leading to uncorrelated event occurrence probabilities.

By analyzing the magnitude-frequency distribution of the earthquakes in the catalog, it is possible to extract parameters to estimate the chances that events of discrete magnitudes occur. For example, the magnitude of completeness (M_C) specifies the magnitude value above which the magnitude-frequency distribution of the catalog follows a power law scale:

$$\log_{10} N(M) = a - b \cdot M \quad (4.2)$$

The M_C can be estimated visually from the plot in Figure 4.4 or by various objective methods. Here, the M_C by b-value Stability (MBS) method was used as presented by Woessner & Wiemer 2005 [163]. With this approach a M_C of 1.45 was estimated for a geographically limited sub-catalog (corner coordinates: -65.5° lon, -64° lon, -26.8° lat, -24.4° lat). This leads to a b-value of 0.75, a rather low value indicating that higher magnitude earthquakes are more likely. Various studies using field and laboratory observations show decreasing b-values with increasing source depth, due to higher lithospheric stresses and fewer heterogeneities at greater depths [164] [165]. Thus, the low b-value confirms the consistency of observing comparably deep hypocentral depths for the investigated local seismicity (see Section 4.3.2).

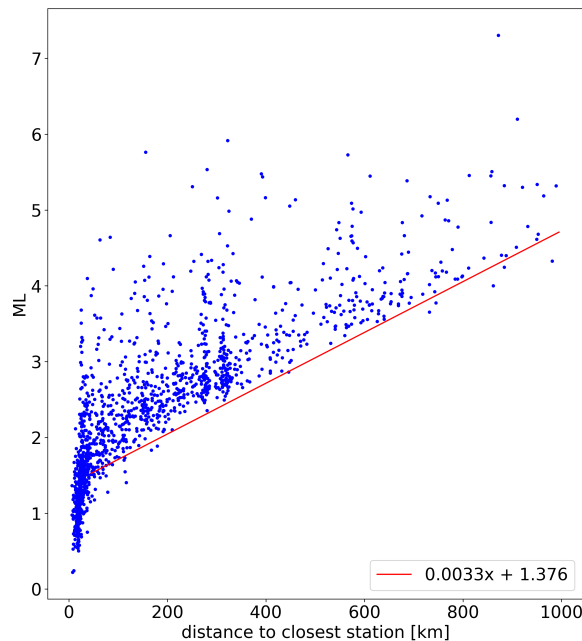


Figure 4.5: Plot of event magnitudes (M_L) over the hypocentral distance to the closest station (blue dots). The red line indicates a linear fit to the 95th – percentile for each magnitude bin (bin width = 0.2).

The detection limits of earthquakes depend highly on the damping along the raypath between earthquake source and the station as a receiver. Comparable to the M_C , the smallest detectable magnitude depends highly on the hypocentral distance. For events within or close to the network (hypocentral distance < 45 km), the smallest detectable magnitude increases rapidly with greater hypocentral distances. It is important to mention that the ability to detect and locate an event does not only depend on the distance to the closest station but rather on the distance to the three closest stations; during the processing, observations of arrival times at three stations minimum are necessary to locate an event unambiguously. For hypocentral distances greater than 45 km, it is more

likely to observe arrivals at numerous stations, as interstation distances are, on average, 17.5 km and at a maximum 38 km. Above 45 km, the minimal detectable magnitude increases linearly with greater hypocentral distance (see Figure 4.5). To estimate the rate at which the detection threshold increases, the 95th – percentile for each magnitude bin (binning = 0.2) is calculated. Then, a linear regression is fitted through all magnitude percentiles above the M_C over their respective distances.

$$ML_{limit} = 0.0033\Delta_{hypo} + 1.376 \quad (4.3)$$

The regression result of equation 4.3 can be translated to an increase of the detection limit by one magnitude with every 303 km.

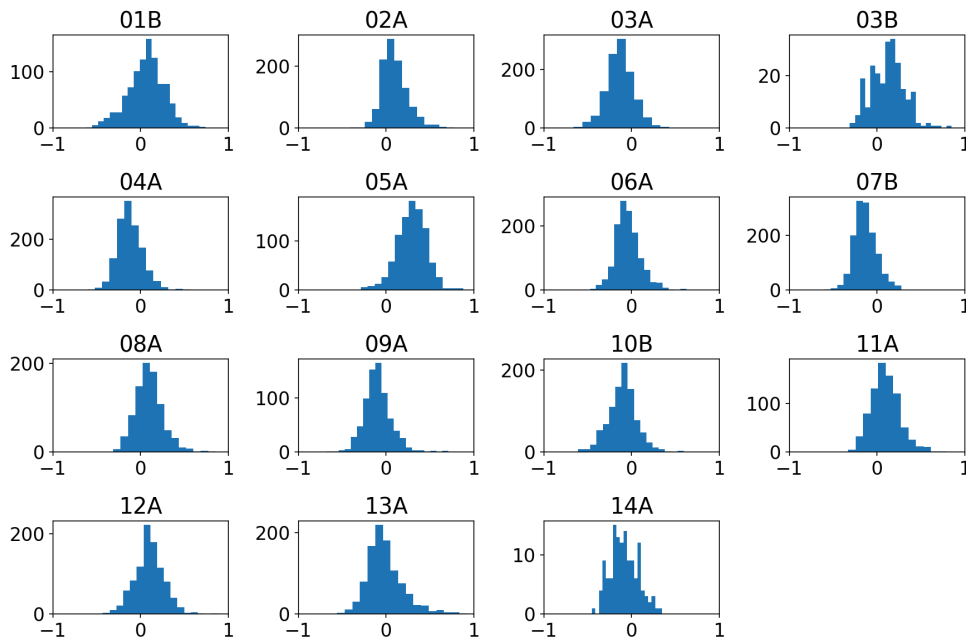


Figure 4.6: Histograms of the residuals between station magnitude and final ML, for all stations in the STRATEGY network.

The residuals between the station magnitude (for explanation see Section 4.2) and the final local magnitude ML follow a normal distribution for each station. The mean values of the residuals correlate with site conditions at each station, while the variance is very similar. For stations in the basin on a sedimentary subsurface, station magnitudes are shifted to higher values (see station ST.05A in Figure 4.6). Thus, the petrophysical parameters of the basin amplify the seismic waves traveling through this kind of media. In contrast, stations that are installed close to bedrock show smaller station magnitudes, than the signal strength averaged over the whole network (e.g., station ST.03A).

5 Topic IV: Minimum 1D – Velocity Model

As described above, the accuracy of hypocenter estimations depends on multiple errors going into the location procedure. The picking accuracy is well determined stochastically and limited by the methods used in the process chain. Site effects, as described in the station magnitude amplification (see Figure 4.6), can lead to systematic bias of distinct event locations. Similarly, inadequate velocity models can lead to systematic errors. Although not deeply discussed yet, global velocity models, as used for primary hypocenter estimation, may introduce the highest residuals and thus dominate the location uncertainties.

Besides the reduction of location errors and presenting a more defined seismicity catalog for further seismotectonic interpretation, the estimation of a local velocity model can provide insights into the crustal structure and the petrophysical parameters of its layers. To do so, a minimum 1D – model is estimated in this chapter using the *FORTRAN* – based VELEST Program [166]. In addition, several tests are presented to resolve the stability and accuracy of the final, local velocity model.

The inversion performed in VELEST solves the coupled hypocenter - model problem [167] [168]. Then, the solution consists of earthquake hypocenter solutions, the velocity model (one dimensional) and station corrections. The inversion minimizes the travel-times residuals using the root-mean-square-misfit. A detailed description of the inversion process is found in Kissling, 1988 [167].

Unfortunately, the inversion for local earthquake data is mostly an ill-posed problem with multiple possible solutions. Without strong a priori information, a wide solution space needs to be scanned by trial-and-error. Further, VELEST does not invert the velocity model for its layering; a number of layers and their thicknesses have to be determined through manual trial-and-error.

5.1 Mantle Velocity Estimation

The use of a priori information can increase the robustness of the inversion process. Especially the uppermost and lowermost layers have disadvantageous raypaths orientation, either subvertical or subhorizontal without crossing pathways. In addition, the lack of raypaths penetrating the mantle (see Section 5.2) complicates the search for stable solutions in these depths. To overcome this issue, here I try to estimate mantle velocities from travel-times differences of critically reflected P-waves.

Under the assumption of a homogeneous, horizontally layered medium, the travel-time difference of a critically reflected wavefield (P_n-phases) only depends on the interstation distance of two stations with the same backazimuth and epicentral distances longer than

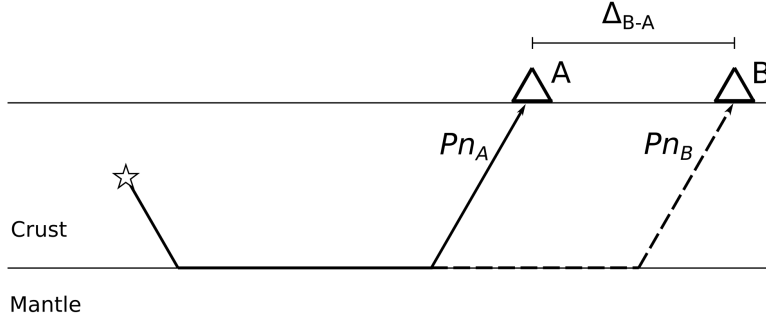


Figure 5.1: This twodimensional sketch illustrates the raypaths of two critically refracted waves (Pn-phase) from the hypocenter (star) to two stations A and B (triangles). The interstation distance between A and B (Δ_{B-A}) equals the dashed part of the raypath Pn_B in the Crust-Mantle boundary.

the overtake distance. Then, the distance between station A and B equals the length of the part of the ray Pn_B , for which it is traveling further through the Moho-discontinuity than ray Pn_A (compare sketch in Figure 5.1). In other words, the difference of the raypath to station B and the raypath to station A is only determined by the mantle velocity and the distance for which the raypath to station B is traveling longer through the Moho-discontinuity.

For this approach, only a particular subset of events can be used. The subset is limited to crustal events, as can emit seismic waves, which can be critically refracted into the Moho. Under the Puna Plateau, the Moho depth can reach down to 60 km (see Figure A.2), but the sparse resolution of the Crust 1.0 model restricts the exact separation into crustal and mantle hypocenters. Thus, a general depth limit of 60 km is used. With the help of the pyrocko cake module [76], the maximum takeover distance is estimated for the region at 150 km. Taking into account maximal horizontal errors of 30 km, used as an additional limitation, the catalog subset only takes into account events with at least 180 km and no more than 1500 km epicentral distance. Events with fixed depth are discarded.

$$v_{mantle} = \frac{\Delta_B - \Delta_A}{t_B - t_A} \approx \frac{\Delta_{B-A}}{t_B - t_A} \quad (5.1)$$

Equation 5.1 is only valid for station pairs with interstation distance paths which are on the same great circle as the event station raypath. Here, the mantle velocity is only estimated if the orientation of both paths differ less than 10° . This would lead to an overestimation of max. 2%. For each event and station pair combination, the backazimuths are also calculated and compared. No azimuthal dependency of the mantle velocity could be identified for backazimuth differences of up to 10° .

The resulting mantle velocities distribute normally over a widespread range (see Figure 5.2); strong, one-sided outliers cause an elevated standard deviation of 5.84 km/s. As

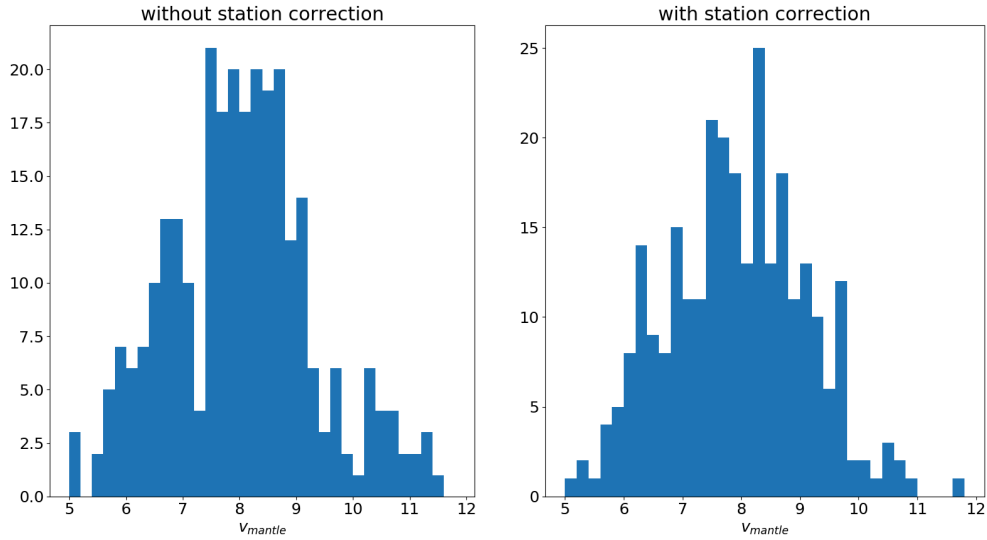


Figure 5.2: Distribution of estimated mantle velocities. *Left*: Only raw arrival times are used, resulting in a median value of 8.08 km/s. *Right*: arrival times are corrected for station corrections derived from VELEST, results in a lower median value of 7.77 km/s.

discussed above, the local site conditions can amplify seismic amplitudes. Further, phase arrival times can be delayed due to local lithological variations. The minimum 1D-model inversion performed by VELEST (presented later in Section 5.4) also estimates station corrections for each station of the network. When incorporating these site-specific values and correcting the arrival times, the mantle velocity values are less widely distributed (standard deviation: 2.72). When including the station correction, the assumption of homogeneous parameters along the raypaths to both stations (Pn_A and Pn_B) becomes more valid.

The backazimuth values cluster around 0° and -150° . In the study area, the Moho is dipping to the west (see Figure A.2 in appendix). Thus, the raypaths of events located in the north of the network should not be affected. The effect of the dipping Moho should be negligible for events from the southwest. In the end, no clear correlation is observable between the estimated mantle velocity and the backazimuth; correlation with other geographical parameters (e.g., epicentral distance, source depth) can also not be identified.

The uncertainty of the mantle velocity estimation can be estimated independently of the data, with respect to the propagation of errors. The pick uncertainty for P-phases is given in Section 3.3.1 as 0.1 s, while the location of the seismic stations derived from averaging the GPS locations of the digitizer gives a precision of 5 m. Thus, the mantle velocity uncertainty is 0.24 km/s. Therefore, the observed velocity difference between corrected and uncorrected arrival time is within these uncertainty bounds. However,

the standard deviation of mantle velocities derived from corrected arrival times is ten times higher than the expected uncertainty range. This increased error range reflects the inappropriate assumption of a homogeneously layered crust. First, crustal and non-site specific heterogeneities are not covered in the station correction values and thus, can lead to erroneous arrival times. Second, thick low-velocity zones at one station do not simply increase the arrival times. Further, the raypaths change their geometry in a way, so the assumption that the additional distance traveled through the Crust-Mantle boundary equals the interstation distance is no longer valid.

The final mantle velocity of 7.8 km/s is within the range of expected values for a continental environment, compared to global velocity models [150] [81] (compare model in Figure A.2) or large scale tomography studies [169]. This ensures the use of a narrower mantle velocity range throughout the inversion process as a priori knowledge.

5.2 Data Selection

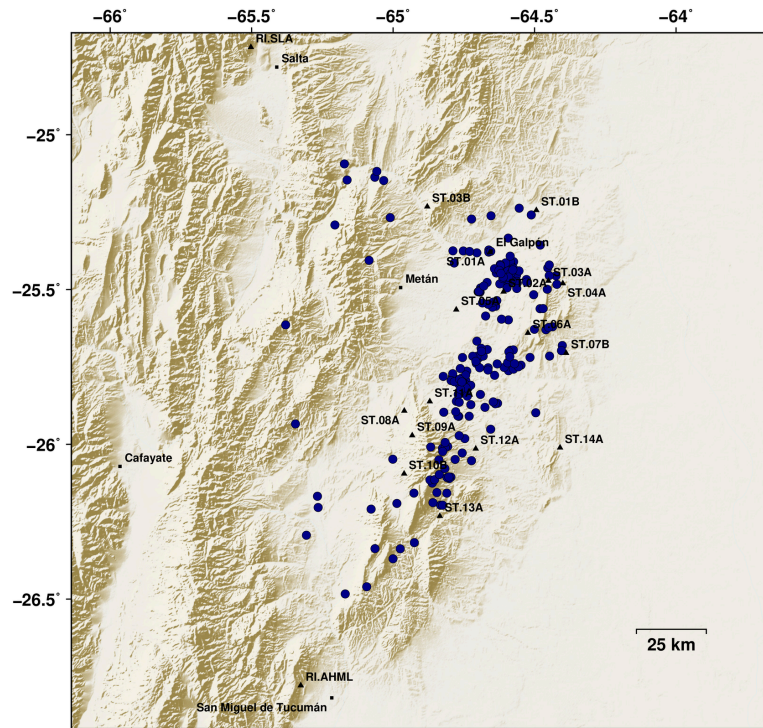


Figure 5.3: Map showing the location of earthquakes used for the inversion with VE-LEST. Black triangles indicate the location of seismic stations used during the inversion.

To approach a stable 1D-minimum model only a subset of well-located earthquakes is used. But first, a limitation of the geographical extent of epicenter locations is applied.

This step assures consistency of the lithological and structural settings, when the used catalog is limited to one tectono-stratigraphical province. Events used here are within the geographical bounds: (-65.5° lon, -64° lon, -26.5° lat, -25° lat).

The terminology of "well-located events" as used in the VELEST manual [166] is defined by the amount of data and their respective geometrical distribution used in the location procedure (see Section 4.1). The catalog subset is limited to events with confirmed picks at more than six stations (see Section 3.2) and an azimuthal gap smaller than 180° . The purpose of the former is to reduce the absolute location uncertainty, while the latter parameter ensures equally shaped uncertainties in all spatial directions, especially for depth estimation in case no station is near the epicenter.

Overall, the original catalog of 1,436 earthquakes is reduced to 580 events (shown in Figure 5.3), which are located in the geographical area of interest. Out of those, only 215 events are left in the subcatalog and used for the inversion of the minimum 1D-model.

5.3 Approaching Stable Solutions

To determine a minimum 1D-model using VELEST is not a straightforward task. Several inversion parameters have to be explored in order to scan the solution space properly and find stable solutions for the given data set. In this Section, different model and inversion parameters are tested. First, proper initial model parameters are scrutinized (section 5.3.1). Afterwards, several tests are executed to identify probable parameter interdependence and to assess the stability of the final results. The process of resolving appropriate model set-ups is performed with P-wave picks only, due to their lower uncertainty of picking times. Later, for the final models, S-picks will be included as well to estimate v_P , v_S and v_P/v_S .

5.3.1 Model Layering

VELEST inverts for layer velocities, but not for layer thicknesses and the number of layers. Thus, the first step is to identify a proper model set-up throughout a manual trial-and-error approach. In order to find a first velocity layer set up, it is advised [166] to use an initial trial model with 2 km layer thicknesses for shallow crustal depths. Here, the limit of shallow levels is defined at 10 km. Deeper layers are introduced with 5 km thickness, while various numbers of layers are tested to identify the depth of the Moho. For each layer, the velocity is chosen randomly from a uniform distribution with individual upper and lower limits regarding physically reasonable bounds, i.e., at mid-crustal depth it is not expected that average P-velocities would be as low as 5 km/s (see Figure A.2). The exact assignment of velocity ranges to sample from for each layer is given in Table 5.1.

The first model runs were performed 1,000 times, in order to sample properly through a wide solution space of possible minimum velocity models. Stable solutions are defined in the manual trial-and-error process as models with RMS-errors below a certain threshold (i.e., 0.6 s for the continuous 1 km layered model) and final velocity values, which are resolved from various initial starting values. From the left plot of Figure 5.4, it is

depth	lower v_P	upper v_P
-3 km	2.0	5.0
0 km	2.0	5.0
2 km	3.0	6.0
4 km	3.0	6.0
5 km	4.0	6.0
6 km	4.0	7.0
8 km	5.0	7.0
10 km	5.0	7.0
15 km	5.0	7.0
20 km	5.0	7.0
30 km	5.5	7.5
35 km	5.5	7.5
40 km	6.0	8.0
45 km	6.5	8.5
50 km	7.5	8.5

Table 5.1: Initial set-up for approaching a first minimum velocity model as advised in the manual [166]. Lower and upper velocity show the range of the uniform distribution from which initial velocity values are sampled.

important to notice that the model with the lowest RMS value does not superimpose with the most stable solutions. In other words, the minimum RMS-solution does not trace the mode values of the velocity distributions shown in the right plot of Figure 5.4.

With the previously described layer set-up, the resulting models can be analyzed for three different depth categories. The shallowest part, from the free surface to 6 km, shows a wide range of velocity solutions. Seemingly, this depth category is unconstrained and mainly dependent on the initial velocity value as the resulting velocities follow the same uniform distribution as the one from which the initial values were sampled. Mid-crustal layers between 6 and 30 km show confined deviation of inverted velocities. For this depth range, stable solutions are anticipated, as most of the primary hypocenter solutions are located in this zone, increasing the raypath coverage and, therefore, the robustness of the inversion process. The deepest part of the model is characterized by a consistent increase of the P-wave velocity with each layer in downwards direction.

Before reducing the total number of velocity layers by merging layers with similar velocities, a different initial model is constructed solely from 1 km thick layers for the full extent of the crust. This allows the differentiation of rather gradual increases of velocities in certain depth ranges from sharp velocity contrasts. The total number of layers is also varied randomly between 30 and 60 km, to test for preferred Moho depths. The velocity for each layer is chosen randomly from a uniform distribution ranging from 2.5 to 7.5 km/s. The mantle velocity was set manually to 8.5 km/s, to force the inversion to approach a stable solution from a higher value.

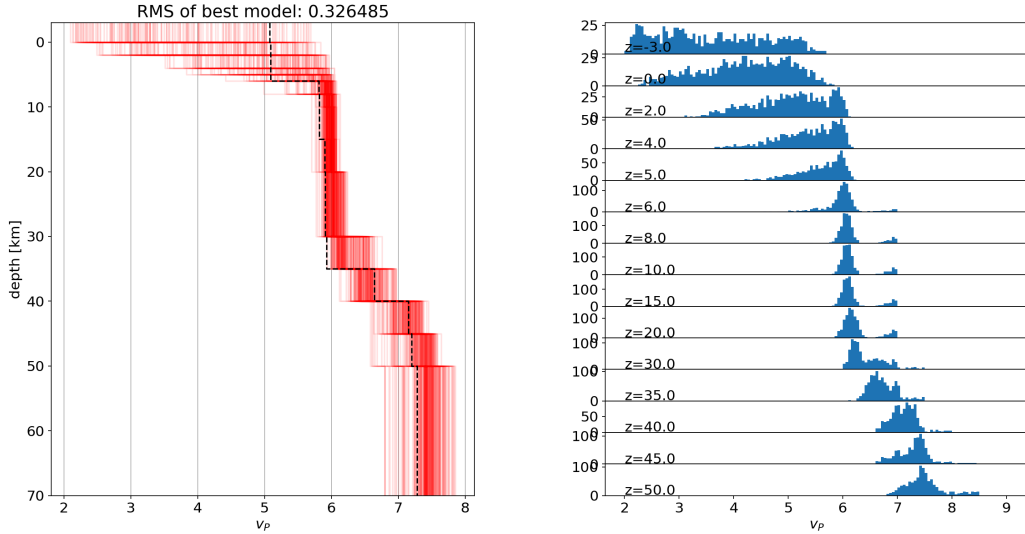


Figure 5.4: Results of first set-up to derive first stable and minimum models. 1,000 inversion runs, but only results with RMS-error greater than 0.6 s plotted here. *Left:* Each red line represents one model result; alpha of lines is 0.1, thus brighter colors represent more models falling in the same or close solution space. The dashed line gives the result of the model with the smallest RMS-error. *Right:* For each layer (as given in Table 5.1), the histogram of the resulting velocity values is shown.

The outcome from 1 km vertical layering (see Figure A.3, left model) results in models with distinct parts of 4 depth categories. The shallowest and second shallowest parts down to 30 km are very comparable to the result presented in Figure 5.4. The slightly higher average velocity could be an artefact of the unconstrained shallowest part, when too high initial values (randomly sampled) shift resulting velocities in the layer underneath to higher values, as here low-velocity layers are not allowed to compensate for that effect. From 30 km depth to the mantle, the velocities increase gradually. The determination of a stable solution for the Moho depth and the mantle velocity is of high uncertainty, due to limited raypath coverage for these depths with only two events in the reduced catalog having a hypocentral depth below 41 km; the depth to the Moho given by the CRUST1.0 [150] global velocity model for the study region. With both previously described generators of initial velocity models, no clear, stable solution range is identified, despite the tendency of more models resulting in lower RMS-errors for Moho depths above 50 km. In addition, the resulting mantle velocities are below global averages and the estimated values in Section 5.1. To overcome that problem, a priori information from receiver functions (Morales et al., *personal communication*) and large

scale tomographies [150] [170] are used to damp the mantle velocity and thus keep the model in more reasonable physical bounds. This step helped to reduce the deviation of the mantle velocity from its initial value of 8.3 km/s.

The final models of the inversion with damped mantle velocities result in slightly lower average RMS-errors in comparison to the undamped case (compare Figure A.3). Still, the lowermost part of the models (>40 km) is unconstrained and does not affect the velocities in shallower parts. However, the installation of the Moho as a firm contrast lowers the RMS-errors; due to the reduced number of hypocenters in this depth range, the damping lowers the uncertainty of the under-determined system. This effect can also apply to the gradual velocity increase within the lower crust and a possible contrast cannot be resolved due to a lack of data.

A simpler model with a smaller number of layers, which gives at least similar RMS-errors and stable results from different initial velocities, is preferred over a complex model. Thus, layers with the same velocities in the previously discussed models are merged into one layer, i.e., mid-crustal layers between 6 and 30 km. With the reduction of parameters in the inversion, the average and minimal RMS-errors are reduced drastically, on average 0.31 s. The simplification of the shallowest layers do not influence the overall model quality. Therefore, the sediment layer is separated into a low velocity-layer representing the top lithology of the basin and a layer of compacted sediments resembling the basin geometry. With fewer shallow layers, mid-crustal (6 – 30 km) velocity solutions fell into a narrow range of 5.8 ± 0.2 km/s. The transition between upper and lower crust can be modeled equally by a sharp transition at 33 km or a gradual velocity increase throughout the whole lower crust, represented by 1 km thick layers (see Figure A.4). Both layer set-ups result in equivalent distributions of RMS-errors using varying starting velocities. Further, the simpler five layer model with a sharp boundary between upper and lower crust is used to perform stability tests on the model (final model set-up of depths and velocities can be found in Table 5.2).

layer	depth at top [km]	velocity [km/s]
unconsolidated sediments	-3.0	2.5
compacted sediments	1.5	5.6
upper crust	4.0	5.8
lower crust	33.0	6.7
mantle	43.0	8.1

Table 5.2: Final layer set-up and initial values used for inverting the velocity model.

5.3.2 Initial Hypocenters

By introducing random variance to the input data, while limiting the freedom of the modeling it is possible to check for bias and systematic shifts during the inversion. This step helps to review whether the solution space is adequately scrutinized. Here, the hypocenter relocations from a minimum 1D velocity model (see table 5.2) are shifted randomly and an attempt is made to back-locate them to the initial position.

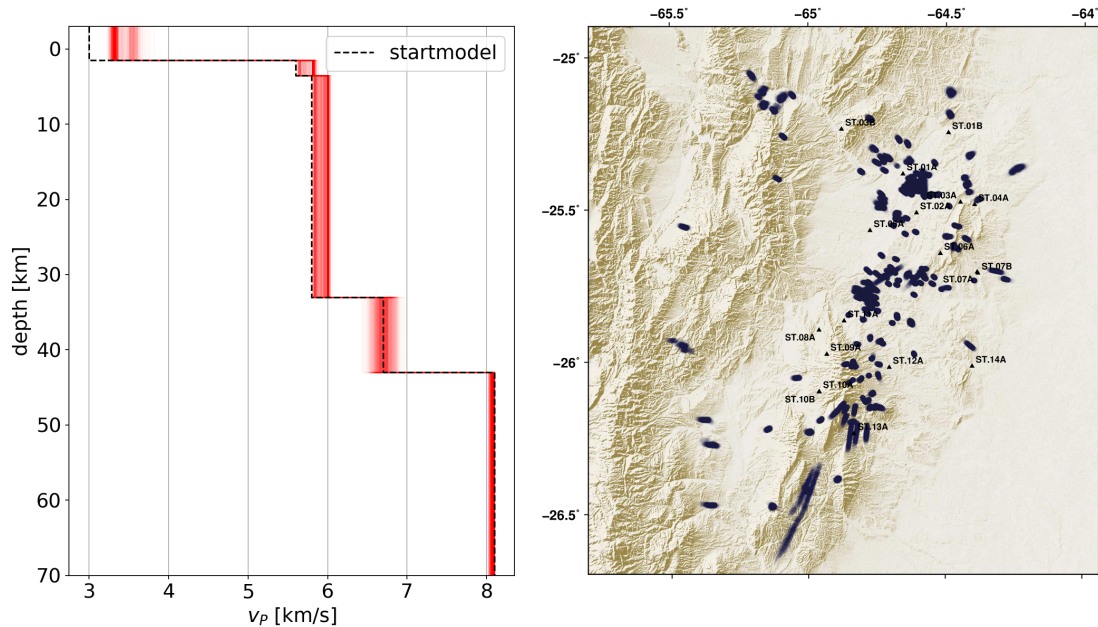


Figure 5.5: Results of the hypocenter variation test after 1,000 runs. The hypocenters are shifted randomly 10 km horizontally and at 5 km depth. *Left:* The resulting velocity models are shown in red and stay in close range to the starting 1D minimum model. *Right:* Map view of all resulting, relocated earthquake epicenters. Epicenters plotted with opacity for each run lead to blurring for unstable relocations. Triangles indicate position of seismic stations, stations SLA and AHML outside of map boundaries.

The minimum 1D velocity model used further as the initial input model. The resulting station corrections from this step have to be incorporated into the input station parameters, and the inversion procedure is adjusted so that VELEST inverts for the hypocenter location in every iteration and for the velocity model in every second iteration. The output hypocenter locations from the 1D minimum model are randomly shifted by 5 and 10 km horizontally and 2.5 or 5 km in depth respectively, because the horizontal uncertainty is two times higher than the depth uncertainty.

The results after 1,000 runs are shown in Figure 5.5. The final velocity models indicate an overall stable solution for the minimum 1D model with little variance and solely a small shift to higher velocities in the upper crustal layer. The event hypocenters are well back-located into a position, which coincides with the original location taken from the minimum velocity model estimation. A few exceptions with substantial deviations in northeast – southwest direction are located to the southwest outside of the STRATEGY network, where the location estimation has higher uncertainty. In general, the relocation deviation is proportional to the increase of the distance between the epicenter and the

mass center of the network. Nevertheless, no systematic bias is identified to disprove the stability of the used minimum 1D velocity model.

5.3.3 Jackknife Resampling

The jackknife resampling is an efficient tool to estimate the variance and potential bias in a data-set. To estimate the stability of the velocity modeling, the jackknife resampling is used to reduce a distinct number of input data points randomly and reestimate the 1D minimum velocity model. If the given minimum model (see Table 5.2) is stable and without bias, the residuals between the initial and reestimated models should be small. Here, the given data-set allows resampling to classes of input data: earthquake locations and stations. The first category intends to evaluate how consistent and independent the velocity modeling is. The latter identifies outlier stations, which increase the uncertainty (given by the RMS-error) of the model, and show the dependence on certain stations or the number of available stations in general.

Earthquake Resampling

In a classical resampling approach, each single event of the input catalog would be removed iteratively as an input parameter. However, the presented reduced catalog of 215 well located primary hypocenters is so robust that taking out a single event will insignificantly modify the resulting velocity model – and the residuals are close to zero.

Instead, a distinct amount of events (here 20, 50, and 100) are randomly chosen from the reduced catalog (see Section 5.2) and not used as input for inverting the minimum 1D velocity model. For an accurate inspection of the solution space, various initial velocities are used. The layer set-up presented in Table 5.2 remains unchanged, but the velocities are shifted by a random value uniformly distributed ± 1 km/s around the respective velocity assigned to the layer. For each jackknife resampling (20, 50, 100 removed events), 500 models are calculated.

The removal of 20 events from the catalog results in stable resolutions with limited deviations in each layer smaller than 0.1 km/s, although the starting velocities vary by ± 1 km/s. The shallowest sediment layers show lower velocities averaged over 500 models than modeled with the full data-set. The velocity values for the lower crust pose a remarkable discrepancy. Here, the inner crustal velocity contrast vanishes for most of the models and the lower crust barely results in velocities above 6 km/s.

In contrast, the final models estimated with 50 events fewer on average show even higher velocities than the initially assigned value for the lower crust. Overall, the variance in final velocity values is comparable to the outcome of the jackknife resampling with 100 randomly chosen events.

The most probable velocities for each layer in the jackknife resampling of 100 fewer events are distributed around the minimum 1D velocity model (see Figure A.5). The overall low variance in comparison to the variation of initial velocity values indicates a very robust model set-up and minimum 1D velocity model, even when using only half of the well-located events.

Station Resampling

The implementation of the jackknife resampling of the second input parameter, the available seismic stations, is similar to the previous stability tests. The layer depths are kept constant, while the respective velocity values are altered randomly by ± 1 km/s. Then, the estimation of velocity models is performed 200 times using all 215 well-located events, but iteratively leaving out the picks of one station at each step.

The resulting velocity estimations are without major interdependence of single stations. The median of RMS-errors varies around 0.32 s. Thus it is comparable to the value estimated for the minimum 1D velocity model (Section 5.3.1). The variance of velocities in all depth layers is comparable to the solutions presented in the previous stability tests. Similarly, the variance of the lower crust is the highest in comparison to other layers, but independent of the station which is left out from the inversion. One remarkable feature is the ambiguity of stable solutions in the upper crustal velocities inverted without using station AHML (shown in Figure A.6). This implies a higher dependence on the data recorded at that station to resolve good constraints on the velocity in the upper crust. As station AHML is located in the south and has greater interstation distances, this effect can be related to local crustal inhomogeneities, as changes in the lithology of the crust (i.e., the southern part of the study area is dominated by basement cored ranges, which are totally lacking in the northern part of the Santa Barbara System).

5.3.4 Geographical Subsets

An additional parameter able to introduce bias in the model is the geographic location, either event location or station location and spatial distribution. In the case of local inhomogeneities or lateral changes in the lithological composition of the crust, two geographically subsampled event catalogs can lead to different modeling results. Due to the north to south transition in geological features exposed at the surface, the study area is divided along -25.8° latitude, and two independent velocity models are calculated. This coincides geographically with the southern margin of the Metán-basin. In both approaches (dividing by hypocenter location or by station of the network), the same layer set-up as before is used, while the initial velocities are randomly shifted by ± 1 km.

Split of Earthquake Catalog

The first approach for dividing the data-set is applied straightforward on the earthquake catalog (see Section 5.2) by separating all events according to their primary hypocenter location. This leads to a northern earthquake list of 143 events and 72 events in the South. As discussed during the event resampling, reducing the catalog randomly by 100 events, the inversion is still capable of solving for stable solutions. Here, still, all stations are used to perform the velocity model estimation.

The results of the 1,000 model runs for each sector (see Figure 5.6) agree with the previous model results. Using only the earthquakes in the north, the ambiguity of stable solutions in the lower crust becomes more evident. Either, the velocity contrast diminishes and the low v_P of 6 km/s extends through the full crust or a second identical

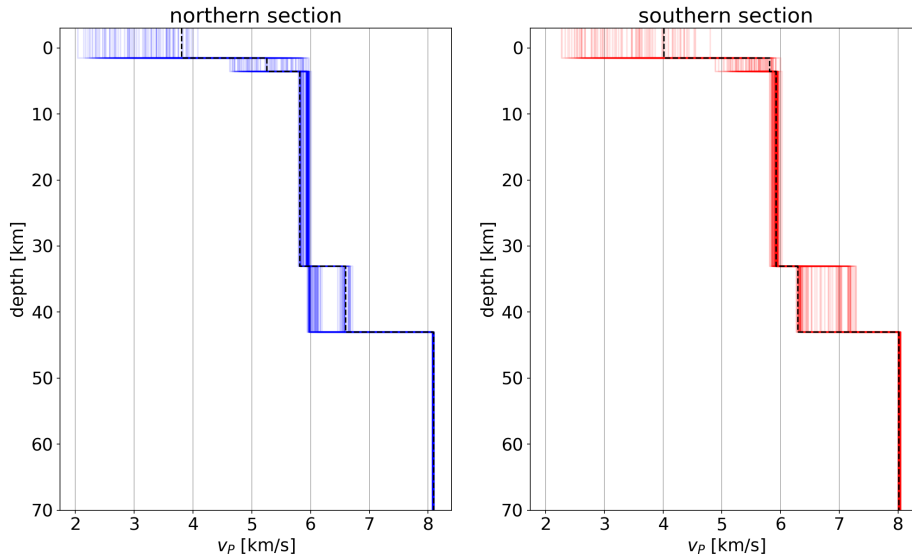


Figure 5.6: Results of velocity model using just events with epicenters north of -25.8° lat (blue) or south of that line (red). Only models with RMS-errors below the 10th-quantile are shown. The dashed lines show the models with the lowest RMS-errors. In total 1000 runs are performed for each sector.

stable solution is found around 7 km/s. The southern set of earthquakes solve for a less ambiguous stable solution, with homogeneous velocities along the full crust. In contrast, the southern velocity model has no stable solution for the shallowest sediment layer, while it ranges wider than the distribution of input values for that layer. Nevertheless, the RMS-errors derived from both event subsets are similar.

Here, the geometry between hypocenter and station locations has to be considered before the interpretation. With increasing epicentral distances, the chances of crossing raypaths increase with depth. Thus, this analysis is feasible to be sensitive to deeper layers in the model, but not for the shallowest part. In addition, the shallowmost part of the subsurface shows laterally high heterogeneities, i.e., thick basin in the north, metamorphic basement rock with elevated topography in the south. To better constrain the shallower layers the subsampling of the stations into geographical subnetworks leads to shorter epicentral distances.

Split of Seismological Network

After the collocation of the stations in two subnetworks, roughly north (including stations SLA, 01A, 01B, 02A, 03A, 03B, 04A, 05A, 06A, 07A, 07B, 11A) and south (including stations AHML, 05A, 06A, 07A, 07B, 08A, 09A, 10A, 10B, 11A, 12A, 13A, 14A), for each subnetwork a new reduced catalog of well-located events has to be created. Here, the

same rules as used in Section 5.2 are used to identify well-located events (>6 observations, 180° minimal azimuthal gap). This leads to a subset of 137 events for the northern and 84 earthquakes in the southern subnetwork.

After running 1,000 models with different initial velocities, two contrasting models for the two subnetworks result as a minimum 1D-model (see Figure A.7). The RMS-errors differ strongly for both data-sets (0.157s for the north, 0.266s for the south). The northern subnetwork presents very stable solutions with very small variance in the upper part of the crust, reproducing previous findings the lower crust and mantle bear higher instability. Here, the initial model is estimated without any damping of the mantle; otherwise, the lower crust is strongly overdamped as well and leads to physically unreasonable velocity values. For most of the 10% best models (determined by RMS-error), the lower crust merely prolongs the low v_P value of the upper crust and thus, shows a very strong crust – mantle boundary. On average, the southern subnetwork results in the same velocities for the uppermost crustal part. Below 33 km, the model is totally unconstrained as no deeper hypocenter exists in the resampled catalog for the southern subnetwork. Hence, the damping of the mantle velocity leads to no variance in that depth.

An overall systematic shift in model quality is not detectable or at least not explicable, by the limitation of available data. In the upper part of the crust, it can be stated with high certainty that spatial biases, due to lithological parameter changes are unnoticeable. Estimations of deeper structural changes are of high uncertainty, if possible at all. The lack of enough raypaths covering that part of the crust prevents accurate discrimination of spatial variation in the model. In the end, a single 1D minimum velocity model can be estimated with high confidence for the whole study area.

5.4 Final Velocity Model

Besides approaching a minimum 1D model for P-wave velocities, VELEST can also simultaneously invert for P- and S-wave velocities. After finding a stable solution for v_P from 5,000 model runs by averaging over the resulting velocities for each layer incorporating the best 500 models, an initial v_S model is calculated using a constant v_P/v_S ratio of 1.73 (see Sections 3.3.2 and 3.3.3), except for the mantle for which global averages give a value of 1.82 [81] [150]. Considering the higher uncertainty of S-wave picks, a weighting factor of 0.5 is applied to the S-wave data. The layer depth set-up, using five layers (Table 5.2), tested in the previous Section lead to good solutions for a wide range of stability tests. Again, to scrutinize the solution space properly, 5,000 model runs are performed with random ± 1 km/s alteration of the initial velocity values.

Only 10% of the resulting velocity models with the lowest RMS-errors are considered for estimating the final velocity model for the study area. The variance of RMS-errors is very small; the difference between the lowest and the 500th lowest RMS-error out of 5,000 model runs is 0.012s. Under the assumption it is a univariate distribution, and thus unambiguous, the median of the velocity distribution is defined as the most probable stable solution for each layer. The standard deviation characterizes the uncertainty of

the final velocity estimation. The v_P/v_S ratio is calculated for each model and each layer independently. Afterwards, the median and standard deviation of the distribution of each layer is used as discriminator.

layer	depth [km]	v_P [km/s]	v_S [km/s]	v_P/v_S
unconsolidated sediments	-3.0	4.16 ± 0.60	2.83 ± 0.11	1.45 ± 0.17
compacted sediments	1.5	5.71 ± 0.22	2.83 ± 0.11	2.02 ± 0.13
upper crust	4.0	5.81 ± 0.05	3.30 ± 0.04	1.76 ± 0.01
lower crust	33.0	6.65 ± 0.31	4.33 ± 0.08	1.54 ± 0.05
mantle	43.0	8.04 ± 0.07	4.49 ± 0.04	1.79 ± 0.02

Table 5.3: Final minimum 1D velocity model, estimated from the median and standard deviations of stable solutions at each depth layer.

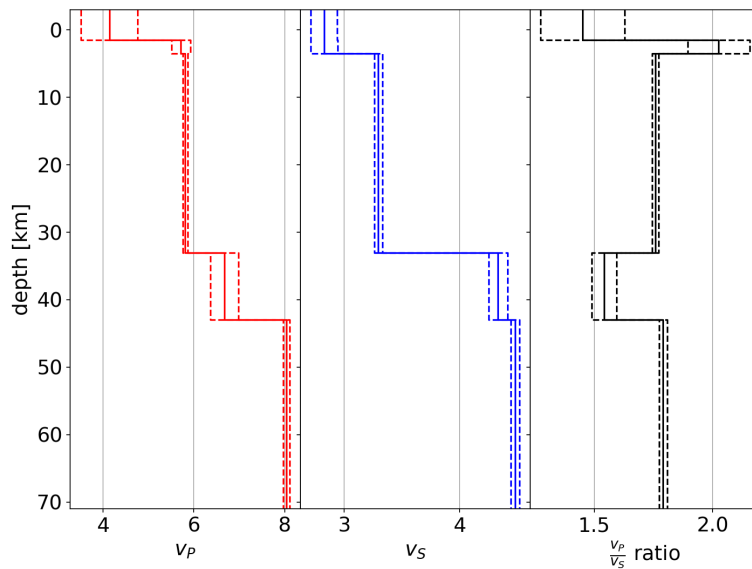


Figure 5.7: Final minimum 1D velocity model (solid lines) with standard deviations of each layer (dashed lines). *Left*: P-wave velocity, *center*: S-wave velocity and *right*: v_P/v_S ratio.

The RMS-error of the simultaneous inversion of both phase types increases by half a magnitude, in comparison to the P-phase only modeling. However, the variance remains unchanged, and the difference between the lowest RMS-value and the 10th quantile model is still 0.012s. The station correction values for P-wave arrivals remain stable, but S-wave station corrections show high negative values, averaged over all stations. This

issue is solved by applying strong damping (2.0 instead of 0.1) for station corrections (final station correction value distribution in Figure A.8).

The final velocity model estimation for P-waves is within the boundaries identified in the previous Section. However, the modeled S-wave velocities do not correlate with associated P-wave velocities. This becomes obvious when analyzing the v_P/v_S ratio for each depth layer. Here it is important to mention VELEST inverts for v_P and v_S , but not for the v_P/v_S ratio itself. The v_P/v_S ratio is an important parameter to conclude on the lithological composition of a layer.

In the two shallowest parts of the model, the v_P/v_S ratio deviates heavily, reflecting the wide range of possible velocities and velocity ratios for shallow unconsolidated sediments. For the uppermost layers of the model, various rock property parameters influence the velocities of the sediments (e.g., porosity, type of pore fluid, pore pressure, rock type) [171]. This reflects the strong heterogeneities in the lithological composition of the shallowmost part, also in vertical extension i.e., a thick basin of unconsolidated sediments on the metasedimentary basement. Lateral variations should be incorporated into the station correction values. Although strongly damped, the resulting model is still capable of recovering distinctive site conditions. For example, station ST.05A is located in the center of the Metán basin on top of a thick layer of unconsolidated sediments [42] leading to very high residuals of 1.4 s for S-waves.

Surprisingly, the stability of solutions for S-wave velocities in the shallow layers is higher than for P-wave velocities, although one would expect a higher number of crossing P-wave raypaths, due to their greater path length in shallower layers. This result is independent of the damping of station corrections. Hence, the variation of v_P/v_S ratios is mostly driven by the unconstrained P-wave velocity in shallower layers.

The stable solutions of the upper crust indicate v_P/v_S ratio close to the value of 1.73 estimated from the Wadati diagram (see Section 3.3.2). The v_P/v_S value is an average over the full raypath and therefore precise comparison is only valid, when considering the ray geometry and weighting with respect to the exact raypath in each layer. As discussed before, the mantle velocities are only constrained through damping according to a priori knowledge and refracted waves in the boundary surface.

Overall, the velocity values estimated by the minimum 1D velocity model infer a felsic composition of the whole modeled crust with lower than global average velocities (6.45 km/s [172]). This coincides with other models from Bouguer anomalies [173] and observations from well logs in the Candelaria region [14]. In the lower crust, velocities and velocity ratios show very unique results, which can only be explained by granodiorites with high SiO_2 content or quartzite as main lithological compounds [174]. In fact, the stability of the velocity throughout the full extension of the upper crust suggests a rather low heat flux in the study area [172].

Besides the velocity model and the station corrections, VELEST also minimizes the residuals for hypocenter locations. The resulting relocations for the reduced catalog used as the input data-set are shown in Figure 5.8. In comparison to the primary hypocenter locations (see Figure 5.3), the interevent distances of epicenters in event clusters are reduced. Individual epicenters delineate parallel to the NNE – SSW striking MBCTF [38]. In the cross-section profile perpendicular to the MBCTF, the hypocenters around

the epicenter of the El Galpón mainshock outline more closely a west-dipping structure throughout the whole upper-crust segment of the five layer model. This observation correlates with the fault plane identified from moment tensor solutions (see Section 1.3.2 and Figure A.2).

In comparison, the final 1D minimum velocity model is used to execute the hypocenter estimation with HYPOSAT (see Section 4.1) again. The local velocity model is used exclusively for events with epicentral distances of less than 1° ; more distant events are located using only a global velocity model [175]. By this, only the locations of events within the network can be improved. More distant events show larger epicentral distances or greater hypocentral depths than the primary hypocenter locations presented before, using the CRUST1.0 model [150] (see Section 4.3.2). Hence, I suggest updating the CRUST1.0 model for the data point at -25.5° lat, -64.5° lon with the presented velocity model, which is inverted for a very localized position.

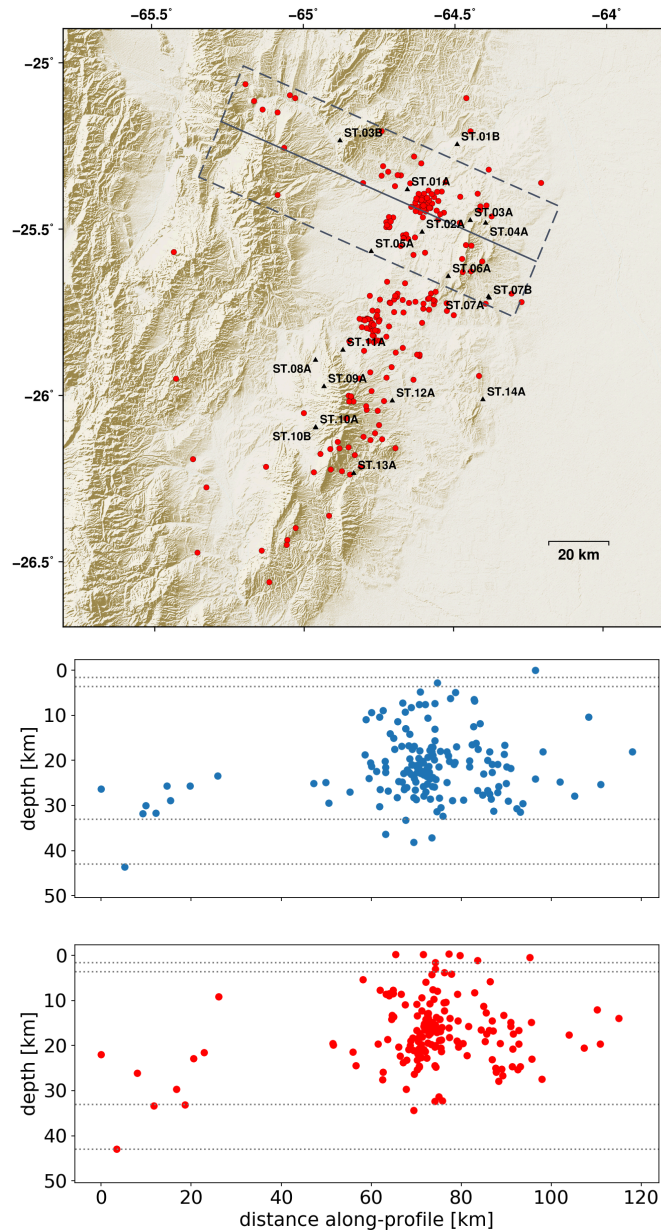


Figure 5.8: Relocated earthquakes as output from the VELEST model. *Upper*: Map of earthquake epicenters on a topographic map with station locations as black triangles and a solid grey line indicating the location of the profiles, with limits of included events as a dashed grey box. *Lower*: profiles through the study area, similar to Figure 4.2 using only hypocenters no more than ± 50 km on both sides of the profile. *Blue dots*: location of events used as input catalog (see Section 5.2) and *red*: hypocenter relocations estimated from VELEST. The grey horizontal lines in the profiles illuminate the transitions between the layers of the 1D minimum velocity model.

6 Topic V: Event Relocation

A major challenge in the use of seismological data to derive a high-resolution image of seismotectonic structures and processes is the reduction of uncertainties. Especially, location errors obtained from passive observation methods can be tackled using various approaches. As described in the previous chapter, the locations of supposedly already well-located events can be improved while reducing residuals together with a velocity model. Other approaches aim entirely for the optimization of event locations, e.g. double-difference relocation [176]. In this chapter, the concept of double-difference relocation is briefly explained as it is implemented in the HypoDD software package [177]. This software is then used to accomplish the relocation of the previously discussed dataset of local, crustal seismicity in NW Argentina (Chapter 4) in combination with the newly introduced local 1D velocity model.

6.1 Method

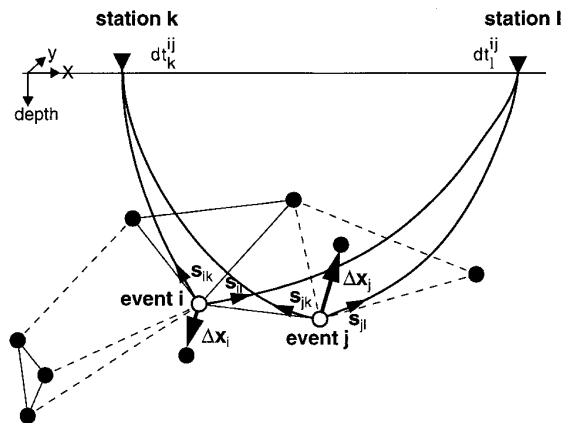


Figure 6.1: Sketch illustrating the concept of double-difference relocation, taken from Waldhauser & Ellsworth 2000 [176]. The initial hypocenter locations of two events i and j (open circles) are relocated (solid circles) along vector Δx . Each event is linked to neighboring locations by cross-correlation (solid lines) or catalog (dashed lines) data. The slowness vectors s correspond to the raypaths from the events to the respective station, leading to the observed travel time difference $dt_{station}^{ij}$.

For two nearby located events, the major part of their raypaths to the same station are similar. The travel time difference ($dt_{station}^{ij}$) of those events observed at one station is proportional to the distance of their hypocenters. This applies only if the spatial separation of the hypocenters is small in comparison to the length of the raypaths and the scale length of the velocity heterogeneity. With the close origin of both events, differences in the absolute errors reduce to very small relative errors, depending on the parts of the raypath in the source location. Therefore, the relocation of events can be performed with very high accuracy. The actual double difference is then defined as the residual between observed and theoretical travel time differences:

$$dr_{station}^{ij} = (t_{station}^i - t_{station}^j)^{obs} - (t_{station}^i - t_{station}^j)^{cal} \quad (6.1)$$

The linking of two events is established through the traveltimes difference at one station, which can be realized using two sets of data: catalog or cross-correlation data (see Figure 6.1). Traveltime difference data derived from the catalog data reflects information close to the true location and thus leads to higher stability over greater distances. Hence, catalog data helps to justify the relative location of multiplet centroids or single events. Cross-correlation time differences are more applicable for events within clusters with interevent distances smaller than $1/4$ of the wavelength of the highest frequency of importance in the seismogram [176]. The sources of two earthquakes of that separation are highly similar and produce matching waveforms, which can be exploited through cross-correlation. This approach reduces the traveltime difference uncertainty up to a factor of 30 compared to catalog data based uncertainties (cross-correlation precision about 1 msec).

A big advantage of the HypoDD software is the use of a joint hypocenter determination (JHD) method. By this, the combination of all hypocentral pairs with all stations leads to a system of linear equations, for which the partial derivatives of the double difference are inverted simultaneously. The full mathematical description of the problem can be found in Waldhauser & Ellsworth, 2000 [176]. It is important to mention that the inclusion of the different data sets (catalog or cross-correlation) is performed in different steps of the inversion, as they strongly influence the final hypocenter locations due to their different relations to the absolute and relative location uncertainty.

6.2 Data Preparation

The preparation of the hypocenter data starts with a conversion of the QuakeML and StationXML catalogs into a FORTRAN-readable format used for the relocation software package of HypoDD. For this purpose, Python based functions are developed ¹ using the pyrocko package [76]. Simultaneously, the catalog of primary hypocenters is reduced to a regionally (corner coordinates: -65.6° lon, -64° lon, -26.7° lat, -24.8° lat) limited subset, to assure consistency and well-constrained initial locations. By this, the workload

¹<https://github.com/marzeck/xml2hypoDD>

to calculate differential times using waveform cross-correlation is reduced. Events with too high separation are already excluded, and by limiting the data-set to events in the proximity or within the seismological network, the slowness vectors of the double-difference for each event – station pair is less ambiguous. In general, the method works only for constant slowness vectors. This is valid as long as linked events are sufficiently close together, and the raypath geometry does not change. The 1D velocity model derived from VELEST (see Section 5.4) used here shows a high homogeneity for the upper crust, the depth range into which most of the observed earthquakes fall. This might increase the stability but is only valid for the regionally subsampled event catalog covering the same source region, for which the velocity model is inverted.

The actual linking between event pairs is performed by `ph2dt`. This subprogram of the `HypoDD` software seeks links in the catalog data and at best, resulting in a chain of pairwise connected events providing a shared network, in which every event is connected with the other. The programs' parameters were chosen in a way, that at maximum, all 643 events in the studied region could be connected. The maximum distance between an event pair and the stations is set to 250 km, twice the maximal interstation distance of the STRATEGY – network (without the stations of AHML and SLA of the national permanent network). Interevent search radii are limited to be smaller than 12 km, a value slightly higher than suggested by the authors; as seen in Section 4.3.2, local hypocenters distribute over a rather large space, while the crust preserves homogeneity throughout a big vertical range (see Section 5.4). The distinction between "weak" and "strong" links to a neighbor is defined by the number of phase pairs, here eight phase pairs (one for each degree of freedom: three spatial, one temporal per event). Internally, `ph2dt` also removes outliers from the catalog; events with delay times greater than the maximum expected delay time, calculated from synthetic rays between two events in the foci area (further explanation in [177]).

Gathering nearby strong events into groups of individual clusters is performed by `HypoDD` itself for stability reasons. Hence, the computation of cross-correlation differential times has to be performed before, based on observations from the catalog data (picked arrival times). For the purpose of more efficient data handling, the cross-correlation procedure of the Python-based `hypoDDpy`², which is based on the `ObsPy`-package [90], was rewritten using the `Ppyrocko` package [76]. This effort reduced the total computation time of all cross-correlations (in total 88,042 correlations) of the 8,371 event pair combinations to approximately 25 minutes; event pair combinations are previously identified by `ph2dt`. For each event pair, the event catalog (chapter 4) is explored for picks at the same stations but using only confirmed picks to assure robustness. For each event pair with picks of the same phase at a common station, the bandwidth filtered (highpass: 1 Hz, lowpass: 15 Hz) data is cut 0.05 s before and 0.2 s after the assigned pick time. The absolute pick time is subtracted so that the cross-correlation gives the relative differential times. Only times with maximum cross-correlation values above 0.8 are stored for further processing, leading to 1,802 P-phase and 2,336 useful S-phase differential times.

²<https://github.com/krischer/hypoDDpy>

The quality of the relocation strongly depends on the iteration scheme and its data weighting at each inversion step. Here, 25 iterations are used in total, with the weighting scheme being updated after every five iterations. As described before, catalog data is of high importance to resolve relocations with greater inter-event distances. Hence, during the first iterations, the cross-correlation data is down-weighted to support stability in absolute locations, and events can fall into clusters. While P-waves are fully weighted with 1, S-wave differential times are weighted 0.5, due to their higher uncertainty; cross-correlation differential times of S-phases are also weighted only half the value assigned for P-waves. During the first five iterations, no further weights are applied to determine a cleaned relocation catalog with outliers removed, portraying first structure outlines. In the iterations, 6 – 10 maximum distances between event pairs are limited to 6 km (average minimum horizontal uncertainty for the geographically subsampled input catalog) to increase robustness. The residual threshold is set to 8 s (for further explanation of that value see [176]). Starting with iteration 11, the catalog data is down-weighted (P-phases: 0.01, S-phases: 0.005) and cross-correlation times up-weighted, in order to redefine relative locations of events forming multiplets at a high level of accuracy. Strong links from cross-correlation differential times are only valid for small interevent distances; therefore, this distance is limited at maximum 2 km in the iterations 11 – 20. The residual threshold of 8 s was only activated after iteration 16. The last five iterations were used to resolve interevent structures; thus, the event separation limit is set to 500 m.

6.3 Relocation Catalog

After performing the relocation procedure as described before, the output catalog contains 408 relocated events. The difference in the number of earthquakes used as input is caused by the removal of outliers and badly linked event pairs throughout the inversion.

Overall, the spatial distribution of earthquake hypocenters is comparable to the distribution of primary hypocenters (see Section 4.3.2 and Figure 4.2). Within the network, earthquakes distribute all through the upper crust and form a seismogenic zone between 10 and 30 km. Laterally, the event epicenters align well with the NNE – SSW striking geological features identified and discussed before. While in the northern half of the studied region two parallel alignments can be tracked, the southern half displays more scattered epicenters in a map view. Highlighting two special clusters of events, the first located north of station ST.02A coincides with the location of the 2015 El Glapón event and reveals its aftershock distribution. The second, northeast of station ST.11A, connects aftershocks of a separated event in September 2015. Hypocenters to the west of the network are located in the lower crust, confirming robustly the occurrence of those deep seated crustal events.

In profile view perpendicular to the strike of geological features (see Figure 6.2), the continuing connection of deeper-seated earthquakes from the west into the seismically highly active parts in the central part of the network becomes more apparent. This confirms the west to East depth reduction of the brittle deformed zones and the aseismic nature of the shallow part of the Eastern Cordillera observed in the spatial distribution

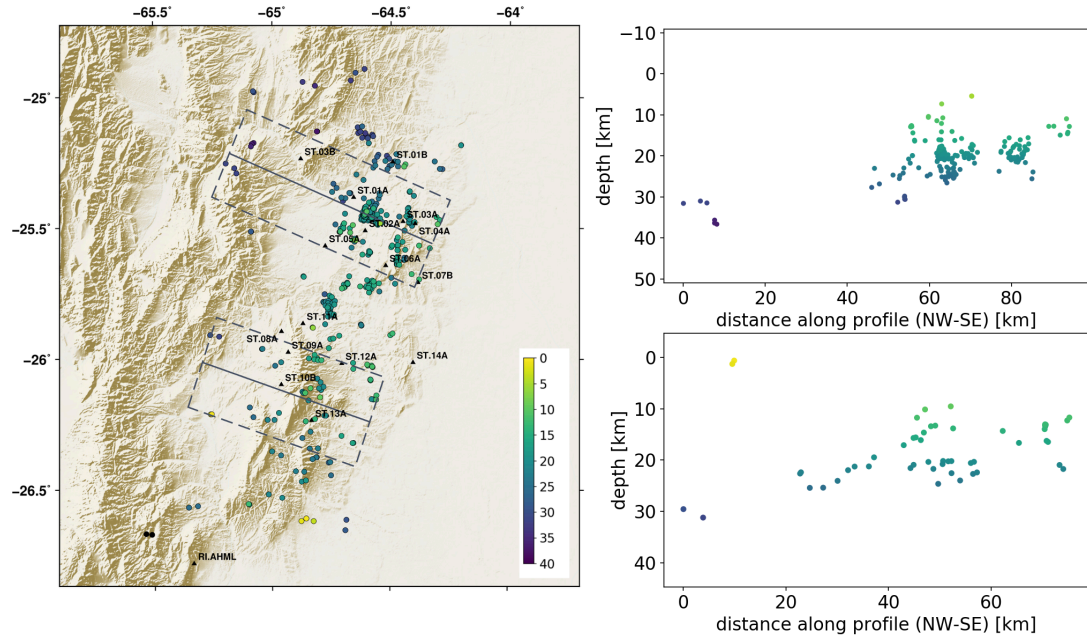


Figure 6.2: Earthquake locations after relocation using HypoDD. *Left*: topographic map with stations of the STRATEGY network and epicenters of relocated events, color-coded by depth. Solid lines indicate the position of profiles shown in the right Figures, with dashed lines outlining the boundaries of events taken into account for the profile. *Upper right*: vertical profile showing events 20 km north and south of the northern profile, *lower right*: southern profile from the map. Both profiles have equilateral axes.

of primary hypocenters in Figure 4.2. Especially in the southern profile (Figure 6.2, the relocated hypocenters align well into a subhorizontal, slightly west-dipping plane emerging underneath the basement-cored *Sierra de la Candelaria* range.

In the northern profile, the presence of the spacious aftershock cluster of the 2015 El Galpón event (see Section 1.3) complicates a detailed structural analysis. The aftershock hypocenters align into a steep, subvertical plane with the centroid (of the upper subcluster) positioned at 19 km depth. The overall extension of the greater cluster reaches from a depth of 17 to 25 km. However, with the presented data, it is unfeasible to outline the exact size of the cluster and to decipher whether the lower subcluster is part of the aftershock sequence or related to the widely distributed deeper-seated crustal deformation. To the east, a second cluster of events aligns parallel to the MBCTF. These events are limited in vertical range (15 – 22 km) and locate exactly underneath the largest topographic expression of the *Cerro Colorado* range.

A full description of the distribution of all seismic events regarding a holistic seismotectonic interpretation is given in Chapter 8.

7 Topic VI: Focal Mechanisms Inversion

Besides the rigorous analysis of tectonic geometries from spatial event distributions, the kinematic information adds an important dimension to the constraints of a seismotectonic study. Manifold indicators are used to determine the regional stress conditions. The group of in-situ measurements contains observations from boreholes or geological fault outcrops. These localized point measurements are not always available and also limited at depth. Instead, passive, second-order observations (e.g., seismic waves, GNSS-data, InSAR) in actively deforming regions are used to invert for seismic source parameters, which are then transformed and incorporated into stress maps [178].

Here, the far-field observations of the STRATEGy seismological network (see section 2.2) is used to reconstruct the kinematic parameters of the source of individual earthquakes. By this, a higher-order interpretation of the seismotectonic settings of the study area will increase the robustness. The inversion of all source parameters, described as moment tensors, is mostly performed by optimizing the residuals of full waveforms between synthetic and observed data. This approach heavily depends on the calculation of Green's function databases [80] [179]. In a small-scale seismological study as presented here, the calculation of a Green's function database becomes computationally very costly. On the one hand, due to the high complexity of raypaths and their dependence on a high resolution velocity model. Further, the dominant frequencies of local earthquakes require such high frequency Green's function databases, making it impractical with current, commonly used software.

A more robust and classical approach for focal mechanisms inversion in close epicentral distances is the use of first motion polarities. Here, the geometric relations between source and receivers, in combination with the local velocity model, are the main constraints for the effectiveness of this inversion approach. Well-constrained focal mechanisms depend on a good coverage of the focal sphere. High quality location estimations and a good resolved velocity model then reduce the errors when calculating the ray parameters.

Various available software packages perform focal mechanism inversion using phase polarities and sometimes in combination with amplitude ratios. Widely used FORTRAN based software packages are: FPFIT [180], HASH [181] and FOCMEC [104]. Following the path of processing the data in a Python-based environment, the newly developed software package MTfit [113] [182] is used, to derive focal mechanisms based on polarity observations. MTfit opposes to the previously mentioned FORTRAN software as the inversion process operates a Bayesian approach, optimizing for the uncertainties of having a sampled model based on the observed data. This approach works with polarity observations and can be extended with relative amplitudes or amplitude ratios. So, the possible number of free parameters in the inversion can be increased and it is possi-

ble to estimate the full moment tensor. However, the double-couple only estimation is performed here. A brief introduction of the method is given in the following section.

7.1 Method

The source function of an earthquake can be decomposed into the source-time function and the spatially dependent moment tensor. In the case of microseismicity, the source is approximated as a point source, which erases the spatial and temporal dependence of the source-time function, and it is possible to describe it mathematically as a step function. While the angular momentum is conserved, the symmetry of the moment tensor will reduce to six independent components. Through normalization the moment tensor is then defined after [183]:

$$\sum_{i,j=1}^3 M_{ij}^2 = 1 \quad (7.1)$$

The normalized moment tensor has five independent components. However, in the study area only tectonic deformation is expected. By forcing the model to resolve for a double couple solution reduces the system to three independent components (strike, dip and rake). A full description of the inversion process, including the full mathematical derivation and rigorous stability tests, is found in Pugh et al. 2016 [182].

$$p(\text{model}|\text{data}) = \frac{p(\text{data}|\text{model})p(\text{model})}{p(\text{data})} \quad (7.2)$$

Using only first-motion polarity observations prevents a linear inversion approach. The Bayes' Theorem [184], as shown in equation 7.2, allows to estimate the likelihood of observing a particular model, given the observed data. The uncertainties of numerous parameters affect the source inversion, which also show interdependences. To remove the interdependence of two parameters when calculating the joint likelihood, marginalization is used [185]. By integrating over the joint probability density function (PDF) for one variable, the dependence is reduced to that parameter, while taking all uncertainties into account. [182] have shown, the Gaussian distribution has maximum entropy and, therefore, it is the first choice to describe the error distribution. With de-measured data, the PDF is then only depending on the standard deviation σ .

Here, only first-motion polarity data is used and therefore the prior PDF for a given polarity is defined as [182] [186] [187]:

$$p(Y = y|A, \sigma_y, \bar{\omega}) = \frac{1}{2}(1 + \text{erf}(\frac{yA}{\sqrt{2}\sigma_y}))(1 - \bar{\omega}) + \frac{1}{2}(1 + \text{erf}(\frac{-yA}{\sqrt{2}\sigma_y}))\bar{\omega} \quad (7.3)$$

with the error function:

$$\text{erf}(x) = \frac{2}{\sqrt{\pi}} \int_0^x e^{-t^2} dt \quad (7.4)$$

Y is the polarity and A the amplitude. The authors in [182] state, that the uncertainty σ_y is difficult to be estimated in a manual polarity picking and should be left as a user-defined parameter. Here, I used the value 0.1 as a confidence interval for the uncertainty of the pick polarity σ_y , which is further defined as the given standard deviation using a Gaussian noise model during the marginalization of the polarity PDF over the error in the amplitude, while the polarity can only have values of 1 and -1, and the amplitude is normalized to take values between -1 and 1. $\bar{\omega}$ represents the mispick probability, due to falsely assigned polarity or trace inversion of a an incorrectly manufactured instrument. However, as shown in Section 2.3, the instruments recording correctly and no trace inversion is expected in the data-set.

The uncertainties of the location and the velocity model are derived by varying the receiver locations on the focal sphere, sampled for different possible event locations. By marginalizing over the hypocenter positions, the resultant likelihood can be incorporated into the model process. Possible moment tensor solutions are sampled randomly with one of the three implemented sampling algorithms: Monte Carlo random sampling and Markov chain Monte Carlo, as Metropolis-Hastings approach or reversible jump technique. The random sampling was favored, due to computational efficiency and the large number of events for which the focal mechanism calculation needed to be performed. For each event, $2.5 \cdot 10^6$ moment tensor samples were used, out of which 60 to 80 % non-zero solutions could be analyzed. Further, only the solution with the highest probability value is kept; the moment tensor, which has the highest probability to be true for the observed data. In order to be able to inspect the stability and unambiguity of the solution, a quality plot of all best 0.01 % solutions combined (out of the $2.5 \cdot 10^6$ million samples) is generated and stored.

7.2 Data Selection and Preparation

In comparison to the synthetic data-set used for the stability tests in Pugh et al. 2016 [182], the available number of polarity observations per event in the presented data-set is comparatively small. To assure satisfying results, the best resolved locations and velocity model were used to compensate for the poorly resolved polarity uncertainty, introduced by the manual picking.

Hence, the relocated catalog obtained from HypoDD is used to explore focal mechanism of accurately located events. From a simple geometric calculation, the azimuth between event and receiver can be determined as the first input parameter. The takeoff angle is then calculated using the `cake` [76] ray-tracer tool from the `pyrocko` package. Here, the newly derived local velocity model presented in Chapter 5 is used to compute seismic raypaths from the relocated event hypocenter to the receiver.

Comparable to the input data used during the determination of the local velocity model, the resulting focal mechanisms are restricted by the minimum azimuthal gap between the used observed rays ($gap < 180^\circ$). The efficiency of resolving the true focal mechanism does not directly rely on the number of stations. Moreover, the geometric

distribution of stations regulates whether or not the focal sphere is sampled properly with thorough observations. This leads also to a dependence on the focal mechanism orientation itself, as observations close to the nodal planes are error-prone in the picking procedure.

7.3 Results

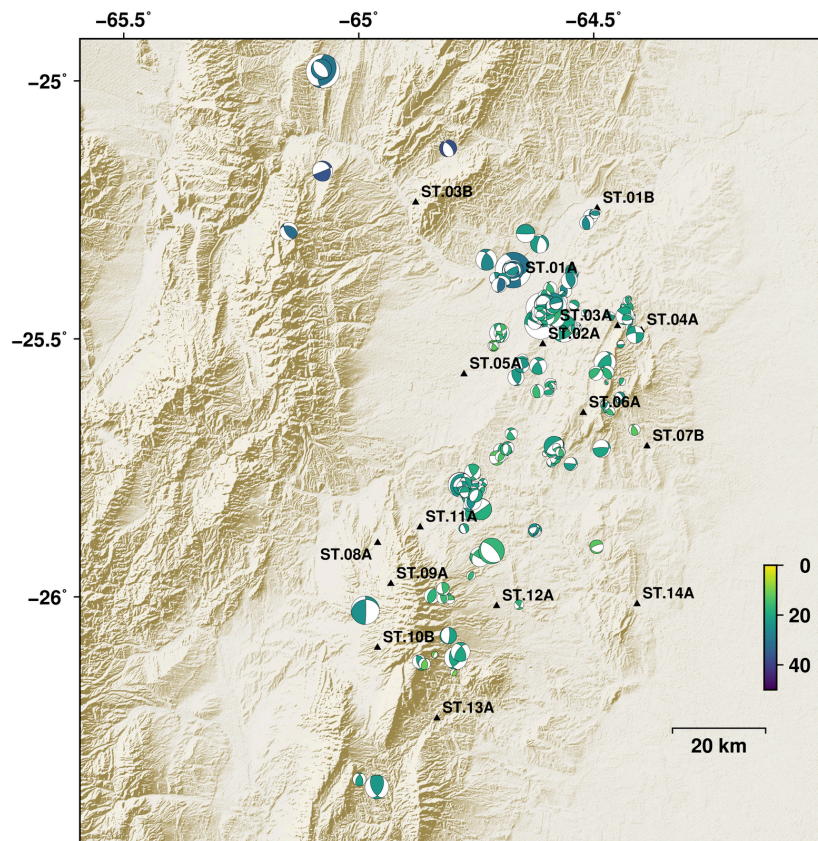


Figure 7.1: Topographic map with stations of the STRATEGY-network (black rectangles) and the locations of 208 focal mechanisms. The size of the beach balls correlates with assigned magnitudes and the color-codes represent the hypocentral depth.

Out of the 409 relocated events, 208 earthquakes have an appropriate azimuthal coverage. Except for two shallower and two deeper events, their hypocentral depth span continuously between 9 and 31 km. Deeper events are mostly located in the northwestern part of the studied area (see Section 7.3.5). Events underneath the Eastern Cordillera

could not be included in the analysis, due to bad azimuthal coverage and poorly linkage between events in the relocation process.

The majority of the source inversions results in thrust mechanisms with north to south oriented strike orientations (see Figure 7.2). Due to the probabilistic characteristic of MTfit, no high-precision result can be discriminated for all events. Moreover, the most probable solutions are estimated from the distribution of all unsupervised source parameters. Hence, the overall stress regime in the study area is compressional, as suspected from previous studies (see Section 1.1). Other results show variations in strike orientations or even strike-slip mechanisms. The occurrence of alternate focal mechanisms has to be discussed with respect to the related seismotectonic structure, taking into account further topographic and geomorphological information, as well as previous geophysical studies. Before the discussion below, individual, outstanding focal mechanisms are controlled manually based on hypocentral uncertainties and adequate focal sphere sampling.

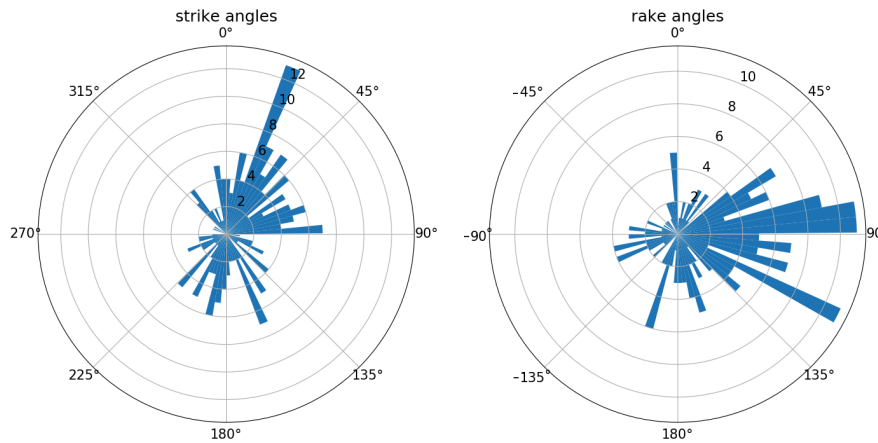


Figure 7.2: Polar plots of source parameters of events shown in map 7.1. *Left*: Strike angles and *right*: rake angles. Both plots indicate a high probability for NNE – SSW striking thrust faults.

7.3.1 El Galpón Aftershock Cluster

The earthquakes located around the 2015 El Galpón mainshock form the biggest cluster within the seismological network, including several events with magnitudes greater than ML 3. As discussed after the relocation, the locations of these events align parallel to the estimated orientation of the NNE – SSW striking MBCTF. The majority of the focal mechanisms have a strike oriented parallel to the strike of the fault inferred by Iaffa et al. [38]. With respect to the threedimensional alignment of hypocenters (see Section 4.3.2) along a steep dipping plane and the dip angle derived from the moment tensor of

the 2015 mainshock using teleseismic observations (see table A.2), the presented focal mechanisms support a west-dipping steep thrust fault.

The rake angles of these events indicate pure thrust faults, while the main shock had an oblique component in the moment tensor. Three thrusting events, including a ML3.7 event, show opposing strike angles oriented in east – west direction. These earthquakes potentially compensate for the lack of oblique deformation, indicating a stress field with a maximal compressive stress vector, which is not oriented perpendicular to the strike of the major fault.

7.3.2 Rosario Aftershock Cluster

The observed focal mechanisms of events located around the location of the event, which occurred in September 2015, are very similar to the observations in the El Galpón aftershock cluster. This suggests a comparable tectonic regime. As the events and their strike align very well for both clusters, they refer to the same structure. Hence, the Rosario aftershock cluster indicates the southernmost extension of the MBCTF. As no primary hypocenters could be observed between these two clusters, the focal mechanisms are important indicators, besides the observations from reflexion seismic profiles [38], for the continuation of the fault cutting through the whole Metán basin.

7.3.3 Sierra de la Candelaria

Compared to the northern sector, the seismicity underneath the *Sierra de la Candelaria* is characterized by a smaller event rate and disparate hypocenter distribution. The orientation of focal mechanisms reflect roughly the overall expected stress orientation of the study area, which leads to strike angles parallel to the strike of the basement-cored mountain range. The focal mechanisms are poorly constrained because many stations in this part of the study area suffered from data loss (see Figure 2.6 and Section 2.2.3). Many events to the south and east of the *Sierra de la Candelaria* were excluded automatically from the data-set, due to insufficient azimuthal coverage, preventing an in-depth analysis of this part of the studied area.

7.3.4 Cerro Colorado

Earthquakes located underneath the *Cerro Colorado* align exactly north – south, along the highest topographic expression of the homoclinal ridge. Strike angles of small magnitude events in the central part connect well with the overall alignment of hypocenters and the strike of the mountain range.

In the northern end, where the range plunges into the basin, noteworthy rake angles can be observed. Several events with strike-slip mechanisms align between the El Galpón aftershock cluster and the northern end of the *Cerro Colorado*. More evident is the positioning of events to the south, where earthquakes align east – west from the Rosario cluster to the southern end of the range. The focal mechanisms reveal mostly north to south striking thrust events, together with sporadic occurrence of strike-slip events.

7.3.5 Decollement

Only for a limited number of events high-precision relocations are determined in the lower part of the seismogenic zone, where primary hypocenters form a decollement like structure (see the profile in Figure 4.2). Due to the insufficient station distribution, the observed polarities do not sample adequately the focal spheres of those events. This leads to precarious results and prevents robust insights for this event category and the driving parameters in this depth range.

8 Topic VII: Seismotectonic Interpretation of the Study Area

In the above Sections, the application of multiple techniques enables the estimation of a diverse set of parameters, which characterizes crustal petrophysical boundary conditions and confines limits of seismotectonic-related processes. Based on these observations, the composition and the internal structure of the Central Andean foreland is discussed for the whole crust; this allows constraints of previously inaccessible depth ranges and potentially leads to future open research question in related geoscientific fields. In addition, implications on the recent tectonic processes in the study area are extracted and discussed, providing substantial new data-driven information about the foreland evolution in NW Argentina.

8.1 Petrological and Geophysical Parameters

The vertical composition of the study area is rather simple and homogeneous for an extended part of the crust. Thus, the metasedimentary Puncoviscana and the low-grade metamorphic Medina formations [52] [188], assembling the basement, apparently extend through the whole upper crust, down to approximately 33 km. The exceptional velocity ratio modeled for the lower crust concludes changes in the petrophysical conditions, while the composition bears high SiO_2 content and supports the felsic character (e.g., granodiorite [172]) throughout the whole crust. Hence, the studied region of the foreland is part of the Andean orogenic plate. Unfortunately, the existence of a mafic lower crust cannot be excluded from the observed model; then, the previously named felsic, lower crust, is actually a mid-crustal layer.

The observation of brittle deformation in the transition between upper and lower crust has major impact on the brittle – ductile transition zone and associated physical parameters, e.g., yield strength, temperature gradient. Especially, the increased SiO_2 content leads to temperature-dependent velocity changes at high pressure, due to phase transition [189]. However, the velocity is not directly proportional to fracture density [190]. Ibarra et al. 2019 [173] propose the increase of the thermal gradient within the lithosphere, and the decrease of its strength, support the deformation due to the transition from the felsic weak crust, of the orogenic plate, into the cold strong mafic crust to the east of the study area. So far, the spatial extension and width of that transition zone remains unresolved with currently available data-sets. Possibly, geodynamic models could solve, whether the adjacent felsic – mafic regimes even behave like a continent – continent collision zone. Nevertheless, the presented velocity models facilitate to con-

strain uncertainties of such a geodynamic model and its related, underlying processes [191] [192].

In regions of active shortening, greater depths of earthquakes develop when colder temperatures of the shallow crust are transported down by underthrusting [193]. With respect to the proposed continent – continent collision, and the available data, continental underthrusting of the Brazilian lithosphere cannot be excluded. In fact, such a process would explain the low heat flow, inferred by the homogeneous velocities in the felsic crust.

8.2 Seismotectonic Interpretation

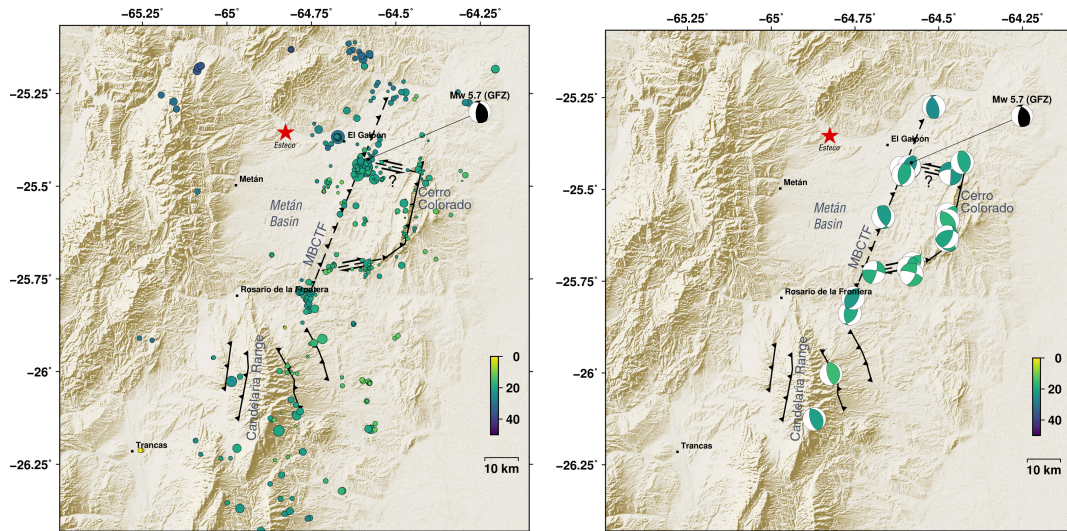


Figure 8.1: Topographic maps with high-resolution earthquake data and identified faults with Quarternary or recent activity. Dashed lines indicate blind faults, showing activity without surface expression. The red star shows the position of the ruins of Esteco. *Left*: Relocated epicenters overlay the tectonic map. *Right*: Focal mechanisms with uniform size are plotted on the tectonic map. Only supervised events are shown.

Highly accurate seismological observations are presented in the above sections and are used now, to map faults in the study region. The spatial distribution of relocated earthquake epicenters reveal sections of increased event rates, in the northern half of the study area around the Metán depression. The areas of increased seismicity trace precisely previously known and unknown faults.

At first, the MBCTF was identified in seismic reflexion profiles, classified as an inversely reactivated normal fault [38], and here it is shown to be active and the host structure responsible for the 2015 El Galpón Earthquake (see Section 1.3) and the in-

independently preceding Rosario Event. Despite the high activity, no surface expressions (e.g., fault scarps) are reported. Therefore it is a blind fault with ongoing deformation limited between 10 and approximately 30 km. However, the evolution of minor relief (30 m over a 5 km profile) on top of the fault drives river network adaptations, offering potential for future geomorphological studies. With an overall length of 75 km, this is the largest, individual seismotectonic structure in the studied area. The joint examination of focal mechanisms and observed hypocenter distribution (see Figure 8.1) concludes a west-dipping fault, opposing the estimations by Iaffa et al. [38]. It is important to mention, the examined depth ranges of seismic and seismological techniques hardly overlap, and changes in the fault geometry between 8 and 10 km could be missed. The dip of the fault also implies further possible links to the deep seated crustal seismicity, which are discussed separately.

The existence of a west-dipping thrust fault underneath the *Cerro Colorado* was already reported by Mon et al. [59]. Here, the existence is verified by strike parallel focal mechanisms, representing ongoing deformation underneath the cuesta range. Microseismicity at the southern end of the range align in east – west direction, linking the range with the Rosario aftershock center and the MBCTF. Strike-slip faults in this part were already suggested from geological observations and are now evident in the focal mechanisms; one exception is event 469 (see Appendix), which possibly indicates a rotation of the right-lateral fault towards north, the strike-orientation of the *Cerro Colorado*. The overall length of such the fault was not reported before. A similar pattern is observed between the northern edge of the *Cerro Colorado* and the El Galpón aftershock cluster.

Both structures could act as transfer faults, transporting strain further eastwards into the foreland. In this part, the MBCTF only shows very limited seismic activity. Thus, the interior of the Metán basin prevents strain-release and instead, transfers the strain further east into the foreland, along these east – west striking structures, pushing the *Cerro Colorado* as a spur into the Chaco-Paraná-basin. The higher activity of the southern transfer zone is related to the geometric relationship between the strike orientation and the principal stresses. Here, thrust and strike-slip mechanisms compensate the oblique deformation along the ENE – WSW striking fault, i.e., through flower structures. Geological observations of the northern transfer fault are not expected in this remote and difficult to access area. The strike of the fault is parallel to the main principal stress and perpendicular to the bedding of the surrounding sedimentary units.

The eastward strain propagation along distinct deformation zones is also visible at depth (see Figure 4.2). The deformation along the steep, west-dipping inverted normal faults in the eastern part of the Metán basin can be traced downdip, up to 30 km below the surface. The deep crustal continuation of the deformation zone follows a decollement-style and flattens until it reaches nearly Moho depth, subhorizontally underneath the apparently aseismic Eastern Cordillera. This is in stark contrast to previously published geometries inferred by balanced cross sections [6] [34] [194]. On a global scale, the observed hypocentral depths are remarkable but in comparison to other actively deforming mountain fronts (e.g., Himalayas or Tian Shan) not totally unexpected [71]. In contrast, the rate of activity at these depths are remarkable.

The observation of a deformation zone affecting the whole crust holds various implications about lower crustal, petrophysical conditions, e.g., temperature, composition (including mineral phases), stress field. Incorporating other observable parameters and data-sets into modeling approaches can estimate for boundary conditions given the observed deformation. In addition, future models could answer, whether an east-vergent decollement within the Andean plate or a westwards oriented underthrusting of the mafic crust takes place.

The southern section underneath the *Sierra de la Candelaria* is characterized by earthquake locations, disparate in space and time. The mapped faults in the Piedmont of the basement-cored range are the result of flexural slip deformation [14] and supposedly forced through the upfolding of a fault bend fold (Arnous, in prep.). Unfortunately, the seismological observations do not promote any of the suggested ideas, regarding the evolution of that mountain range. Further modeling is inevitable to describe the tectonic evolution in detail. However, the mapped faults in the Piedmont bear only a minor hazard potential, due to their low dip angles and shallow appearance.

8.3 Seismic Hazard Estimation

The unawareness of the existence of a fault bears a high risk, even in well studied regions, as it became evident earlier this year [195]. Here, two new potential faults are identified. In a slow deforming region as the Santa-Bárbara-System with long recurrence intervals, the activity of all faults cannot be resolved within a 15 months field survey. Hence, the presented tectonic map is an improvement of the current seismotectonic understanding of the study area.

The two newly suspected faults are 15 to 23 km long and can hold a potential maximum M6.5 earthquake [63]. Under the assumption, they are of secondary order and used to transfer stresses into the foreland, their potential to accumulate stresses then is low.

As pointed out above, the MBCTF is the longest, active fault observed in the study area. When considering the two events occurring in 2015 as the bounding asperities of a stronger, previously ruptured main shock, because seismicity at this part of the fault is comparably low, the along-strike interevent distance is 40 km. Under the assumption the full downdip extend of the fault ruptures, the Magnitude – Area relationship of Wells & Coppersmith [63] can be applied. A complete rupture on the MBTCF in between the two earthquakes of 2015 leads to an M7.1 earthquake. With respect to the ± 0.25 uncertainty given by [63], this result matches with the estimated magnitude of the 1692 Esteco earthquake (see Section 1.2). Hence, it is possible to speculate that the intermediate magnitude earthquakes of September and October 2015 are aftershocks of the Esteco earthquake. This also would have implications for its probable epicenter location (see Figure 8.1).

In the scope of this study, it was not intended nor the time was available, to perform a complete probabilistic seismic hazard analysis. Thus, it was restricted to a qualitatively analysis only.

9 Conclusions

Although previously described as a broken-foreland type of deformation with spatiotemporal disparate deformation and sedimentation [196], the temporal installation of a seismological network in the Central Andean Foreland uncovers an elevated seismic activity confined along the Andean thrust front of the Santa-Bárbara-System.

The catalog of primary hypocenter locations, with a magnitude of completeness M_C 1.45, reveals event distribution along steep, deep reaching thrust faults, generated through the inversion of Cretaceous normal faults. Further, the seismic deformation propagates through the whole crust, portraying a subhorizontal, decollement-like structure close to the Moho.

The greater depth limitation of the brittle-ductile transition zone, in combination with the findings of the estimated local velocity models, implicates suggestions for the composition of the crust. This leads to opportunities for potential future research questions, aiming for modeling lower crustal boundary conditions, supporting the striking observations of this thesis.

Highly accurate event relocations enable the mapping of fault traces. In combination with source information derived from focal mechanisms, the geometry and the (stress orientation/deformation type) of seismogenic faults are discovered. Here, two new structures are speculated, in a location where field-based geological studies are unfeasible.

Following a wholistic path, the integration of geomorphic analyses [197] based on remote-sensing data, and observations from active [14] and passive [16] geophysical experiments grant the pervasive strengthening of scientific findings, in otherwise remote and inaccessible parts of the geosphere.

Acknowledgments

This research project was mainly funded by the German Research Council (*Deutsche Forschungsgemeinschaft*). I am very thankful to them for granting the International Research Training Group StRATEGy, where I was part of. Besides the general funds for salary, fieldwork and conferences, many opportunities were given to us, through soft skills training, preparing us for the future work as the next generation of scientists.

Many thanks to all the people of StRATEGy, involved at any level. Special thanks to Manfred Strecker and Magdalena Scheck-Wenderoth for leading the Graduate Colleg and to Frank Krüger, for giving me the opportunity to start the Doctorate position within this framework. With all members of StRATEGy, independent from their scientific background or if they were PIs or PhDs, I had many fruitful discussions and found myself always in a respectful environment. Here, I want to emphasize the personal connection I had to all my fellow PhD students, with plenty of international and intercultural exchanges we experienced together. These I will always keep in mind and hope to benefit from in the next levels of my career. The organisational skills of Henry Wichura, Melanie Olschmke, Andreas Bergner and Verónica Torres Acosta enabled and facilitated many additional opportunities, i.e., several research stays and field work surveys in Argentina.

Without the permission of the University of Potsdam, to use their seismological instruments and providing infrastructural support over the last four years, this study could not have been realized. Here, a special thank to Daniel Vollmer, who was always very helpful and supportive, while I carried out the field-based part of the study.

I will always be grateful to Frank Krüger. During the supervision of my thesis, he was always very supportive and constructively critical, while giving me enough freedom, in order to follow my own path of solving open research questions or applying different approaches. He was always available, giving wonderful advises and sharing a lot of empathy in all periods of my PhD. In addition I am thankful, that he supported an additional year of funding by the University of Potsdam, so I remained contracted and became the additional opportunity to teach in front of Bachelor students.

On the Argentinean side of the binational training group, I am especially grateful to Fernando Hongn and Patricia Alvarado, besides many other PIs in the Argentinean StRATEGy environment. Both were in key positions, when organizing the transportation of human and technical resources into the field. In addition, they were very supportive throughout my extensive research stays in Argentina, allowing me to assemble my own research network. From the many fellow Argentinean PhD students, I want to name three outstanding persons: Ahmad Arnous, Germán Aranda Viana and Emilio Criado Sutti. They played a major role in the realization of the fieldwork and the following joint research projects. In addition, I also admire the deep private friendship which arose from the originally professional relationship.

Outside of science I want to thank my parents first. Besides supporting my career, they also gave me many opportunities to discover my curiosity about mountain building processes at a very early age. My former partner Mira was always very supportive, from the first ideas to every opportunity which was offered to me throughout the PhD. At last, I am very thankful for my "learn-buddy" Mareike, with whom I share, besides a very deep friendship, all the struggles of working on a PhD thesis.

List of Figures

1.1	Nazca subduction profile	1
1.2	Overview maps of study area	3
1.3	stratigraphic coloumn	4
1.4	Map of historical and analog earthquake locations after Zossi 1979	7
1.5	Destruction of buildings in El Galpón	10
1.6	surface cracks in epicenter region	11
1.7	Abedeto results	13
2.1	station map of the STRATEGy network	17
2.2	image of station 04A	18
2.3	PPSD of station 06A	20
2.4	median PPSD of all stations	21
2.5	station-map, colorcoded by noise level	22
2.6	plot of available data throughout the STRATEGy installation	23
2.7	seismic instruments during huddle-test	25
2.8	results of huddle-test	27
3.1	workflow chart	29
3.2	delay and stack sketch	31
3.3	automatized event detections over time	35
3.4	pick accuracy	36
3.5	wadati diagram plots	38
3.6	complete Wadati diagram plots with uncorrected and corrected picks	39
3.7	corrected wadati diagram plots	41
4.1	broad map of events in catalog	45
4.2	map of events in catalog	47
4.3	location uncertainty	49
4.4	gutenberg-richter plot	50
4.5	magnitude distance plot	51
4.6	station magnitudes residuals	52
5.1	diffraction raypaths sketch	54
5.2	mantle velocity estimation histograms	55
5.3	reduced event map for VELEST	56
5.4	first velocity models	59
5.5	hypocenter stability plot	61

5.6	event separated model results	64
5.7	final local velocity model	66
5.8	VELEST relocated hypocenters	69
6.1	sketch of double-difference relocation	70
6.2	map and profiles of hypocenter relocations	74
7.1	Map with focal mechanisms	78
7.2	polar plots of strike and rake angles	79
8.1	seismotectonic maps	83
A.1	STRATEGy moment tensors	111
A.2	CRUST 1.0 model	112
A.3	1 km layer velocity models	113
A.4	reduced 5-layer models	114
A.5	velocity models from jackknife resampling of events	115
A.6	station jackknife resampling	116
A.7	station separated model results	116
A.8	station correction results per station	117
A.9	RMS errors	118
A.10	error ellipses over depth	119
A.11	depth uncertainty over depth	120

Bibliography

- [1] International Seismological Centre. *On-line Bulletin*. <http://www.isc.ac.uk>. Internatl. Seismol. Cent. Thatcham, United Kingdom, 2019.
- [2] Hiroo Kanamori and John J Cipar. “Focal process of the great Chilean earthquake May 22, 1960”. In: *Physics of the Earth and Planetary Interiors* 9.2 (1974), pp. 128–136.
- [3] Katsuyuki Abe and Hiroo Kanamori. “Magnitudes of great shallow earthquakes from 1953 to 1977”. In: *Tectonophysics* 62.3-4 (1980), pp. 191–203.
- [4] Muawia Barazangi and Bryan L Isacks. “Spatial distribution of earthquakes and subduction of the Nazca plate beneath South America”. In: *Geology* 4.11 (1976), pp. 686–692.
- [5] Teresa E Jordán et al. “Andean tectonics related to geometry of subducted Nazca plate”. In: *Geological Society of America Bulletin* 94.3 (1983), pp. 341–361.
- [6] J. Kley, C. R. Monaldi, and J. A. Salfity. “Along-strike segmentation of the Andean foreland: Causes and consequences”. In: *Tectonophysics* 301.1-2 (1999), pp. 75–94.
- [7] Thomas Cahill and Bryan L Isacks. “Seismicity and shape of the subducted Nazca plate”. In: *Journal of Geophysical Research: Solid Earth* 97.B12 (1992), pp. 17503–17529.
- [8] Michael Bevis and Bryan L Isacks. “Hypocentral trend surface analysis: Probing the geometry of Benioff zones”. In: *Journal of Geophysical Research: Solid Earth* 89.B7 (1984), pp. 6153–6170.
- [9] Kelly H Liu et al. “Mantle layering across central South America”. In: *Journal of Geophysical Research: Solid Earth* 108.B11 (2003).
- [10] Andres Tassara et al. “Three-dimensional density model of the Nazca plate and the Andean continental margin”. In: *Journal of Geophysical Research: Solid Earth* 111.B9 (2006).
- [11] Gavin P Hayes, David J Wald, and Rebecca L Johnson. “Slab1. 0: A three-dimensional model of global subduction zone geometries”. In: *Journal of Geophysical Research: Solid Earth* 117.B1 (2012).
- [12] Cliff Frohlich. *Deep earthquakes*. Cambridge university press, 2006.
- [13] M.R. Strecker et al. “Tectonics and Climate of the Southern Central Andes”. In: *Annual Review of Earth and Planetary Sciences* 35.1 (2007), pp. 747–787.

- [14] A. Arnous et al. “Neotectonic activity in the low-strain broken foreland (Santa Bárbara System) of the north-western Argentinean Andes, (26S)”. In: *Lithosphere* (2019). in review.
- [15] Thomas Cahill et al. “SEISMICITY AND TECTONICS IN JUJUY PROVINCE, NORTHWESTERN ARGENTINA”. In: *Tectonics* 11.5 (1992), pp. 944–959.
- [16] Martin Zeckra et al. *Seismic neTwoRk/Array in norThwEstern arGentina - STRAT-EGy*. Dataset/Seismic Network. 2017. DOI: 10.7914/SN/2S_2016.
- [17] Dean Whitman et al. “Attenuation of high-frequency seismic waves beneath the central Andean Plateau”. In: *Journal of Geophysical Research* 97.B13 (1992), p. 19929.
- [18] Brian K Horton. “Sedimentary record of Andean mountain building”. In: *Earth-Science Reviews* 178 (2018), pp. 279–309.
- [19] Phillip K. McFarland et al. “Rapid Geodetic Shortening Across the Eastern Cordillera of NW Argentina Observed by the Puna-Andes GPS Array”. In: *Journal of Geophysical Research: Solid Earth* 122.10 (2017), pp. 8600–8623.
- [20] Patricia Alvarado and Victor A Ramos. “Earthquake deformation in the north-western Sierras Pampeanas of Argentina based on seismic waveform modelling”. In: *Journal of Geodynamics* 51.4 (2011), pp. 205–218.
- [21] N Carrera et al. “The role of inversion tectonics in the structure of the Cordillera Oriental (NW Argentinean Andes)”. In: *Journal of Structural geology* 28.11 (2006), pp. 1921–1932.
- [22] Mathis P Hain et al. “Neogene to Quaternary broken foreland formation and sedimentation dynamics in the Andes of NW Argentina (25 S)”. In: *Tectonics* 30.2 (2011).
- [23] Víctor H García, Fernando Hongn, and Ernesto O Cristallini. “Late Miocene to recent morphotectonic evolution and potential seismic hazard of the northern Lerma valley: clues from Lomas de Medeiros, Cordillera Oriental, NW Argentina”. In: *Tectonophysics* 608 (2013), pp. 1238–1253.
- [24] Diego Nicolas Iaffa et al. “Basin fragmentation controlled by tectonic inversion and basement uplift in Sierras Pampeanas and Santa Bárbara System, northwest Argentina”. In: *Geological Society, London, Special Publications* 377.1 (2013), pp. 101–117.
- [25] Robbie Gries. “North-south compression of Rocky Mountain foreland structures”. In: (1983).
- [26] Stephen Marshak, Karl Karlstrom, and J Michael Timmons. “Inversion of Proterozoic extensional faults: An explanation for the pattern of Laramide and Ancestral Rockies intracratonic deformation, United States”. In: *Geology* 28.8 (2000), pp. 735–738.
- [27] VS Burtman. “Structural geology of variscan Tien Shan, USSR”. In: *Am. J. Sci* 275 (1975), pp. 157–186.

- [28] DW Burbank et al. “Partitioning of intermontane basins by thrust-related folding, Tien Shan, Kyrgyzstan”. In: *Basin Research* 11.1 (1999), pp. 75–92.
- [29] Victor A Ramos, EO Cristallini, and Daniel J Pérez. “The Pampean flat-slab of the Central Andes”. In: *Journal of South American earth sciences* 15.1 (2002), pp. 59–78.
- [30] R Mon and JA Salfity. “Tectonic evolution of the Andes of northern Argentina”. In: (1995).
- [31] Félix González Bonorino. “Algunos problemas geológicos de las Sierras Pampeanas”. In: *Revista de la Asociación Geológica Argentina* 5.3 (1950), pp. 81–110.
- [32] Richard W Allmendinger et al. “Paleogeography and Andean structural geometry, northwest Argentina”. In: *Tectonics* 2.1 (1983), pp. 1–16.
- [33] L del V Abascal. “Deformación andina en la cuenca de Choromoro, NO de Tucumán: estilo estructural combinado”. In: *Revista de la Asociación Geológica Argentina* 60.2 (2005), pp. 268–277.
- [34] Jonas Kley and César R. Monaldi. “Tectonic inversion in the Santa Barbara System of the central Andean foreland thrust belt, northwestern Argentina”. In: 21.6 (2002), pp. 1–18.
- [35] Ricardo Mon. “The structure of the eastern border of the Andes in north-western Argentina”. In: *Geologische Rundschau* 65.1 (1976), pp. 211–222.
- [36] George E Hilley and Manfred R Strecker. “Processes of oscillatory basin filling and excavation in a tectonically active orogen: Quebrada del Toro Basin, NW Argentina”. In: *Geological Society of America Bulletin* 117.7-8 (2005), pp. 887–901.
- [37] Victor A Ramos, Ricardo N Alonso, and Manfred Strecker. “Estructura y neotectónica de Las Lomas de Olmedo, zona de transición entre los Sistemas Subandino y de Santa Bárbara, provincia de Salta”. In: *Revista de la Asociación Geológica Argentina* 61.4 (2006), pp. 579–588.
- [38] Diego Nicolas Iaffa et al. “The role of inherited structures in a foreland basin evolution. The Metán Basin in NW Argentina”. In: *Journal of Structural Geology* 33.12 (2011), pp. 1816–1828.
- [39] H. Barcelona et al. “Tectonic activity revealed by morphostructural analysis: Development of the Sierra de la Candelaria range, northwestern Argentina”. In: *Journal of South American Earth Sciences* 56 (2014), pp. 376–395.
- [40] Rosa A Marquillas, Cecilia Del Papa, and Ignacio F Sabino. “Sedimentary aspects and paleoenvironmental evolution of a rift basin: Salta Group (Cretaceous–Paleogene), northwestern Argentina”. In: *International Journal of Earth Sciences* 94.1 (2005), pp. 94–113.

- [41] Chiara Invernizzi et al. “Preliminary assessment of the geothermal potential of Rosario de la Frontera area (Salta, NW Argentina): insight from hydro-geological, hydro-geochemical and structural investigations”. In: *Journal of South American Earth Sciences* 54 (2014), pp. 20–36.
- [42] E Cristallini, AH Cominguez, and VA Ramos. “Deep structure of the Metan-Guachipas region: Tectonic inversion in northwestern Argentina”. In: *Journal of South American Earth Sciences* 10.5-6 (1997), pp. 403–421.
- [43] JA Salfity and RA Marquillas. “Tectonic and sedimentary evolution of the Cretaceous-Eocene Salta Group basin, Argentina”. In: *Cretaceous tectonics of the Andes*. Springer, 1994, pp. 266–315.
- [44] JH Reynolds et al. “Middle Miocene tectonic development of the transition zone, Salta Province, northwest Argentina: Magnetic stratigraphy from the Metán Subgroup, Sierra de González”. In: *Geological Society of America Bulletin* 112.11 (2000), pp. 1736–1751.
- [45] Ricardo Mon and Adolfo a. Gutiérrez. “Estructura del extremo sur del sistema subandino (provincias de Salta, Santiago del Estero y Tucumán)”. In: *Revista de la Asociación Geológica Argentina* 62.1 (2007), pp. 62–68.
- [46] Manfred R Strecker et al. “Does the topographic distribution of the central Andean Puna Plateau result from climatic or geodynamic processes?” In: *Geology* 37.7 (2009), pp. 643–646.
- [47] Benjamin A Brooks et al. “Orogenic-wedge deformation and potential for great earthquakes in the central Andean backarc”. In: *Nature Geoscience* 4.6 (2011), p. 380.
- [48] Gerardo E Bossi. *Geología y estratigrafía del sector sur del Valle de Choromoro*. Universidad Nacional de Tucumán, Fundación e Instituto Miguel Lillo, 1969.
- [49] Victor A Ramos. “The basement of the Central Andes: the Arequipa and related terranes”. In: *Annu. Rev. Earth Planet. Sci.* 36 (2008), pp. 289–324.
- [50] C Moreno Espelta, JG Viramonte, and JE Arias. “Area termal de Rosario de la Frontera y sus posibilidades”. In: *Actas del II Congreso Ibero-Americano de Geología Económica IV*. 1975, pp. 543–548.
- [51] R Seggiaro et al. “Estructura del area geotermica de Rosario de la Frontera, Salta, Argentina”. In: *VIII Congreso Geológico Chileno*. Vol. 1. 1997, pp. 390–394.
- [52] JCM Turner et al. “Estratigrafía del cordón de Escaya y de la sierra de Rinconada (Jujuy)”. In: *Revista de la Asociación Geológica Argentina* 13.1-2 (1959), pp. 15–39.
- [53] FÉLIX CELSO Reyes and JA Salfity. “Consideraciones sobre la estratigrafía del Cretácico (Subgrupo Pirgua) del noroeste argentino”. In: *V Congreso Geológico Argentino: Buenos Aires, Argentina, Asociación Geológica Argentina*. 1973, pp. 355–385.

- [54] JG Viramonte et al. “Cretaceous rift related magmatism in central-western South America”. In: *Journal of South American Earth Sciences* 12.2 (1999), pp. 109–121.
- [55] JA Gebhard, AR Giudici, and J Oliver Gascón. “Geología de la comarca entre el Río Juramento y arroyo Las Tortugas, provincias de Salta y Jujuy, Republica Argentina”. In: *Revista de la Asociación Geológica Argentina* 29.3 (1974), pp. 359–375.
- [56] JA Salfity and CR Monaldi. *Hoja Geológica 2566-IV: Metán (provincia de Salta)*. 2006.
- [57] A. Gioncada et al. “Pliocene intraplate-type volcanism in the Andean foreland at 26°10’S, 64°40’W (NW Argentina): Implications for magmatic and structural evolution of the Central Andes”. In: *Lithosphere* 2.3 (2010), pp. 153–171.
- [58] S Zapata et al. “Miocene fragmentation of the Central Andean foreland basins between 26 and 28°S”. In: *Journal of South American Earth Sciences* (2019), p. 102238.
- [59] Ricardo Mon et al. “Estructura del Cerro Colorado (Sistema de Santa Bárbara, provincia de Salta)”. In: *Asociación Geológica Argentina Serie D.Publicación Especial No. 6* (2006), pp. 113–118.
- [60] JA Salfity. “Evolución paleogeográfica del Grupo Salta (Cretácico-Eogénico), Argentina”. In: *Actas Congreso Latinoamericano de Geología*. Vol. 5. 1982, pp. 11–26.
- [61] Marta María Zossi. “Estudio de la actividad sísmica de la Provincia de Tucumán”. Doctoral Thesis. Universidad Nacional de Tucumán, 1979, pp. 1–125.
- [62] Carlos A. Navarro. *Sismicidad Histórica de la R.A.* Tech. rep. INPRES, 2012.
- [63] Donald L Wells and Kevin J Coppersmith. “New empirical relationships among magnitude, rupture length, rupture width, rupture area, and surface displacement”. In: *Bulletin of the seismological Society of America* 84.4 (1994), pp. 974–1002.
- [64] Lilian Blaser et al. “Scaling relations of earthquake source parameter estimates with special focus on subduction environment”. In: *Bulletin of the Seismological Society of America* 100.6 (2010), pp. 2914–2926.
- [65] Klaus-G. Hinzen. “The use of engineering seismological models to interpret archaeoseismological findings in Tolbiacum, Germany: a case study”. In: *Bulletin of the Seismological Society of America* 95.2 (2005), pp. 521–539.
- [66] Fabrizio Galadini, Klaus-G. Hinzen, and Stathis Stiros. “Archaeoseismology: Methodological issues and procedure”. In: *Journal of Seismology* 10.4 (2006), pp. 395–414.
- [67] Klaus-G. Hinzen et al. “Quantitative methods in archaeoseismology”. In: *Quaternary International* 242.1 (2011), pp. 31–41.

- [68] Gregor Schweppe et al. “The ruin of the Roman Temple of Kedesh, Israel; example of a precariously balanced archaeological structure used as a seismoscope”. In: *Annals of Geophysics* 60.4 (2017).
- [69] INPRES and INTI CIRSOC. *Reglamento Argentino Para Construcciones Sismorresistentes – Parte I, Construcciones en General*. Tech. rep. Instituto Nacional de Tecnología Industrial, 2013.
- [70] Abel Pesce and Fernando Miranda. *Catalogo de Manifestaciones Termales*. Tech. rep. Buenos Aires: SEGEMAR - Servicio Geológico Minero Argentino, 2003, pp. 1–165. URL: <http://repositorio.segemar.gov.ar/308849217/2424>.
- [71] R. A. Sloan et al. “Earthquake depth distributions in central Asia, and their relations with lithosphere thickness, shortening and extension”. In: *Geophysical Journal International* 185.1 (2011), pp. 1–29.
- [72] Alireza Alinaghi and Frank Krüger. “Seismic array analysis and redetermination of depths of earthquakes in Tien-Shan: implications for strength of the crust and lithosphere”. In: *Geophysical Journal International* 198.2 (2014), pp. 1111–1129.
- [73] Torsten Dahm et al. “The 2004 M w 4.4 Rotenburg, Northern Germany, earthquake and its possible relationship with gas recovery”. In: *Bulletin of the Seismological Society of America* 97.3 (2007), pp. 691–704.
- [74] J. Schweitzer et al. “Seismic Arrays”. In: *New Manual of Seismological Observatory Practice 2 (NMSOP2)*. Ed. by P. Bormann. 2nd ed. Deutsches GeoForschungsZentrum GFZ, 2012. Chap. 9, pp. 1–80. DOI: http://doi.org/10.2312/GFZ.NMSOP-2_ch9.
- [75] Sebastian Rost and Christine Thomas. “Improving seismic resolution through array processing techniques”. In: *Surveys in Geophysics* 30.4-5 (2009), pp. 271–299.
- [76] Sebastian Heimann et al. *Pyrocko - An open-source seismology toolbox and library*. GFZ Data Services, 2017. DOI: <http://doi.org/10.5880/GFZ.2.1.2017.001>.
- [77] GSC. *Earthquakes Canada*. NetDC Service. <http://earthquakescanada.nrcan.gc.ca/stndon/NetDC/index.php>. Nat. Res. Can., 2019.
- [78] GEOFON Data Centre. *GEOFON Seismic Network*. Other/Seismic Network. 1993. DOI: 10.14470/TR560404.
- [79] Federal Institute for Geosciences and Natural Resources (BGR). *German Regional Seismic Network (GRSN)*. Dataset/Seismic Network. Federal Institute for Geosciences and Natural Resources (BGR), 1976. DOI: <https://doi.org/10.25928/MBX6-HR74>.
- [80] Rongjiang Wang. “A simple orthonormalization method for stable and efficient computation of Green’s functions”. In: *Bulletin of the Seismological Society of America* 89.3 (1999), pp. 733–741.

- [81] Brian LN Kennett, ER Engdahl, and R Buland. “Constraints on seismic velocities in the Earth from traveltimes”. In: *Geophysical Journal International* 122.1 (1995), pp. 108–124.
- [82] C. Bassin, G. Laske, and G. Masters. “The Current Limits of Resolution for Surface Wave Tomography in North America”. In: *EOS Trans AGU* 81 (2000).
- [83] Walter D Mooney, Gabi Laske, and T Guy Masters. “CRUST 5.1: A global crustal model at 5×5 ”. In: *Journal of Geophysical Research: Solid Earth* 103.B1 (1998), pp. 727–747.
- [84] G. Sanchez et al. “The Argentinean National Network of Seismic and Strong-Motion Stations”. In: *Seismological Research Letters* 84.5 (2013), pp. 729–736.
- [85] Servicio Geológico Minero Argentino. *Deformaciones Cuaternarias*. map. SEGEMAR, Oct. 2017.
- [86] Victor A Ramos. “Las provincias geológicas del territorio argentino”. In: *Geología Argentina* 29.3 (1999), pp. 41–96.
- [87] T. Utsu and Y. Ogata. “The centenary of the Omori formula for a decay law of aftershock activity.” In: *Journal of Physics of the Earth* 43.1 (1995), pp. 1–33.
- [88] Daniel E McNamara and Raymond P Buland. “Ambient noise levels in the continental United States”. In: *Bulletin of the seismological society of America* 94.4 (2004), pp. 1517–1527.
- [89] Jon Peterson et al. “Observations and modeling of seismic background noise”. In: (1993).
- [90] Moritz Beyreuther et al. “ObsPy: A Python toolbox for seismology”. In: *Seismological Research Letters* 81.3 (2010), pp. 530–533.
- [91] Michael Selwyn Longuet-Higgins. “A theory of the origin of microseisms”. In: *Philosophical Transactions of the Royal Society of London. Series A, Mathematical and Physical Sciences* 243.857 (1950), pp. 1–35.
- [92] Gregor Hillers et al. “Global oceanic microseism sources as seen by seismic arrays and predicted by wave action models”. In: *Geochemistry, Geophysics, Geosystems* 13.1 (2012).
- [93] P. Bormann and E. Wielandt. “Seismic Signals and Noise”. In: *New Manual of Seismological Observatory Practice 2 (NMSOP2)*. Ed. by P. Bormann. 2nd ed. Deutsches GeoForschungsZentrum GFZ, 2013. Chap. 04, pp. 1–62. DOI: http://doi.org/10.2312/GFZ.NMSOP-2_ch4.
- [94] Gregoire Francois Gauthier, Robin C. Carruthers, and Maria Florencia Millan Placci. *Logística de la soja : Argentina - Paraguay - Uruguay (Spanish)*. Tech. rep. Washington D.C.: World Bank Group, 2016. URL: <http://documents.worldbank.org/curated/en/923401468272770160/Logística-de-la-soja-Argentina-Paraguay-Uruguay>.

- [95] Maryam Ramezani Ziarani et al. “Using Convective Available Potential Energy (CAPE) and Dew-Point Temperature to Characterize Rainfall-Extreme Events in the South-Central Andes”. In: *Atmosphere* 10.7 (2019), p. 379.
- [96] SISTEMA DE INFORMACIÓN Y GESTIÓN AGROMETEOROLÓGICA. *Estación Meteorológica Automática*. Meteorological Station. INTA – Instituto Nacional de Tecnología Agropecuaria, 2017.
- [97] Jens Havskov and Gerardo Alguacil. *Instrumentation in earthquake seismology*. Vol. 358. Springer, 2004.
- [98] The ObsPy Development Team. *ObsPy 1.1.1*. Feb. 2019. DOI: 10.5281/zenodo.1040770. URL: <https://doi.org/10.5281/zenodo.1040770>.
- [99] Carl E Johnson et al. “Earthworm: A flexible approach to seismic network processing”. In: *Iris newsletter* 14.2 (1995), pp. 1–4.
- [100] Jens Havskov and Lars Ottemoller. “SEISAN earthquake analysis software”. In: *Seismological Research Letters* 70.5 (1999), pp. 532–534.
- [101] B Weber et al. “SeisComp3—Automatic and interactive real time data processing”. In: *Geophysical Research Abstracts*. Vol. 9. 09,219. 2007.
- [102] W Hanka et al. “Real-time earthquake monitoring for tsunami warning in the Indian Ocean and beyond.” In: *Natural Hazards & Earth System Sciences* 10.12 (2010).
- [103] Egill Hauksson, Wenzheng Yang, and Peter M Shearer. “Waveform relocated earthquake catalog for southern California (1981 to June 2011)”. In: *Bulletin of the Seismological Society of America* 102.5 (2012), pp. 2239–2244.
- [104] J Arthur Snoke. “FOCMEC: Focal mechanism determinations”. In: *International Handbook of Earthquake and Engineering Seismology* 85 (2003), pp. 1629–1630.
- [105] Simone Cesca and Sebastian Heimann. “A practical on moment tensor inversion using the Kiwi tools”. In: *New Manual of Seismological Observatory Practice (NMSOP)* 2 (2013), pp. 1–24.
- [106] Lion Krischer et al. “Large-scale seismic inversion framework”. In: *Seismological Research Letters* 86.4 (2015), pp. 1198–1207.
- [107] Raphaël Grandin et al. “Rupture process of the Mw= 7.9 2015 Gorkha earthquake (Nepal): Insights into Himalayan megathrust segmentation”. In: *Geophysical Research Letters* 42.20 (2015), pp. 8373–8382.
- [108] Henriette Sudhaus et al. “New Developments in Open-source Tools to Combine Geodetic Data and Seismic Waveforms”. In: *EGU General Assembly Conference Abstracts*. Vol. 20. 2018, p. 14592.
- [109] Andreas Steinberg et al. “Automated assessment of rupture geometry and segmentation based on InSAR data and seismic moment rate functions prior to source optimizations”. In: *EGU General Assembly Conference Abstracts*. Vol. 20. 2018, p. 15647.

- [110] Weiqiang Zhu and Gregory C Beroza. “PhaseNet: a deep-neural-network-based seismic arrival-time picking method”. In: *Geophysical Journal International* 216.1 (2018), pp. 261–273.
- [111] Marius Kriegerowski et al. “A deep convolutional neural network for localization of clustered earthquakes based on multistation full waveforms”. In: *Seismological Research Letters* 90.2A (2018), pp. 510–516.
- [112] Zachary E Ross et al. “Generalized seismic phase detection with deep learning”. In: *Bulletin of the Seismological Society of America* 108.5A (2018), pp. 2894–2901.
- [113] DJ Pugh and Robert Stephen White. “MTfit: A Bayesian approach to seismic moment tensor inversion”. In: *Seismological Research Letters* 89.4 (2018), pp. 1507–1513.
- [114] Johannes Schweitzer. *HYPOSAT - A new routine to locate seismic events*. Tech. rep. 1. 1997.
- [115] FDSN. *SEED Reference Manual*. Tech. rep. Aug. 2012.
- [116] Danijel Schorlemmer et al. “QuakeML: status of the XML-based seismological data exchange format”. In: *Annals of Geophysics* 54.1 (2011), pp. 59–65. DOI: 10.4401/ag-4874.
- [117] Danijel Schorlemmer et al. *QuakeML—An XML Representation of Seismological Data Basic Event Description*. Tech. rep. Version 1.2. ETH Zurich. URL: <http://quakeml.org/docs/latest?action=AttachFile&do=get&target=QuakeML-BED.pdf>.
- [118] Dmitry Bobrov, Ivan Kitov, and Lassina Zerbo. “Perspectives of cross-correlation in seismic monitoring at the international data centre”. In: *Pure and Applied Geophysics* 171.3-5 (2014), pp. 439–468.
- [119] David R Shelly, Gregory C Beroza, and Satoshi Ide. “Non-volcanic tremor and low-frequency earthquake swarms”. In: *Nature* 446.7133 (2007), p. 305.
- [120] Matthias Ohrnberger. “Continuous automatic classification of seismic signals of volcanic origin at Mt. Merapi, Java, Indonesia”. PhD thesis. University of Potsdam, 2001, p. 168.
- [121] Moritz Beyreuther et al. “Constructing a Hidden Markov Model based earthquake detector: application to induced seismicity”. In: *Geophysical Journal International* 189.1 (Apr. 2012), pp. 602–610.
- [122] Martin Zeckra et al. “Automated Detection and Classification of Rockfall Induced Seismic Signals with Hidden-Markov-Models”. In: *AGU Fall Meeting Abstracts*. 2015.
- [123] Arnaud Burtin et al. “Continuous catchment-scale monitoring of geomorphic processes with a 2-D seismological array”. In: *Journal of Geophysical Research: Earth Surface* 118.3 (2013), pp. 1956–1974.

- [124] A. Burtin et al. “Spectral analysis of seismic noise induced by rivers: A new tool to monitor spatiotemporal changes in stream hydrodynamics”. In: *Journal of Geophysical Research: Solid Earth* 113.B5 (2008).
- [125] Julian Drew et al. “Coalescence microseismic mapping”. In: *Geophysical Journal International* 195.3 (2013), pp. 1773–1785.
- [126] Nadège Langet et al. “Continuous Kurtosis-Based Migration for Seismic Event Detection and Location, with Application to Piton de la Fournaise Volcano, La RéunionContinuous Kurtosis-Based Migration for Seismic Event Detection and Location”. In: *Bulletin of the Seismological Society of America* 104.1 (2014), pp. 229–246.
- [127] Clément Hibert et al. “Automated identification, location, and volume estimation of rockfalls at Piton de la Fournaise volcano”. In: *Journal of Geophysical Research: Earth Surface* 119.5 (2014), pp. 1082–1105.
- [128] Francesco Grigoli et al. “Automated seismic event location by travel-time stacking: An application to mining induced seismicity”. In: *Seismological Research Letters* 84.4 (2013), pp. 666–677.
- [129] José Ángel et al. “Automated Full Waveform Detection and Location Algorithm of Acoustic Emissions from Hydraulic Fracturing Experiment”. In: *Procedia Engineering* 191 (2017), pp. 697–702.
- [130] Simone Cesca and Francesco Grigoli. “Full waveform seismological advances for microseismic monitoring”. In: *Advances in Geophysics* 56 (Nov. 2014).
- [131] Honn Kao and Shao-Ju Shan. “The source-scanning algorithm: Mapping the distribution of seismic sources in time and space”. In: *Geophysical Journal International* 157.2 (2004), pp. 589–594.
- [132] Honn Kao and Shao-Ju Shan. “Rapid identification of earthquake rupture plane using source-scanning algorithm”. In: *Geophysical Journal International* 168.3 (2007), pp. 1011–1020.
- [133] Hom Nath Gharti et al. “Automated microearthquake location using envelope stacking and robust global optimizationautomated microearthquake location”. In: *Geophysics* 75.4 (2010), MA27–MA46.
- [134] Yen-Che Liao et al. “Delineating complex spatiotemporal distribution of earthquake aftershocks: An improved source-scanning algorithm”. In: *Geophysical Journal International* 189.3 (2012), pp. 1753–1770.
- [135] Xiangfang Zeng et al. “Surface microseismic monitoring of hydraulic fracturing of a shale-gas reservoir using short-period and broadband seismic sensors”. In: *Seismological Research Letters* 85.3 (2014), pp. 668–677.
- [136] Francesco Grigoli et al. “Automated seismic event location by waveform coherence analysis”. In: *Geophys. J. Int* 196 (2014), pp. 1742–1753.

- [137] S Heimann et al. “Lassie: A versatile tool to detect and locate seismic activity”. interested users to preview Lassie can write to: sebastian.heimann@gfz-potsdam.de. 2018.
- [138] S Husen et al. “Probabilistic earthquake location in complex three-dimensional velocity models: Application to Switzerland”. In: *Journal of Geophysical Research: Solid Earth* 108.B2 (2003).
- [139] Rex V Allen. “Automatic earthquake recognition and timing from single traces”. In: *Bulletin of the Seismological Society of America* 68.5 (1978), pp. 1521–1532.
- [140] Rex V Allen. “Automatic phase pickers: Their present use and future prospects”. In: *Bulletin of the Seismological Society of America* 72.6B (1982), S225–S242.
- [141] Christos D Saragiotis, Leontios J Hadjileontiadis, and Stavros M Panas. “PAI-S/K: A robust automatic seismic P phase arrival identification scheme”. In: *IEEE Transactions on Geoscience and Remote Sensing* 40.6 (2002), pp. 1395–1404.
- [142] L Küperkoch et al. “Automated P-wave arrival time determination using higher order statistics”. In: *Geophys. J. Int* 181.2 (2010), pp. 1159–1170.
- [143] M. Baer and U. Kradolfer. “An automatic phase picker for local and teleseismic events”. In: *Bulletin of the Seismological Society of America* 77.4 (1987), pp. 1437–1445.
- [144] Takashi Akazawa. “A technique for automatic detection of onset time of P-and S-phases in strong motion records”. In: *Proc. of the 13th World Conf. on Earthquake Engineering*. 2004.
- [145] L. Küperkoch, T. Meier, and T. Diehl. “Automated Event and Phase Identification”. In: *New Manual of Seismological Observatory Practice 2 (NMSOP2)*. Ed. by P. Bormann. 2nd ed. Deutsches GeoForschungsZentrum GFZ, 2013. Chap. 16, pp. 1–52. DOI: http://doi.org/10.2312/GFZ.NMSOP-2_ch16.
- [146] N. Poiata et al. “Multi-band array detection and location of seismic sources recorded by dense seismic networks”. In: *Geophys. J. Int.* 205.3 (2016), pp. 1548–1573.
- [147] K. Wadati and S. Oki. “On the travel time of earthquake waves (Part II)”. In: *Journal of the Meteorological Society of Japan*. 2nd ser. 11.1 (1933), pp. 14–28.
- [148] J. Havskov, P. Bormann, and J. Schweitzer. “Seismic source location”. In: *New Manual of Seismological Observatory Practice 2 (NMSOP2)*. Ed. by P. Bormann. 2nd ed. Deutsches GeoForschungsZentrum GFZ, 2012. Chap. IS 10.1, pp. 1–36. DOI: http://doi.org/10.2312/GFZ.NMSOP-2_IS_10.1.
- [149] Travis E. Oliphant. *A guide to NumPy*. Vol. 1. Trelgol Publishing USA, 2006.
- [150] Gabi Laske et al. “Update on CRUST1. 0—A 1-degree global model of Earth’s crust”. In: *Geophys. Res. Abstr.* Vol. 15. EGU General Assembly Vienna, Austria. 2013, p. 2658.
- [151] Charles F. Richter. “An instrumental earthquake magnitude scale”. In: *Bulletin of the Seismological Society of America* 25.1 (1935), pp. 1–32.

- [152] Beno Gutenberg and Charles Francis Richter. “Earthquake magnitude, intensity, energy, and acceleration”. In: *Bulletin of the Seismological Society of America* 32.3 (1942), pp. 163–191.
- [153] Beno Gutenberg and Charles F. Richter. “Earthquake magnitude, intensity, energy, and acceleration: (Second paper)”. In: *Bulletin of the seismological society of America* 46.2 (1956), pp. 105–145.
- [154] P. Bormann and D. Wendt S.and DiGiacomo. “Seismic Sources and Source Parameters”. In: *New Manual of Seismological Observatory Practice 2 (NMSOP2)*. Ed. by P. Bormann. 2nd ed. Deutsches GeoForschungsZentrum GFZ, 2013. Chap. 03, pp. 1–259. DOI: http://doi.org/10.2312/GFZ.NMSOP-2_ch3.
- [155] LK Hutton and David M Boore. “The ML scale in southern California”. In: *Bulletin of the Seismological Society of America* 77.6 (1987), pp. 2074–2094.
- [156] G. Sanchez et al. “The Argentinean National Network of Seismic and Strong-Motion Stations”. In: *Seismological Research Letters* 84.5 (2013), pp. 729–736.
- [157] B Schurr et al. “Seismicity and average velocities beneath the Argentine Puna plateau”. In: *Geophysical Research Letters* 26.19 (1999), pp. 3025–3028.
- [158] Konstantinos Michailos et al. “Variations in Seismogenic Thickness Along the Central Alpine Fault, New Zealand, Revealed by a Decade’s Relocated Microseismicity”. In: *Geochemistry, Geophysics, Geosystems* (2019).
- [159] G Monsalve et al. “Seismicity and one-dimensional velocity structure of the Himalayan collision zone: Earthquakes in the crust and upper mantle”. In: *Journal of Geophysical Research: Solid Earth* 111.B10 (2006).
- [160] Nihal Akyol et al. “Crustal structure and local seismicity in western Anatolia”. In: *Geophysical Journal International* 166.3 (2006), pp. 1259–1269.
- [161] PA Reasenberg and LM Jones. “Earthquake hazard after a mainshock in California”. In: *Science* 243 (1989), pp. 73–76. URL: <http://www.sciencemag.org/content/243/4895/1173.short>.
- [162] T Van Stiphout, J Zhuang, and D Marsan. *Seismicity declustering, Community Online Resource for Statistical Seismicity Analysis*. 2012. DOI: 10.5078/corssa-52382934.
- [163] Jochen Woessner and Stefan Wiemer. “Assessing the quality of earthquake catalogues: Estimating the magnitude of completeness and its uncertainty”. In: *Bulletin of the Seismological Society of America* 95.2 (2005), pp. 684–698.
- [164] Jim Mori and Rachel E Abercrombie. “Depth dependence of earthquake frequency-magnitude distributions in California: Implications for rupture initiation”. In: *Journal of Geophysical Research: Solid Earth* 102.B7 (1997), pp. 15081–15090.
- [165] David Amitrano. “Brittle-ductile transition and associated seismicity: Experimental and numerical studies and relationship with the b value”. In: *Journal of Geophysical Research: Solid Earth* 108.B1 (2003).

- [166] E Kissling, U Kradolfer, and H Maurer. “Program VELEST user’s guide-Short Introduction”. In: *Institute of Geophysics, ETH Zurich* (1995).
- [167] Edi Kissling. “Geotomography with local earthquake data”. In: *Reviews of Geophysics* 26.4 (1988), pp. 659–698.
- [168] Edi Kissling et al. “Initial reference models in local earthquake tomography”. In: *Journal of Geophysical Research: Solid Earth* 99.B10 (1994), pp. 19635–19646.
- [169] Gary S. Chulick, Shane Detweiler, and Walter D. Mooney. “Seismic structure of the crust and uppermost mantle of South America and surrounding oceanic basins”. In: *Journal of South American Earth Sciences* 42.November 2017 (2013), pp. 260–276.
- [170] Marcelo Assumpção et al. “Models of crustal thickness for South America from seismic refraction, receiver functions and surface wave tomography”. In: *Tectonophysics* 609 (2013), pp. 82–96.
- [171] Myung W Lee. *Velocity ratio and its application to predicting velocities*.
- [172] Nikolas I. Christensen and Walter D. Mooney. “Seismic Velocity Structure and Composition of the Continental Crust: A global view”. In: *Journal of Geophysical Research* 100.B7 (1995), pp. 9761–9788.
- [173] F. Ibarra et al. “3D data-derived lithospheric structure of the Central Andes and its implications for deformation: Insights from gravity and geodynamic modelling”. In: *Tectonophysics* 766.February (2019), pp. 453–468.
- [174] Nikolas I. Christensen. “Poisson’s ratio and crustal seismology”. In: *Journal of Geophysical Research: Solid Earth* 101.B2 (1996), pp. 3139–3156.
- [175] BLN Kennett and ER Engdahl. “Traveltimes for global earthquake location and phase identification”. In: *Geophysical Journal International* 105.2 (1991), pp. 429–465.
- [176] F. Waldhauser and W. L. Ellsworth. “A Double-difference Earthquake location algorithm: Method and application to the Northern Hayward Fault, California”. In: *Bulletin of the Seismological Society of America* 90.6 (2000), pp. 1353–1368.
- [177] Felix Waldhauser. *hypoDD—A program to compute double-difference hypocenter locations*. Tech. rep. U.S. Geological Survey, 2001.
- [178] Oliver Heidbach et al. “Global crustal stress pattern based on the World Stress Map database release 2008”. In: *Tectonophysics* 482.1-4 (2010), pp. 3–15.
- [179] Sebastian Heimann et al. “A Python framework for efficient use of pre-computed Green’s functions in seismological and other physical forward and inverse source problems”. In: *Solid Earth Discussions* (2019). in review. DOI: <https://doi.org/10.5194/se-2019-85>.
- [180] Paul A Reasenber. “FPFIT, FPLOT, and FPPAGE: Fortran computer programs for calculating and displaying earthquake fault-plane solutions”. In: *US Geol. Surv. Open-File Rep.* (1985), pp. 85–739.

- [181] Jeanne L Hardebeck and Peter M Shearer. “A new method for determining first-motion focal mechanisms”. In: *Bulletin of the Seismological Society of America* 92.6 (2002), pp. 2264–2276.
- [182] D. J. Pugh, R. S. White, and P. A.F. Christie. “A Bayesian method for microseismic source inversion”. In: *Geophysical Journal International* 206.2 (2016), pp. 1009–1038.
- [183] CH Chapman and WS Leaney. “A new moment-tensor decomposition for seismic events in anisotropic media”. In: *Geophysical Journal International* 188.1 (2012), pp. 343–370.
- [184] Thomas Bayes. “LII. An essay towards solving a problem in the doctrine of chances. By the late Rev. Mr. Bayes, FRS communicated by Mr. Price, in a letter to John Canton, AMFR S”. In: *Philosophical transactions of the Royal Society of London* 53 (1763), pp. 370–418.
- [185] Devinderjit Sivia and John Skilling. *Data analysis: a Bayesian tutorial*. OUP Oxford, 2006.
- [186] DR Brillinger, A Udias, and BA Bolt. “A probability model for regional focal mechanism solutions”. In: *Bulletin of the Seismological Society of America* 70.1 (1980), pp. 149–170.
- [187] David Walsh, Richard Arnold, and John Townend. “A Bayesian approach to determining and parametrizing earthquake focal mechanisms”. In: *Geophysical Journal International* 176.1 (2009), pp. 235–255.
- [188] Mónica P Escayola, Cees R van Staal, and William J Davis. “The age and tectonic setting of the Puncoviscana Formation in northwestern Argentina: An accretionary complex related to Early Cambrian closure of the Puncoviscana Ocean and accretion of the Arequipa-Antofalla block”. In: *Journal of South American Earth Sciences* 32.4 (2011), pp. 438–459.
- [189] H. Kern. “Effect of high-low quartz transition on compressional and shear wave velocities in rocks under high pressure”. In: *Physics and Chemistry of Minerals* 4.2 (1979), pp. 161–171.
- [190] Walter D Mooney and Avihu Ginzburg. “Seismic measurements of the internal properties of fault zones”. In: *pure and applied geophysics* 124.1-2 (1986), pp. 141–157.
- [191] JN Wang et al. “Newtonian dislocation creep in quartzites: Implications for the rheology of the lower crust”. In: *Science* 265.5176 (1994), pp. 1204–1206.
- [192] Emily J Chin et al. “On the origin of hot metasedimentary quartzites in the lower crust of continental arcs”. In: *Earth and Planetary Science Letters* 361 (2013), pp. 120–133.
- [193] Peter Molnar and Wang-Ping Chen. “Seismicity and mountain building”. In: *Mountain building processes* (1982), pp. 41–57.

- [194] CR Monaldi and J Kley. “Balanced cross sections of the northern Santa Barbara system and Sierra de Zapla, Northwestern Argentina”. In: *VIII Congreso Geológico Chileno, Antofagasta, Chile*. Universidad Católica del Norte Antofagasta, Chile. 1997, pp. 180–184.
- [195] Zachary E Ross et al. “Hierarchical interlocked orthogonal faulting in the 2019 Ridgecrest earthquake sequence”. In: *Science* 366.6463 (2019), pp. 346–351.
- [196] Manfred R Strecker et al. “Structural, geomorphic, and depositional characteristics of contiguous and broken foreland basins: examples from the eastern flanks of the central Andes in Bolivia and NW Argentina”. In: *Tectonics of sedimentary basins: Recent advances* (2011), pp. 508–521.
- [197] Sean D Willett, Scott W McCoy, and Helen W Beeson. “Transience of the North American High Plains landscape and its impact on surface water”. In: *Nature* 561.7724 (2018), p. 528.

A Appendix

A.1 Wadati-Diagram

A.1.1 Derivation for source time independent v_P/v_S ratio estimation

After Wadati, 1933 [147]:

$$t_S - t_P = \left(\frac{v_P}{v_S} - 1\right)(t_P - t_0) \quad (\text{A.1})$$

$$\begin{aligned} t_{S-P} &= m_{Wad}(t_P - t_0) \\ t_0 &= t_P - \frac{t_{S-P}}{m_{Wad}} \end{aligned} \quad (\text{A.2})$$

If we now compare the arrival times (t_P , t_S) at two different stations a and b for the same event, the source time will be the same.

$$t_0^a = t_0^b$$

As formula (2):

$$\begin{aligned} t_P^a - \frac{t_S^a - t_P^a}{m_{Wad}} &= t_P^b - \frac{t_S^b - t_P^b}{m_{Wad}} \\ t_P^a - t_P^b &= \frac{t_S^a - t_P^a}{m_{Wad}} - \frac{t_S^b - t_P^b}{m_{Wad}} \\ m_{Wad}(t_P^a - t_P^b) &= t_S^a - t_S^b + t_P^b - t_P^a \end{aligned}$$

As: $m = \frac{v_P}{v_S} - 1$,

$$\begin{aligned} \frac{v_P}{v_S}(t_P^a - t_P^b) - t_P^a + t_P^b &= t_S^a - t_S^b + t_P^b - t_P^a \\ \frac{v_P}{v_S}(t_P^a - t_P^b) &= t_S^a - t_S^b \\ \frac{v_P}{v_S} &= \frac{t_S^a - t_S^b}{t_P^a - t_P^b} \end{aligned} \quad (\text{A.3})$$

A.1.2 Derivation for time offset calculation from Wadati-Diagram

In order to identify the time offset of one station keep i fixed as one station. A useful indicator would be the n -value derived from the arrival times (see 2.1).

$$\begin{aligned} f(x) &= m_{diff}x & g(x) &= m_{diff}x + n \\ t_S^i - t_S^{ref} &= \frac{v_P}{v_S}(t_P^i - t_P^{ref}) & t_S^{i'} - t_S^{ref} &= \frac{v_P}{v_S}(t_P^{i'} - t_P^{ref}) + n \end{aligned} \quad (A.4)$$

While:

$$t_P^{i'} = t_P^i + t_{offset} \quad t_S^{i'} = t_S^i + t_{offset} \quad (A.5)$$

Thus,

$$\begin{aligned} g(x) &= m_{diff}x + n \\ t_S^i + t_{offset} - t_S^{ref} &= \frac{v_P}{v_S}(t_P^i + t_{offset} - t_P^{ref}) + n \\ t_S^i + t_{offset} - t_S^{ref} &= \frac{v_P}{v_S}t_P^i - \frac{v_P}{v_S}t_P^{ref} + \frac{v_P}{v_S}t_{offset} + n \\ t_{offset} - \frac{v_P}{v_S}t_{offset} &= \frac{v_P}{v_S}(t_P^i - t_P^{ref}) - t_S^i + t_S^{ref} + n \end{aligned}$$

See formula (4). So,

$$\begin{aligned} t_{offset}\left(1 - \frac{v_P}{v_S}\right) &= n \\ t_{offset} &= \frac{n}{1 - \frac{v_P}{v_S}} = \frac{n}{1 - m_{diff}} \end{aligned} \quad (A.6)$$



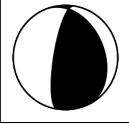

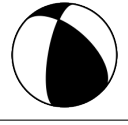
The coefficients m_{diff} and n can simply be estimated using linear regression of $t_S^i - t_S^{ref}$ over $t_P^i - t_P^{ref}$ (see formula A.4).

A.2 Shake reports during recording period of STRATEGY network

Date (UTC)	Location	z [km]	x_{epic} [km]	M_L	M_L
2016-07-13	-25.4834, -64.5867	23.3	12.0	3.2	None
2016-08-08	-25.4533, -64.5939	23.9	8.7	3.5	2.6
2016-09-01	-25.5, -64.5954	24.7	13.5	3.7	3.1
2016-09-06	-25.4787, -64.5606	27.0	12.9	3.3	3.0
2016-10-16	-23.9364, -64.1254	41.1 (10)	168.3 (244.4)	5.8	4.7

Table A.1: List of felt events during the installation period of the STRATEGY network. Shaking reports geolocated for El Galpón at -25.3833 lat, -64.6333 lon. Hypocenter information taken from the STRG catalog presented in this work. For comparison local magnitudes (M_L) are presented in the last column, while the second value is taken from the INPRES catalog. The "None" entry represents a missing event in the national catalog, although it was reported as felt.

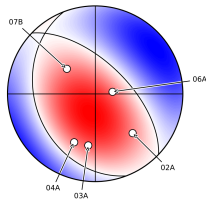
A.3 Moment Tensor solutions for 2015 El Galpón EQ

focal mechanism	Author	strike	dip	rake	depth [km]
	GCMT	190	63	126	22.8
	GEOFON	187	61	113	25
	IPGP	189	70	102	20
	NEIC	189.16	69.07	123.52	19.0
	NEIC	190	63	126	21.5

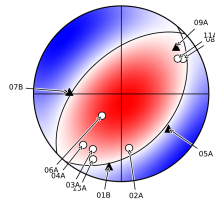
	NEIC	198	63	131	23.5
---	------	-----	----	-----	------

Table A.2: Comparison of focal mechanisms provided by various seismological observatories. Presented results solely modeled from teleseismic phases of global seismological networks. Data is taken from the ISC bulletin[1].

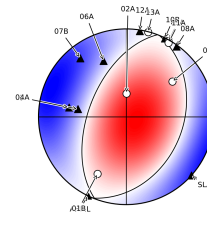
A.4 Focal Mechanisms of Supervised Events



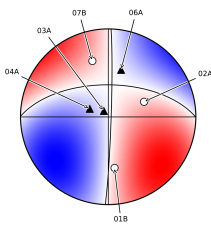
(a) Event 19



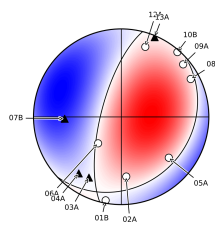
(b) Event 79



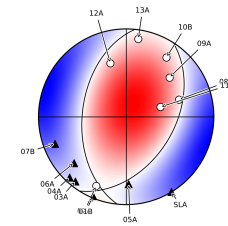
(c) Event 86



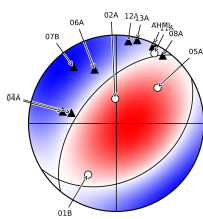
(d) Event 138



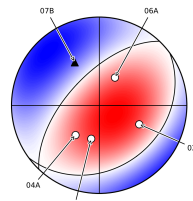
(e) Event 139



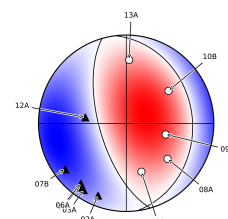
(f) Event 145



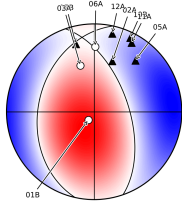
(g) Event 167



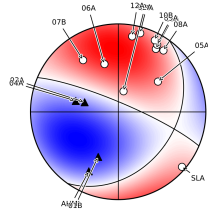
(h) Event 230



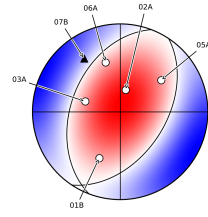
(i) Event 248



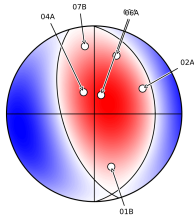
(j) Event 260



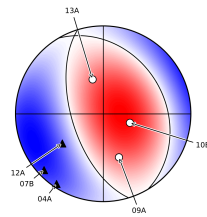
(k) Event 264



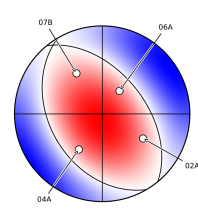
(l) Event 270



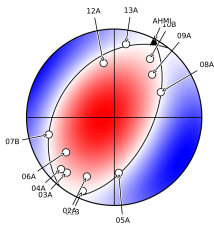
(m) Event 287



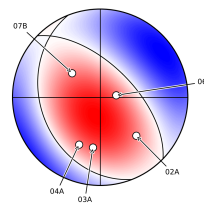
(n) Event 320



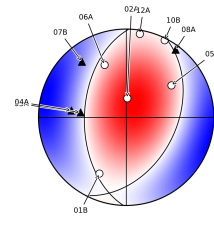
(o) Event 350



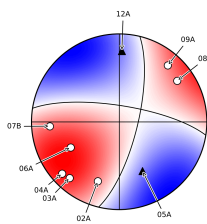
(p) Event 359



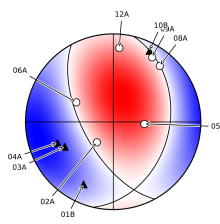
(q) Event 374



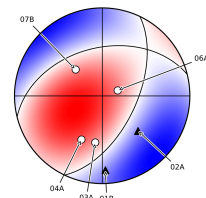
(r) Event 409



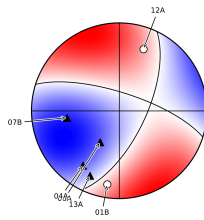
(s) Event 441



(t) Event 442



(u) Event 453



(v) Event 469

Figure A.1: Supervised focal mechanisms plotted in the map of Figure 8.1. The color-coding of the lower hemisphere shows the pressure nodal planes in blue and the tension nodal planes in red. The station samples on the focal sphere are plotted on top.

A.5 Velocity Models

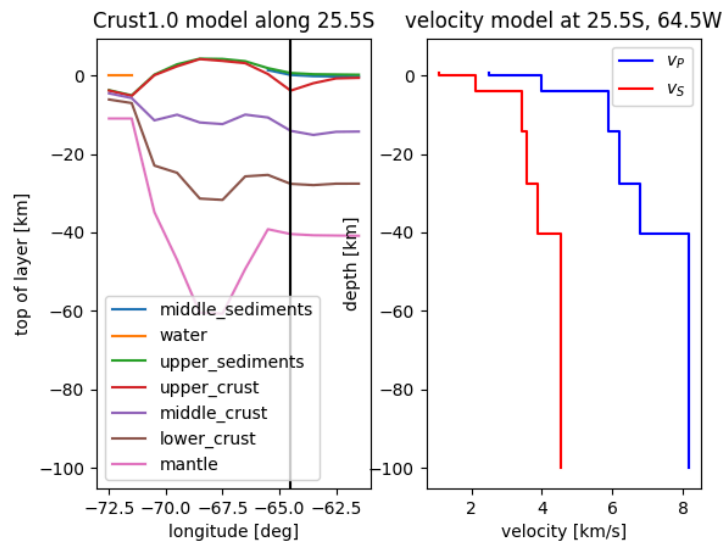


Figure A.2: The CRUST 1.0 velocity model [150]. *Left*: the layering of the velocity model is shown along a transect at -25.5° lat. The black line represents the location of the model shown on the right. *Right*: P- and S-wave velocity model at -64.5° lon, -25.5° lat.

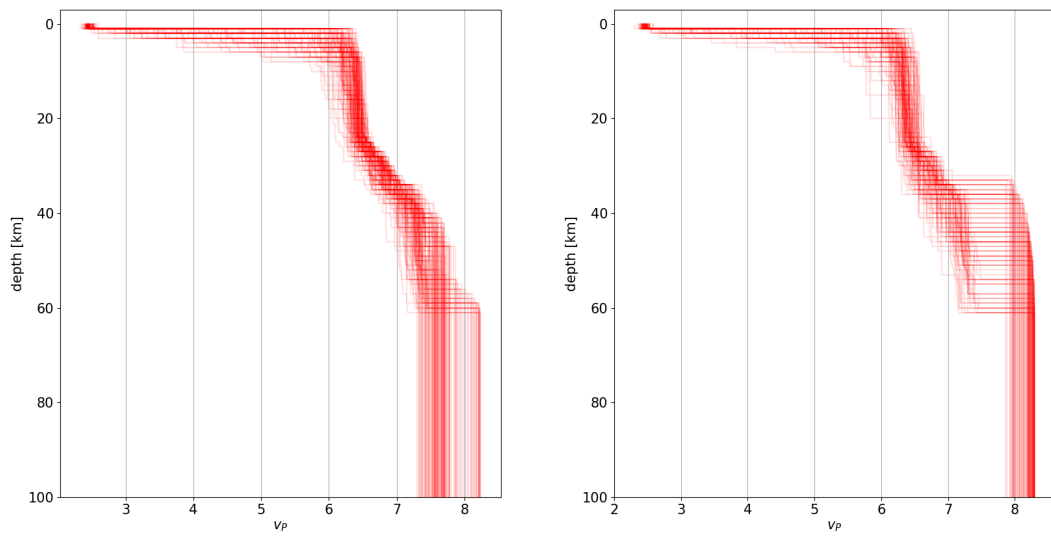


Figure A.3: Velocity models using continuously 1 km thickness with randomly varying total number of layers to incorporate different Moho depths. *Left:* All layers undamped and initial mantle velocity of 8.5 km/s. *Right:* The mantle layer is damped with a damping factor of 10 at 8.3 km/s.

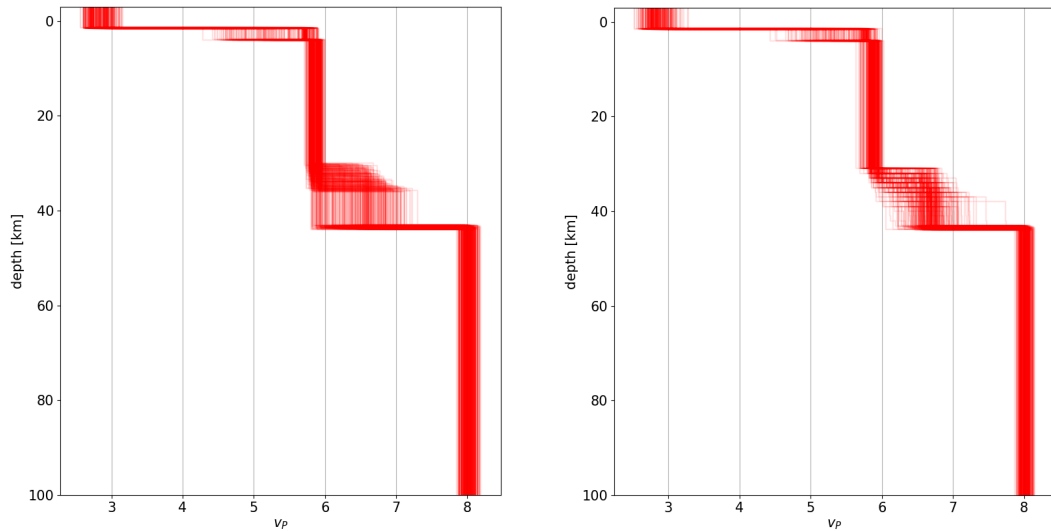


Figure A.4: Velocity models with reduced numbers of velocity layers and a small amount of depth variation for each layer, 500 runs each. Both model set-ups show equal RMS-errors (mean: 0.31 s). *Left:* A sharp boundary between the upper and lower crust at 33 km was varied ± 3 km to approach the best depth. *Right:* The gradual transition between upper and lower crust was implemented by introducing 1 km thick layers through the whole lower crust, starting at 31 km.

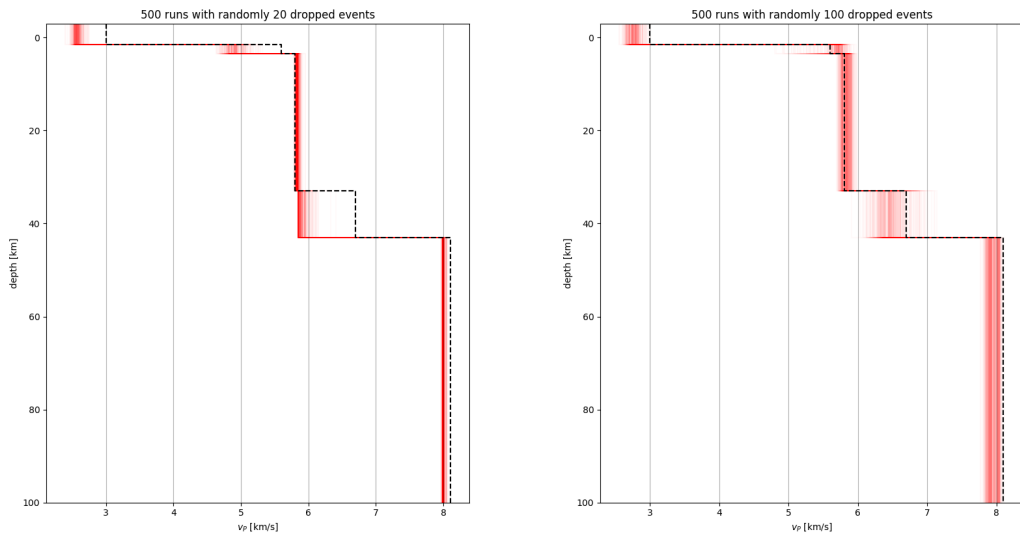


Figure A.5: Resulting 500 velocity models using a randomly reduced input catalog in red. The minimum 1D velocity model (from which random variations of the initial velocities are used) is shown in a black dashed line. *Left*: Jackknife resampling of 20 randomly chosen events and *right*: jackknife resampling of 100 randomly chosen and left out events.

jack knife - 200 models - random varying layer velocities

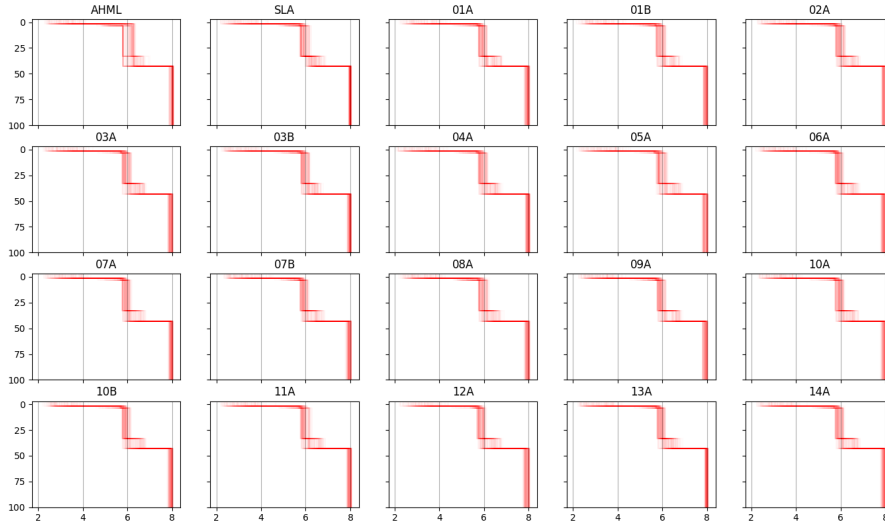


Figure A.6: Results of jackknife resampling of the used stations. Iteratively removing each station (one plot) and running 200 inversions with varying initial velocity values.

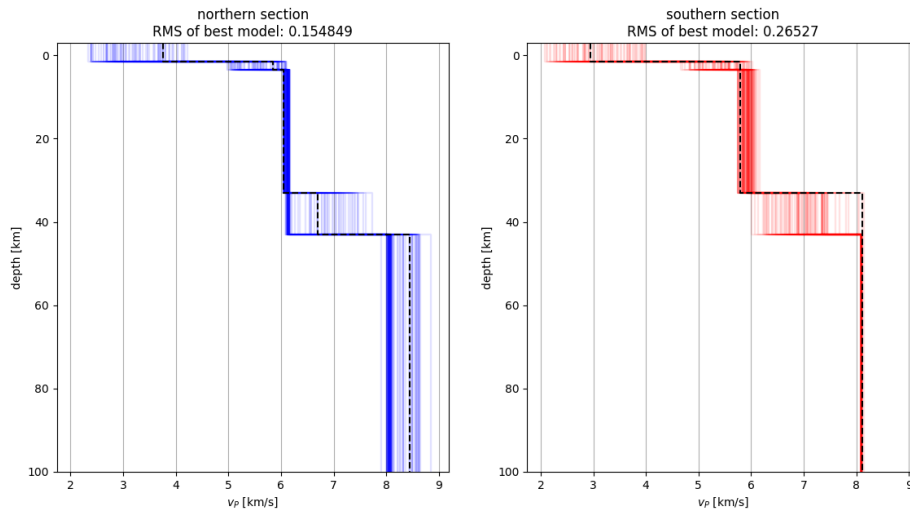
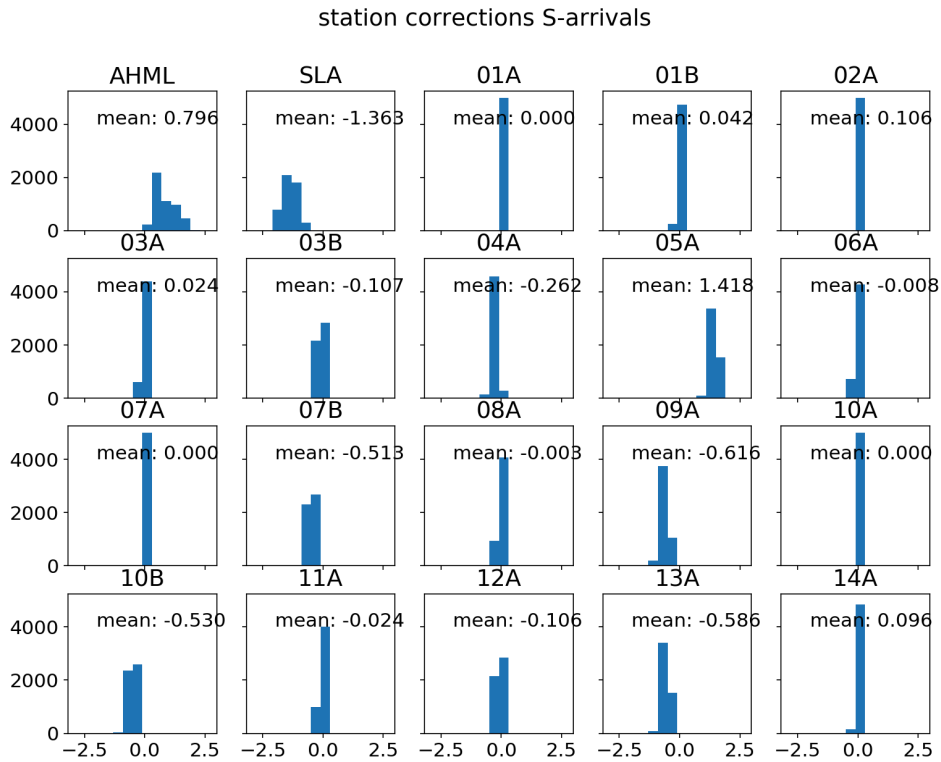
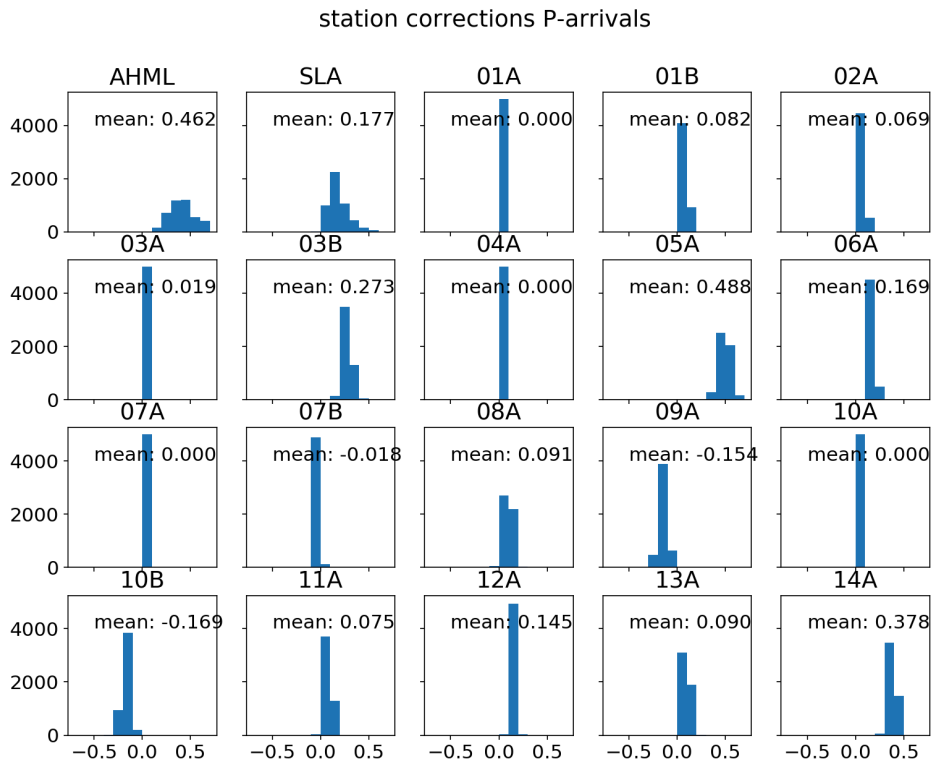


Figure A.7: Results of velocity modeling using a northern (blue) and a southern sub-network (red). Only models with RMS-errors below the 10th-quantile are shown. The dashed lines show the models with the lowest RMS-errors. In total, 1,000 runs were performed for each sector.



117

Figure A.8: Distribution of station correction values of all 5000 models, shown for each station. *Upper*: station corrections for P-wave arrivals, *lower*: station corrections for S-wave arrivals.

A.6 Uncertainty plots

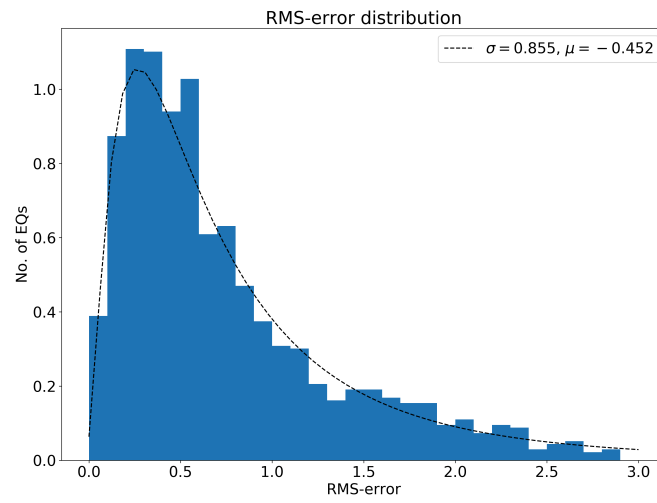


Figure A.9: The histogram (normed to one) of RMS-errors given by the location optimization with HYPOSAT. The parameters of a lognormal distribution (σ and μ) are fitted to the distribution of RMS-errors, using a maximum likelihood estimator.

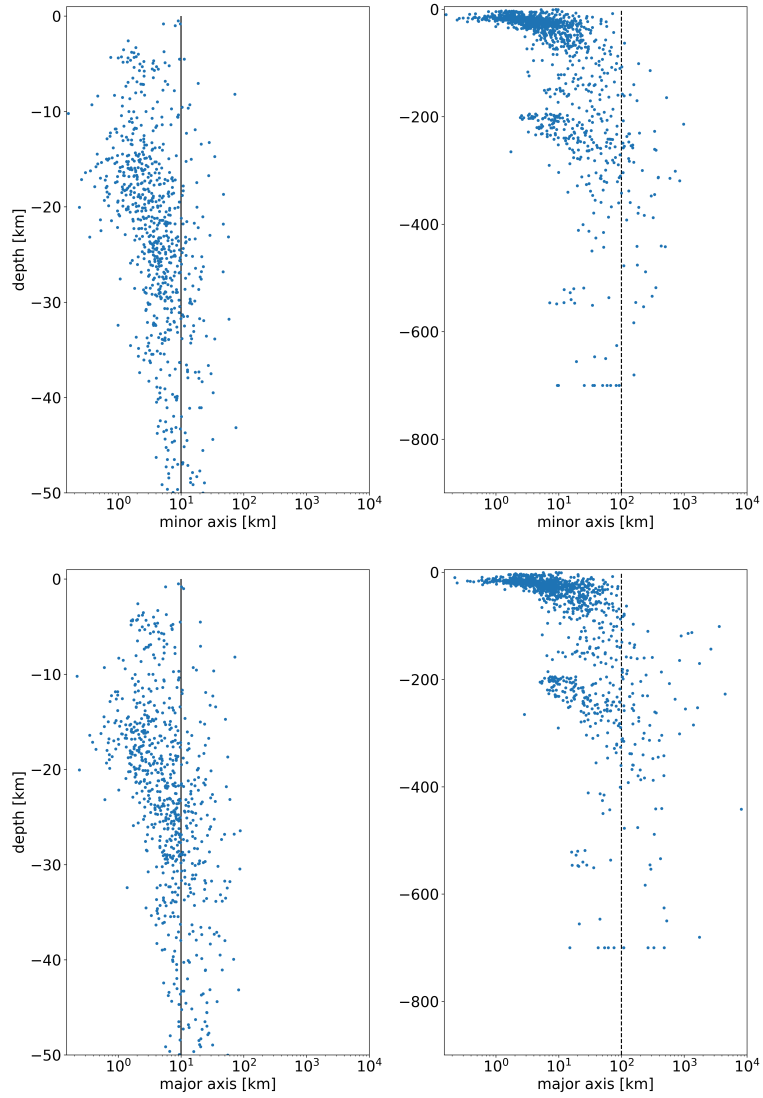


Figure A.10: Axes of the location error ellipses plotted over source depth, with different depth scales. *Upper*: minor axis represents the minimal horizontal location error, while *lower*: major axis expresses the maximal horizontal error.

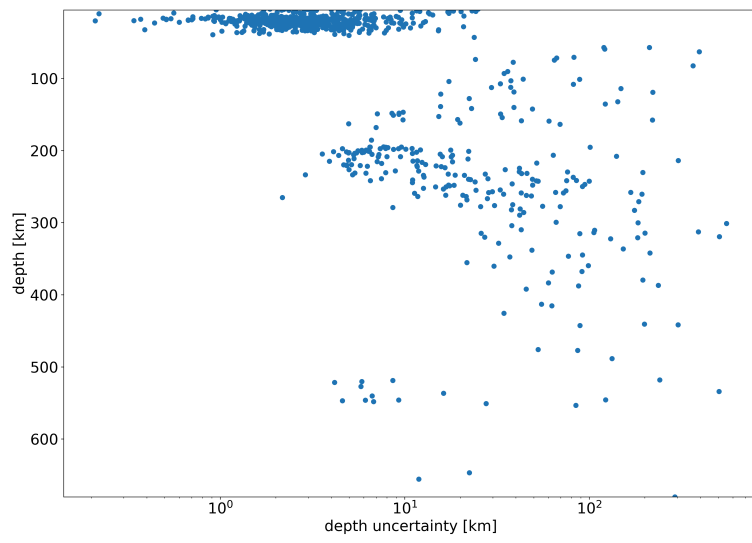


Figure A.11: Depth uncertainty over source depths.